Searches for Supersymmetry with compressed mass spectra using monojet events with the CMS detector at the LHC

Robyn Elizabeth Lucas
Imperial College London

A dissertation submitted to Imperial College London
for the degree of Doctor of Philosophy

Abstract

This is the abstract, find me in frontmatter.tex

Declaration

I, the author of this thesis, hereby declare the material presented here to be the result of my own work, except where explicit reference is made to the work of others. It has not been submitted for another qualification to this or any other university. All figures labelled "CMS" have been sourced from CMS publications, referenced in the caption, and include those produced by the author. Those figures labelled "CMS Preliminary" have been sourced from a CMS public preliminary document or an unpublished CMS document. All figures taken from external sources are referenced appropriately throughout this thesis.

Robyn Lucas

Acknowledgements

Contents

"For Peter"

—

Chapter 1

Introduction

"Everything starts somewhere, although many physicists disagree."
— Terry Pratchet

Chapter 2

Theory and Motivations

"Absence of evidence is not evidence of absence."
— Carl Sagan, 1934 – 1996

This chapter introduces the Standard Model (SM) as a gauge invariant Quantum Field Theory (QFT), and gives a description of the fundamental particles and their interactions. The shortcomings of the SM, outlined in Section 2.2, imply however that it must be an incomplete description of nature. A Supersymmetric extension of the SM can address many of these limitations and is described in Section 2.3. Particular emphasis is placed on the arguments for SUperSYmmetry (SUSY) with compressed mass spectra in Section 2.3.5, as this is the subject of this thesis.

2.1 The Standard Model of Particle Physics

The SM of particle physics provides a fantastically accurate description of the fundamental particles of nature and their interactions via the strong, electromagnetic, and weak forces at the electroweak energy scale. It has proved itself incredibly robust during the first years of Large Hadron Collider (LHC) running. Many high precision measurements of production cross sections (which can be understood as the number of events produced) are consistent with their loop level SM predictions, see Figure 2.1, which shows many different experimental measurements and theory expectations agree over 6 orders of magnitude. Even very rare processes have been measured to agree with their SM predictions: the decay $B_S \to \mu\,\mu$, very sensitive to new physics processes, has been observed at the level of three in every billion decays of the B_S meson [1]. Such tests of the SM cement its place as one of the major successes of 20$^{\text{th}}$ century physics.

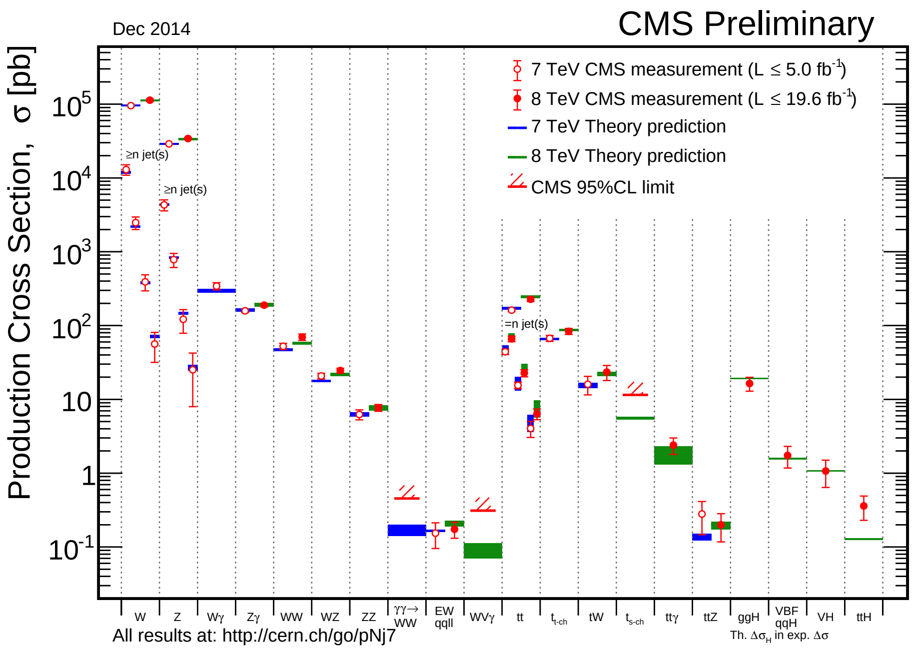

Figure 2.1: Combined results from CMS of many SM measurements made at LHC centre-of-mass energies of 7 and 8 TeV , taken from [2]. Theory and experiment agree over a vast range of production cross section values, for many different SM processes.

Developed in the 1960's and 1970's [3–6], the SM is a relativistic QFT in which particles are excitations of fields. It is gauge invariant, guaranteeing its renormalizability, and contains three symmetries: $SU(3)_C \otimes SU(2)_L \otimes U(1)_Y$. $SU(3)$ describes the strong force, felt by coloured particles, and $SU(2) \otimes U(1)$ describes the unified Electromagnetic and Weak forces, felt by particles with weak isospin and weak hypercharge. The Higgs mechanism [7] describes the spontaneous symmetry breaking of the $SU(2) \times U(1)$ gauge symmetry which allows for massive gauge bosons in a gauge invariant way. The discovery of the Higgs boson [8, 9] in July 2012, the mediator of the Higgs field, provided the last piece of the SM.

2.1.1 Fundamental particles and forces

All known matter in the universe can be described by the fundamental matter particles, which can be separated into quarks – those that feel the strong force, and leptons – those that do not. Matter particles are all spin-$\frac{1}{2}$ fermions that conform to Fermi statistics

Matter fermions: spin-$\frac{1}{2}$						
	Leptons			Quarks		
Generation	Particle	Mass (MeV)	Charge	Particle	Mass (MeV)	Charge
1	ν_e	~ 0	0	d	2.3	$-\frac{1}{3}$
	e	0.511	-1	u	4.8	$+\frac{2}{3}$
2	ν_μ	~ 0	0	s	95	$-\frac{1}{3}$
	μ	106	-1	c	1270	$+\frac{2}{3}$
3	ν_τ	~ 0	0	b	4180	$-\frac{1}{3}$
	τ	1780	-1	t	173200	$+\frac{2}{3}$

Table 2.1: Summary of the particles of the SM of particle physics. Fermions, of spin-$\frac{1}{2}$ are shown, split into the three generations of leptons and quarks. Masses are taken from Ref. [11].

and obey the Dirac equation [1].

$$(i\gamma^\mu \partial_\mu - m)\psi = 0, \tag{2.1}$$

where γ^μ are the Dirac matrices, which are defined by their anti-commutation relation $\{\gamma^\mu, \gamma^\nu\} = \gamma^\mu\gamma^\nu + \gamma^\nu\gamma^\mu = 2\eta^{\mu\nu} I_4$, where $\eta^{\mu\nu}$ is the Minkowski metric $(+, -, -, -)$, and I_4 is the four-dimensional identity matrix; δ_μ is the covariant derivative; and m is the mass of the particle. Repeated indices are summed over [10].

A summary of the matter particles of the SM can be found in Table 2.1. A similar table exists for the antiparticles of the leptons and quarks, a consequence of Equation 2.1, which has both positive and negative energy solutions. Rather than particles travelling backwards through time, as the negative energy solutions suggest, anti-particles are interpreted to have all of the same properties as their partner particles but with opposite charge.

Leptons are fundamental, free particles in nature. Conversely, quarks are fundamental but not free particles; they form hadrons: baryons, which consist of 3 quarks or anti-quarks, and mesons, a bound quark-anti-quark pair. This difference is due to the colour charge that quarks carry: they interact with the strong force, resulting in colour confinement and hadronization. Both quarks and gluons exist in three families or generations, with each subsequent family increasing in mass. Within the SM neutrinos are massless; however

[1]The convention $c = \bar{h} = 1$ is used throughout and the four vector indices are labelled μ and ν.

Force carrying gauge bosons: spin-1				
Force	Particle	Symbol	Mass (GeV)	Charge
Electromagnetic	Photon	γ	0	0
	W boson	W^+	80.4	1
Weak	W boson	W^-	80.4	-1
	Z boson	Z	91.2	0
Strong	Gluons (8)	g	0	0
Higgs Boson: spin-0				
-	Higgs	H^0	126	0

Table 2.2: Summary of the gauge bosons of the SM. The force carrying bosons of spin-1 are shown, with the Higgs boson to complete the picture. Masses are taken from Ref. [11].

neutrino oscillations observed in nature imply a non-zero mass [12]. However, due to the negligible mass as compared to the other SM particles as well as to the energy scales probed, here, and throughout, their mass is neglected.

Matter particles interact via the exchange of spin-1 gauge bosons. The photon (γ) mediates the electromagnetic interaction and the heavy $W^{\pm}$ and Z bosons mediate the weak interaction, through the mixing of the gauge fields when the respective forces are unified. There are 8 colourless gluons (g) that mediate the strong force. The properties of these bosons, and similarly the properties of the interactions, are a direct result of their gauge symmetry groups, detailed in Section 2.1.2. A summary of the bosons can be found in Table 2.2.

Discoveries of sub-atomic particles throughout the 19$^{\text{th}}$ and 20$^{\text{th}}$ Centuries drove the formulation of the SM. The electron was discovered by J.J. Thomson in the Cavendish Laboratory in 1897 [13], and the electron (anti)-neutrino was first proposed by Pauli in 1930 to explain the energy spectrum of beta decay [14], though it was not discovered until 1956 by Cowan and Reines at Los Alamos [15]. The muon was discovered in 1936 by Anderson and Neddermeyer at Caltech in studies of cosmic rays [16], and confirmed a year later in a cloud chamber experiment [17]. The muon neutrino was then discovered in 1962 by Lederman, Schwartz and Steinberger [18], after being proposed in the early 1940's. The u, d, and s quarks were first proposed in 1964 by Gell-Man and Zweig to explain the 'Eightfold' hadron structure [19, 20], and the three quarks were observed in deep inelastic scattering experiments at the Stanford Linear Accelerator Center (SLAC) four years later [21, 22]. The proposal of the GIM mechanism [23] in 1970 predicted the completion of the second generation – the charm quark in order to explain the observed suppression of Flavour Changing Neutral Currents (FCNC). The discovery of the J/Ψ meson in 1974 [24, 25] confirmed the existence of the charm quark. The third generation was more of a surprise. The τ lepton was proposed to explain an excess of events at the e^+e^- colliding ring at SLAC in the mid 1970's [26], and so postulating another generation of leptons. It was not until 2000 that the ν_τ was discovered [27], completing the lepton family. CP violation in kaon decay drove the proposal of the third quark generation in 1973 [28]. The bottom quark was first observed in 1977 at Fermilab with the observation of the bottomonium state, known as the Υ meson [29]. The top quark, after years of dedicated searches at SLAC, Deutsches Elektronen-Synchrotron (DESY) and European Organisation for Nuclear Research (CERN), was finally discovered in 1995 at the Tevatron [30, 31] and it remains the heaviest SM particle today.

The SM was thus built as a theory over several decades; driven by the need to explain experimental observations, and predicting the existence of particles that were then found later after dedicated searches. This is particularly evident in the discoveries of the W and Z bosons. The unification of electromagnetism and the weak nuclear force [3–5] around 1968 predicted the existence of both the charged W bosons and the neutral Z boson. They were discovered at CERN in 1983 using the UA1 and UA2 experiments on the Super Proton Synchrotron (SPS) collider ring [32–35]: experiments specifically designed to search for traces of the W and Z. Due to the non-perturbative nature of the strong force, interactions between quarks and gluons were (and remain) less certain, and theory is driven by experiment. The observation of three-jet events at PETRA [36, 37], DESY, provided direct evidence of gluons in 1979.

2.1.2 Gauge Symmetries

Neother's theorem [38] states that symmetries lead to conserved quantities in nature. If a physical process is unaffected by location or time, then its Lagrangian is symmetric under space and time translations. As a result, both energy and linear momentum are conserved quantities. If it is unaffected by spatial orientation, its Lagrangian is rotationally symmetric, leading to the conservation of angular momentum. The symmetries found in a Lagrangian which attempts to describe a system therefore reveal important and useful properties of that system. It is certainty reasonable that we should expect a theory to give the same answer 10 minutes ago as it does now; and in 10 minutes, or 10 years, or

10 millennia – any Lagrangian which is not invariant under time transformations should perhaps be revised. Indeed, the conserved quantity associated with invariance under time transformations, energy, is a cornerstone of physics. Energy is always conserved. Symmetries are therefore very powerful in forming conserved quantities, and vice versa. By demanding that any theory which describes the particle nature of our universe has the appropriate conserved quantities, we are demanding that its Lagrangian formalism is invariant under the various transformations.

The principle of Gauge Invariance drives the formalism of the SM. The SM Lagrangian is invariant under local gauge transformations: transformations which are space-time dependent. A gauge transformation takes the wavefunction describing a system to a different 'gauge', and in this gauge the Lagrangian is symmetric compared to the original state – there is a 'gauge symmetry'. Such gauge symmetries result in symmetry, or 'gauge' groups, and it is the generators of these gauge groups which lead to the gauge bosons. The generators manifest themselves as vector, or gauge fields – one for each degree of freedom in the symmetry group. Mathematically, the substitution of

$$\partial_\mu \rightarrow D_\mu = \partial_\mu - igA_\mu \tag{2.2}$$

for the covariant derivative in the Dirac equation, where g are the coupling constants of the gauge group indicating interaction strength and A_μ are the gauge fields which transform as

$$A_\mu \rightarrow A_\mu + \frac{1}{g}\partial_\mu \theta \tag{2.3}$$

ensures gauge invariance under the transformation

$$\psi \rightarrow \psi' = e^{i\theta}\psi \tag{2.4}$$

by construction, where θ is any gauge tranformation.

The formulation of Quantum Electro-Dynamics (QED) gives the simplest demonstration of the use of gauge symmetries. Under a local U(1) abelian gauge transformation, the wavefunction transforms as

$$\psi(x) \rightarrow \psi'(x) = e^{i\theta(x)}\psi(x) \tag{2.5}$$

where $\theta(x)$ implies a local rotation of the phase angle of the electron field. Taking the free Lagrangian, which follows from Eq. 2.1,

$$\mathcal{L} = \bar{\psi}(x)(i\gamma^{\mu}\partial_{\mu} - m)\psi(x) \tag{2.6}$$

and substituting in for the gauge covariant derivative,

$$\mathcal{L} = \bar{\psi}(x)(i\gamma^{\mu}D_{\mu} - m)\psi(x), \tag{2.7}$$

we can demonstrate the gauge invariance. Transforming the wavefunction according to Eq. 2.5, where ψ and θ are functions of x, and substituting in Eq. 2.3 for the gauge transformation of A_{μ},

$$\begin{aligned}
\mathcal{L}' &= e^{-i\theta}\bar{\psi}(i\gamma^{\mu}(\partial_{\mu} - ig(A_{\mu} + \frac{1}{g}\partial_{\mu}(\theta)) - m)e^{i\theta}\psi && (2.8)\\
\mathcal{L}' &= \bar{\psi}(i\gamma^{\mu}(\partial_{\mu} - igA_{\mu}) - me^{i\theta})\psi + e^{-i\theta}\bar{\psi}i\gamma^{\mu}(ie^{i\theta}\psi\partial_{\mu}(\theta) - i\partial_{\mu}(\theta)e^{i\theta}\psi) && (2.9)\\
\mathcal{L}' &= \mathcal{L} && (2.10)
\end{aligned}$$

as the last term equates zero. QED is therefore gauge invariant under a local gauge transformation, which guarantees its renormalizability as a theory. A_{μ} is interpreted as the massless photon field which has coupling $g = e$. In order to regard A_{μ} as a physical field a kinetic term must be added to the Lagrangian of Eq. 2.7. To maintain gauge invariance, the kinetic term is of the form $F_{\mu\nu} = \partial_{\mu}A_{\nu} - \partial_{\nu}A_{\mu}$. The full QED Lagrangian can thus be written as

$$\begin{aligned}
\mathcal{L}_{QED} &= \mathcal{L}_{int} + \mathcal{L}_{kin} && (2.11)\\
&= \bar{\psi}i\gamma^{\mu}D_{\mu}\psi - \frac{1}{4}F_{\mu\nu}F^{\nu\mu} - m\bar{\psi}\psi && (2.12)
\end{aligned}$$

The lack of any photon mass term, of the form $m^2A_{\mu}A^{\mu}$ (which would not be gauge invariant), implies the photon is massless. Thus, by requiring gauge invariance and using the simple free particle Dirac Equation, which is invariant under $U(1)_{EM}$ symmetry, we arrive at the QED Lagrangian that gives a massless photon field, A_{μ}, with interaction strength e.

2.1.3 Electroweak Unification

The requirement of local gauge invariance in the weak sector, in conjunction with QED, can be used to unify the electromagnetic and weak forces. The Electroweak (EWK) sector is defined by the symmetry groups $SU(2)_L \otimes U(1)_Y$.

The special unitary group $SU(2)_L$, of order 2, is generated by the 2×2 matrices $T_i = \tau_i/2$, where τ_i are the three Pauli spin matrices [2]. The three generators are manifested in the three gauge fields W^1_μ, W^2_μ, and W^3_μ. They act only on the left handed chiral component of the field ψ_L, where $\psi = \psi_L + \psi_R$ and $\psi_{L/R} = (1 \mp \gamma_5)\psi$; where $\gamma^5 = i\gamma^0\gamma^1\gamma^2\gamma^3$. This reflects the experimental observation of parity violation in weak interactions: W^i_μ couple only to the left handed component of the fermion wavefunctions, hence the L subscript. The weak isospin t_i are the corresponding conserved quantities. The unitary group $U(1)_Y$ brings an additional generator, hypercharge Y, which is manifested in the gauge field B_μ. Here, the conserved quantity is hypercharge y, where electric charge $Q = t_3 + y/2$. Incidently, $U(1)_Y$ is a different representation of the $U(1)_{EM}$ gauge group used in Section 2.1.2, which instead has generator Q, and gauge field A_μ, where electric charge is the conserved quantity.

Due to the parity violating nature of the electroweak representation, the left and right handed components of the fermion wavefunction are written separately as χ_L, a doublet, and ψ_R, a singlet. Their $SU(2)_L \otimes U(1)_Y$ gauge transformations can then be written as:

$$\chi_L \to \chi'_L = e^{i\theta(x)\cdot T + i\theta(x)Y}\chi_L \tag{2.13}$$

$$\psi_R \to \psi'_R = e^{i\theta(x)Y}\psi_R. \tag{2.14}$$

Gauge invariance is maintained by modifying the covariant derivative accordingly:

$$\partial_\mu \to D_\mu = \partial_\mu - ig_1\frac{Y}{2}B_\mu - ig_2\frac{\tau_i}{2}W^i_\mu. \tag{2.15}$$

[2] The $SU(2)$ generators are labelled i, j, and k

To recover the familiar physical bosons of Table 2.2, the $SU(2)_L$ and $U(1)_Y$ symmetries are combined via a rotation of the separate gauge bosons:

$$W^{\pm}_{\mu} = \frac{1}{\sqrt{2}}(W^1_{\mu} \mp W^2_{\mu}) \tag{2.16}$$

$$Z_{\mu} = \cos\theta_W W^3_{\mu} - \sin\theta_W B_{\mu} \tag{2.17}$$

$$A_{\mu} = \sin\theta_W W^3_{\mu} + \cos\theta_W B_{\mu}, \tag{2.18}$$

where A_{μ} is the photon field and the Weinberg angle, θ_W, is determined by the ratio of the electromagnetic coupling constant (g_1) and the weak coupling constant (g_2):

$$\frac{g_1}{g_2} = \frac{\sin\theta_W}{\cos\theta_W}. \tag{2.19}$$

The fermion wavefunctions are then written in terms of left-handed states (the electroweak doublet), and right-handed state (the electroweak singlet). For the leptons, these are:

$$\chi_L = \begin{pmatrix} \nu_e \\ e \end{pmatrix}_L, \begin{pmatrix} \nu_\mu \\ \mu \end{pmatrix}_L, \begin{pmatrix} \nu_\tau \\ \tau \end{pmatrix}_L = L \tag{2.20}$$

$$\psi_R = e_R, \mu_R, \tau_R = e_R, \tag{2.21}$$

where there is no right-handed neutrino, using the notation where L and e_R are implicitly summed over the three generations of left-handed lepton doublets and right-handed electron-like right-handed singlets. For the quarks,

$$\chi_L = \begin{pmatrix} u \\ d \end{pmatrix}_L, \begin{pmatrix} c \\ s \end{pmatrix}_L, \begin{pmatrix} t \\ b \end{pmatrix}_L = Q_L \tag{2.22}$$

$$\psi_R = u_R, d_R, c_R, s_R, t_R, b_R = u_R, d_R \tag{2.23}$$

where, similarly, Q_L is summed over the three generations, and u_R and d_R are summed over the three generations of up-type and down-type quarks. This gives five types of fermion wavefunction. We can then write ψ, the total fermion wavefunction, as ψ^i, for $i \in 1-5 = e_R, L, u_R, d_R, Q_L$, and the sum over three generations is implicit.

Compressing the fermion wavefunction as such allows a concise definition of the fermion interaction Lagrangian:

$$\mathcal{L}_{int} = \bar{\psi} i\gamma^{\mu} D_{\mu} \psi \tag{2.24}$$

where D_μ is defined in Eq. 2.15. In the same way as for QED, to describe a physical system and allow the propogation of the gauge fields, a kinetic term of the form $\frac{1}{4}F_{\mu\nu}F^{\mu\nu}$ is required. The term for the B_μ gauge field follows from Eq. 2.12, and a similar expression for W_μ^i is necessary, which is given by the field strength tensor for the $SU(2)$ group:

$$B_{\mu\nu} = \partial_\mu B_\nu - \partial_\nu B_\mu \tag{2.25}$$

$$W_{\mu\nu} = \partial_\mu W_\nu^i - \partial_\nu W_\mu^i - g_2 \epsilon^{ijk} W_\mu^j W_\nu^k \tag{2.26}$$

The kinetic term of the Lagrangian can thus be defined,

$$\mathcal{L}_{kin} = -\frac{1}{4}F_{\mu\nu}F^{\mu\nu} = -\frac{1}{4}\left(B_{\mu\nu}B^{\mu\nu} + W_{\mu\nu}W^{\mu\nu}\right), \tag{2.27}$$

and the full $SU(2)_L \times U(1)_Y$ Lagrangian is simply written as

$$\mathcal{L}_{EWK} = \mathcal{L}_{int} + \mathcal{L}_{kin}. \tag{2.28}$$

Notice that here, as for QED, there are no boson mass terms of the form $m^2 X_\mu X^\mu$. While this is sensible for the photon field, as the photon is known to be massless, the W and Z bosons are heavy. Similarly, mass terms such as $m\bar{\psi}\psi$ for the fermions are absent: this, too, is at odds with nature. Adding such mass terms to the Lagrangian would break the gauge symmetry. Masses are instead generated using the Higgs mechanism. By introducing an extra scalar field (with an associated massive scalar boson), spontaneous symmetry breaking is induced in order to give mass to the electroweak bosons, and SM fermions, in a gauge invariant way.

2.1.4 Electroweak Symmetry Breaking and the Higgs Mechanism

The previous discussion tells us that if we are to believe $\mathcal{L}_{EWK}$ to be an accurate description of the electroweak force, both the bosons and fermions must be massless: something which observation tells us is clearly not true. Mass terms cannot be introduced to the Lagrangian as they break gauge invariance; the masses of what we know to be the heavy vector bosons $W^{\pm}$ and Z^0 (as well as the fermions) are instead generated by the Higgs mechanism. The $SU(2)$ symmetry is broken spontaneously, while preserving the invariance of the Lagrangian itself and the renormalizability of the theory.

To start with, we introduce a scalar $SU(2)$ field ϕ:

$$\Phi = \begin{pmatrix} \phi_1 \\ \phi_2 \end{pmatrix}, \tag{2.29}$$

where ϕ_i are complex fields: $\phi_i = \mathrm{Re}(\phi_i) + i\mathrm{Im}(\phi_i)$; in total then, there are four real scalar fields. The additional term in the Lagrangian takes the form

$$\mathcal{L}_H = (D_\mu \Phi)^\dagger (D^\mu \Phi) - V(\Phi), \tag{2.30}$$

and in order to break the $SU(2)$ symmetry spontaneously, the potential term $V(\Phi)$ must take a very specific form:

$$V(\Phi) = -\mu^2 \Phi^\dagger \Phi + \lambda (\Phi^\dagger \Phi)^2 \tag{2.31}$$

where $\mu^2 < 0$ and $\lambda > 0$. Compared to the Lagrangian for a complex scalar, the μ term has the wrong sign: it is *not* the mass. Instead, the potential has a 'Mexican hat' shape, see Figure 2.2, and gives a non-zero expectation value as it forms a circle in phase space. Any point on this circle gives the same solution, and the vacuum state, at which point the potential gives the Vacuum Expectation Value (VeV), can be in any direction. This choice of direction, to determine where the field acquires a non-zero VeV, causes the symmetry to become spontaneously broken. The field no longer looks the same in all directions of the $SU(2)$ phase space; $SU(2)$ is no longer invariant.

The convention is to chose the VeV as

$$\langle 0|\Phi|0\rangle = \begin{pmatrix} 0 \\ v/\sqrt{2} \end{pmatrix} \text{ where } v = \sqrt{\frac{-\mu^2}{\lambda}} \tag{2.32}$$

as the minimum of the Higgs potential, given by $\Phi^\dagger \Phi = \frac{1}{2}(-\mu)^2/\lambda$, is chosen to be consistent with the ground state of the vacuum. Fluctuations from this zero point are

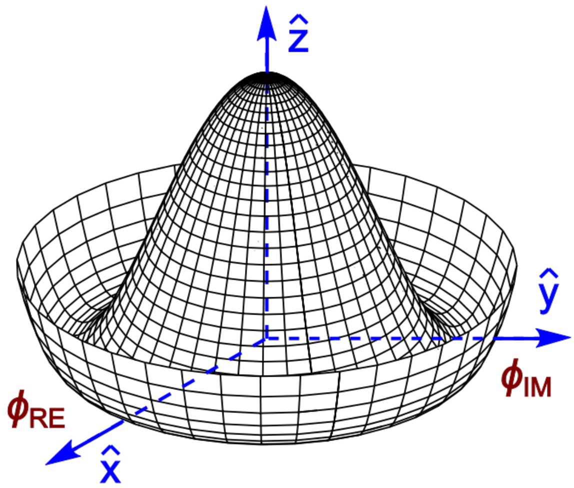

Figure 2.2: Higgs 'Mexican Hat' potential

then parametrized in terms of the four real scalar fields $\theta_1, \theta_2, \theta_3$, and $h(x)$.

$$\Phi(x) = \begin{pmatrix} \theta_2 + i\theta_1 \\ v/\sqrt{2} + h(x)/\sqrt{2} - i\theta_3 \end{pmatrix} = e^{i\tau \cdot \theta(x)/v} \begin{pmatrix} 0 \\ v/\sqrt{2} + h(x)/\sqrt{2} \end{pmatrix} \tag{2.33}$$

The four scalar fields can be interpreted as four massless Goldstone bosons. The exponential factor is recognised as a $SU(2)$ gauge transformation, so by moving to a different gauge in which this term becomes unity (the unitary gauge), we can arrive at

$$\Phi(x)' = \frac{1}{\sqrt{2}} \begin{pmatrix} 0 \\ v + h(x) \end{pmatrix}. \tag{2.34}$$

Substituting this expression for $\Phi'(x) = \Phi(x)$ into the covariant derivative term of $\mathcal{L}_H$, using Eq. 2.15, the mass terms for the three gauge bosons we require to complete the electroweak unification present themselves:

$$(D_\mu \Phi)^\dagger (D^\mu \Phi) = \frac{1}{2}(\partial_\mu h)^2 + \frac{g_2^2 v^2}{8}\left(W_\mu^+ W^{+\mu} + W_\mu^- W^- \mu\right) + \frac{(g_1^2 + g_2^2)v^2}{8} Z_\mu Z^\mu + 0 A_\mu A^\mu . \tag{2.35}$$

Here, we have substituted in the physical gauge bosons $W_\mu^\pm, Z_\mu$ and A_μ for the fields W_μ^i and B_μ. This mechanism for spontaneous symmetry breaking gives the expected mass terms of the form $\frac{1}{2}m^2 X_\mu X^\mu$ for the $W^\pm$ and Z in terms of their couplings:

$$m_W = \frac{g_2 v}{2} \tag{2.36}$$

$$m_Z = \frac{\sqrt{g_1^2 + g_2^2}\, v}{2} = \frac{m_W}{\cos\theta_W}. \tag{2.37}$$

Crucially, the photon remains massless. By moving to the unitary gauge, we have lost three of the Goldstone bosons, or equivalently three degrees of freedom. The fourth massless Goldstone boson has become a massive scalar boson, the SM Higgs boson, with mass $m_H = \sqrt{-2\mu^2}$. The three lost degrees of freedom correspond to the longitudinal polarizations of the new massive boson.

Adding the Higgs potential to the SM Lagrangian has allowed massive gauge bosons in a gauge invariant way. The remaining missing fermion mass terms can now be filled in using a similar method. By adding a Yukawa coupling (that is invariant under $SU(2)$) between the Higgs field and the fermions in the Lagrangian, the same Higgs boson can generate their masses. The additional terms in the Lagrangian are of the form

$$\mathcal{L}_{Yukawa} = k_e \bar{L}\Phi e_R + h.c. + \left(k_u \bar{Q_L}\Phi d_R + k_d \bar{Q_L}\tilde{\Phi} u_R\right) + h.c \tag{2.38}$$

where $\tilde{\Phi} = i\tau_2 \Phi^*$ for up-type quark wavefunctions is necessary for gauge invariance. In the same unitary gauge of Eq. 2.34, we find the couplings of the fermions to the Higgs field are then equal to their masses; $m_e = k_e v/\sqrt{2}$ and similarly for m_u, m_d where k_u and k_d are arbitrary, non-diagonal 3×3 matrices. These are the Cabibbo-Kobayashi-Maskawa (CKM) matrices and dictate the flavour structure of the SM [28, 39].

The remaining piece of the SM not mentioned above is the description of the strong interaction. It only affects coloured particles, and as a result of its $SU(3)$ gauge invariance, the generators are the Gell-Mann matrices λ_a where $a = 1, 2, ...8$ which give rise to eight gluons G_a. To incorporate the strong force, which gives rise to Quantum Chromo-Dynamics (QCD), we simply add the $SU(3)$ terms to the covariant derivative and $\mathcal{L}_{kin}$:

$$D_\mu = \partial_\mu - ig_1 \frac{Y}{2} B_\mu - ig_2 \frac{\tau_i}{2} W_\mu^i - ig_3 \frac{\lambda_a}{2} G_\mu^a \tag{2.39}$$

$$\frac{1}{4} F_{\mu\nu} F^{\mu\nu} = \frac{1}{4}\left(B_{\mu\nu}B^{\mu\nu} + W_{\mu\nu}W^{\mu\nu} + G^a_{\mu\nu}G_a^{\mu\nu}\right). \tag{2.40}$$

Gauge invariance dictates the form of the electroweak Lagrangian. Spontaneous symmetry breaking via the Higgs mechanism leads to three to massive gauge bosons, one massless gauge boson, and one massive scalar boson. The SM Lagrangian can then be written by summing the various terms discussed above:

$$\mathcal{L} = \mathcal{L}_{int} + \mathcal{L}_{kin} + \mathcal{L}_{H} + \mathcal{L}_{Yukawa} \tag{2.41}$$

$$= \bar{\psi}\, i\gamma^{\mu} D_{\mu}\psi - \frac{1}{4}F_{\mu\nu}F^{\mu\nu} + |D_{\mu}\Phi|^2 + \mu^2|\Phi|^2 - \lambda\,|\Phi|^4 + \left(\bar{\psi}_i k_{ij}\psi_j + h.c\right) \tag{2.42}$$

2.2 Motivation for Physics Beyond the Standard Model

Despite its many successes, fundamental theoretical flaws in the SM, as well as observed phenomena it fails to explain, imply there must be new physics at some energy scale. Various experimental observations – gravity, the matter-antimatter imbalance in the universe, neutrino oscillations, dark matter – all have no explanation in the SM. Questions of the naturalness of the theory with regard to fine tuning the mass of the Higgs boson, the non-unification of the fundamental forces, and the seemingly arbitrary number of parameters lead many theorists to believe the SM to be a low energy approximation of some new form of physics – physics which solves the underlying theoretical problems, as well as filling in the 'holes'.

Gravity has no place within the SM; there is no interaction to explain the gravitational attraction felt by the fundamental particles which is so evident at large distance scales. Despite its negligible influence on subatomic particles at the energy scales probed by the LHC, the gravitational force cannot be reconciled with a quantum theory.

In addition, there is insufficient Charge Parity (CP) violation within the SM to explain the observed matter dominance in the Universe. The CP violation in the kaon and D_0 meson sectors is not enough to explain why only matter remains from the Big Bang, in which matter and antimatter are thought to have been produced in even quantities. Physics Beyond the Standard Model (BSM) is necessary to introduce another source of it in order to explain we why are here at all; why all matter did not annihilate soon after it was created.

The solar neutrino problem, in which there were far less ν_e arriving at the Earth from the Sun than solar models predicted, was solved with the discovery of neutrino oscillations [40]. The ν_e, on their flight from the sun, were changing state so that when they were measured on Earth they were no longer in the electron-like weak eigenstate. They had oscillated into a different weak eigenstate, and so appeared to have disappeared when measured in electron-like charged current interactions. Neutrino oscillations imply that there is a mass difference between the different mass eigenstates of the neutrinos, ν_1, ν_2, ν_3, which are a superposition of their weak flavour eigenstates ν_e, ν_μ, ν_τ. A mass difference means each type of neutrino must have a mass (albeit small) – in contradiction of the massless, left handed neutrinos present in the SM. New physics is needed to explain massive neutrinos.

The flaw in the SM getting perhaps the most attention at the moment, in the current post-Higgs boson discovery era, is that it has no candidate for Dark Matter (DM). Astronomical observations of galaxy rotation curves [41], gravitational lensing [42, 43], the Cosmic Microwave Background [44], the Bullet Cluster [45], and large scale structures [46] imply that there is a 'dark' matter present in the universe; dark because it does not interact with electromagnetic radiation. Its presence is only inferred by its gravity. Therefore it must be also stable and weakly interacting – we have found no unequivocal evidence of DM decay products (although recent gamma-line spectra from the centre of the galaxy could suggest DM annihilation [47]). Astronomical observations imply that DM makes up around 26.8% of the energy budget of the universe, compared to the 4.9% of the matter the SM is comprised of. For our model of the fundamental forces and particles of the universe, the SM, to have no DM candidate leads us to question it – and come to the conclusion there must be something more. It is perhaps worth mentioning that Dark Energy, which is theorized to constitute the remaining 68.3% of the energy budget, and is responsible for the observed expansion of the universe, is not understood at all!

While the above are pieces of experimental evidence that cannot be explained by the SM, there are also theoretical problems with the model when calculating the radiative corrections to the Higgs boson mass. We saw in Eq. 2.31 that the scalar potential giving rise to the Higgs Boson h is of the form

$$V \sim m_{H0}^2 h^2 + \lambda h^4. \tag{2.43}$$

The presence of the quartic term, proportional to λ, implies the Higgs interacts with itself at loop level. This self-interaction adds another, quadratically divergent term to the mass of the Higgs, m_H:

$$m_H^2 \sim m_{H0}^2 + \frac{\lambda}{4\pi^2}\Lambda^2 + \delta M_H^2, \tag{2.44}$$

where Λ is some cut-off energy scale to where the physics is valid. If there is no new physics between the electroweak scale at ~ 100 GeV and the Planck scale, then Λ is of the same order as the Planck scale. Indirect constraints on the Higgs mass from measurements of the W and top quark masses [48, 49] imply that the Higgs mass is around the electroweak scale, and indeed direct measurements of the Higgs boson mass are around 125 GeV [50, 51] – not M_{Pl}. The term δM_H^2 then must cancel out the term in Λ; ie there must be a cancellation of order $M_{Pl} \sim 10^{18}$. To put this hierarchy problem another way, there is a precise fine-tuning necessary, of one part in 10^{18}. Although possible, this is very unnatural, and drives the much of the theoretical motivation for BSM physics.

SUSY [52, 53] is one example of an extension to the SM which can solve many of its problems, and is the subject of remainder of this chapter, as well as the analysis work done in this thesis. It is probably the most popular and well studied BSM theory in the community, however is not alone: models of Large Extra Dimensions [54], the SeeSaw Mechanism [55, 56], and Little Higgs [57] are just a few examples of many theories which attempt to explain the shortcomings of the SM by introducing new physics.

2.3 Supersymmetry

SUSY first emerged in the 1970's as a result of the mathematical considerations of QFT. The Coleman-Mandula theorem [58], which states that space time and internal symmetries cannot be combined anything but trivially, was found to have a hole in it [59]. This allows a symmetry between fermions (f) and bosons (b):

$$\hat{O}|f\rangle = |b\rangle; \qquad \hat{O}|b\rangle = |f\rangle \tag{2.45}$$

where $\hat{O}$ is the supersymmetric operator generating the transition. SUSY relates particles of different spin, where they differ by a half integer unit, and the Lagrangian remains invariant under transformations such as those in Eq. 2.45. The generated particles, or sparticles, have the all of the same quantum numbers as those particles they have been generated with (but for the spin) – so they have the same mass.

If we reconsider the one loop corrections to the Higgs field, h, with massive fermions ψ and massive scalars ϕ [60] (which can be generated by a supersymmetric transition as they differ in spin by a half-integer unit), we see additional terms in m_H^2:

$$\begin{aligned} m_H^2 \sim m_{H0}^2 + \frac{\lambda_F^2}{4\pi^2}(\Lambda^2 + m_F^2) - \frac{\lambda_S^2}{4\pi^2}(\Lambda^2 + m_S^2) \\ + \text{ logarithmic divergences } + \text{ uninteresting terms }. \end{aligned} \tag{2.46}$$

Crucially, there is a relative minus sign between the two quadratic terms in Λ, a result of Fermi statistics. If the couplings between the Higgs and the fermion λ_F and scalar λ_S are equal, then the quadratic terms in Λ cancel, and all that remains of the troubling quadratic divergence of Eq. 2.44 are the mass terms:

$$m_H^2 \sim m_{H0}^2 + \frac{\lambda_F^2}{4\pi^2}(m_F^2 - m_S^2). \tag{2.47}$$

Here, the fermion and scalar have been generated by a supersymmetric transition, and thus have the same quantum numbers. They have the same mass – and so the quadratic term completely cancels out. The fine tuning problem has been solved. However, no scalar particle has been observed with the same quantum numbers, and mass, of any fermion. No scalar particle with the same quantum numbers and different mass have been observed either, up to the energies probed – which, at the LHC, is of order 1 TeV.

It was the theoretical breakthrough in the 1980's that allowed SUSY to be a broken symmetry: the mathematical framework remains consistent even if the masses are not the same. Then, the second term in Eq. 2.47 remains – but, provided the masses are 'not too different' (where the allowed differences are seemingly a matter of opinion, deemed 'naturalness', but general consensus is of order a few TeV so reachable at LHC energies) - the issue of the fine-tuning of the Higgs mass is resolved, as the huge corrections necessary with no SUSY are now far more manageable.

SUSY, then, is a BSM theory with a foundation in the mathematics of QFTs, which, as a consequence of its symmetry, cancels out the huge quadratic divergences in the Higgs mass, making it very appealing. The SM becomes a part of a wider supersymmetric model that maintains the same $SU(3) \times SU(2) \times U(1)$ gauge symmetry. In the Minimal Supersymmetric Standard Model (MSSM), every SM particle gets a supersymmetric particle (sparticle) partner which has the same quantum numbers but differs a half integer unit in spin and has a greater mass. A rich sparticle phenomenology results, as the entire spectrum of SM particles is doubled. For example, the left-handed quark doublet gets a doublet of left handed scalars:

$$Q_L = \begin{pmatrix} u \\ d \end{pmatrix}_L \quad ; \quad \tilde{Q}_L = \begin{pmatrix} \tilde{u}_L \\ \tilde{d}_L \end{pmatrix} \tag{2.48}$$

and similarly, L, e_R, u_d, d_R defined in Section 2.1.3 get $\tilde{L}, \tilde{e}_R, \tilde{u}_d, \tilde{d}_R$ which are both contained in the respective $SU(2)_L$ or $U(1)$ superfields. Additional superfields contain the SM bosons and their fermionic partners: the gluons g^a and gluinos $\tilde{g}^a$; the three weak bosons W_i and the winos $\tilde{w}_i$; and the $U(1)$ boson B and its partner the bino $\tilde{b}$. To cancel out gauge anomalies, the SM $SU(2)_L$ Higgs doublet of scalars becomes two doublets H_u and H_d, which then require two Higgs doublets of fermions for the higgsinos $\tilde{h}$.

2.3.1 R Parity and Dark Matter

The full MSSM Lagrangian can be found elsewhere [60]. Suffice to say, there are terms which permit lepton and baryon number violating interactions that can mediate proton decay, and give rise to interactions such as the one in Fig. 2.3. There are very stringent

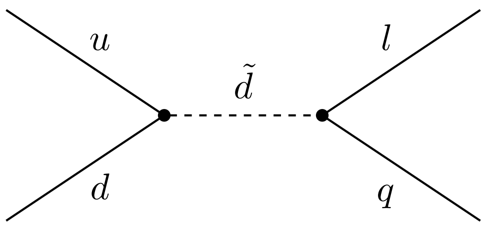

Figure 2.3: Example of a lepton and baryon number interaction which would mediate proton decay.

limits on proton decay; $\tau > 10^{33}$ years [11], so interactions such as these must be highly suppressed, if allowed at all. The class of SUSY models which do not permit lepton and baryon violating interactions have an additional symmetry in R parity, which is defined as

$$R = (-1)^{3(B-L)+s}, \tag{2.49}$$

where B is the baryon number, L the lepton number, and s the spin of the particle. A consequence of R parity conserving SUSY is that sparticles are always produced in pairs, and any sparticle decay will always result in another sparticle being produced. So any SUSY decay chain, as well as producing many SM particles, will always result in a single sparticle – the lightest of the SUSY spectra, so cannot decay further. This is then the Lightest Supersymmetric Particle (LSP), and must be stable. Cosmological bounds on light charged or coloured stable particles [11] imply the LSP (if it exists) must be neutral. A stable, neutral, weakly interacting LSP, key to the popularity of SUSY, then very naturally gives a DM candidate. The LSP, with a collider signature much like a neutrino, will exit a detector having deposited no energy as it interacts with none of its material. There will instead be an imbalance in momentum, leading to a missing transverse energy signature.

2.3.2 Unifying the forces

Another feature of SUSY which makes it very popular with the theory community is the natural unification of the weak, electromagnetic and strong forces at the Grand Unified Theory (GUT) scale. The strengths of each of these forces change with distance, or equivalently energy – their coupling constants 'run'. At very small distances, or very high energies, such as those at the time of the Big Bang, masses of any particles involved are completely negligible, and the strengths of interactions can be investigated. With the vanilla SM of Section 2.1, there is not a single point where the three coupling constants unite, or become one, unified interaction. However, when SUSY is added in, all three forces become unified at a single point around 10^{16} GeV [61], see Fig. 2.4.

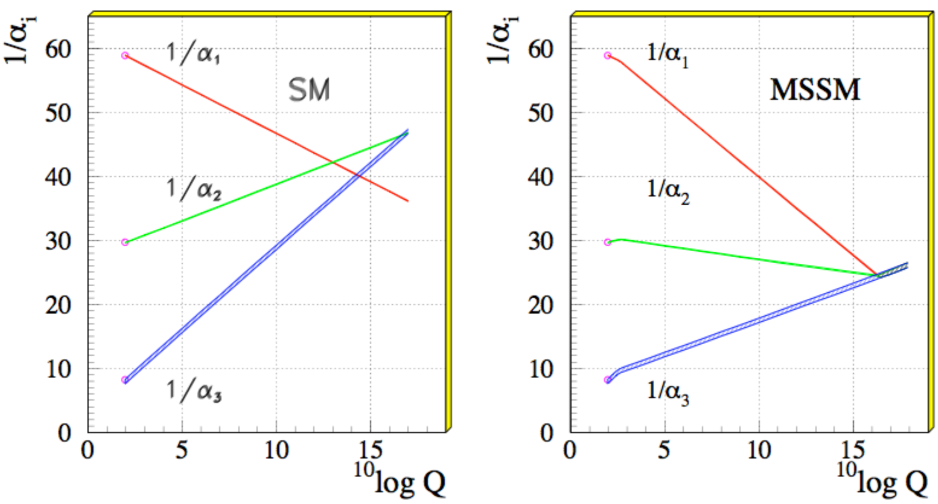

Figure 2.4: The running coupling constants of the electromagnetic, strong and weak forces with increasing energy or decreasing distance. Once SUSY has been added in, the three unify around 10^{16} GeV, hinting at a GUT. Taken from [62].

This very elegant picture of the early universe is very attractive: one single force dominated while the energy density was high enough, and then later, a transition occurred when the three forces became distinct. The idea of a GUT, with some higher symmetry group, that can dictate all of the behaviour we observe in the universe is very appealing to theorists.

2.3.3 Breaking Supersymmetry and Naturalness

We have mentioned that SUSY is a broken symmetry if it exists in nature. The possible mechanism of the spontaneous symmetry breaking is beyond the scope of this thesis, but different SUSY breaking mechanisms lead to many different sparticle phenomenologies [53]. It is usually assumed that the SUSY breaking occurs at some high scale $\sim M_{Pl}$, and that it is "soft" [63], which leads to logarithmic, rather than quadratic divergences. The correction to the Higgs mass then takes the form

$$\delta\, m_H^2 \sim \left(m_{\tilde{q}}^2 - m_q^2\right) \log \Lambda. \tag{2.50}$$

The largest contribution to $\delta\, m_H$ is from the top quark, because it is so much more massive than all other SM fermions at 173 GeV . To keep $\delta\, m_H$ reasonably small, and the fine tuning issue minimal, the supersymmetric partner to the top quark, the top squark $\widetilde{\mathrm{t}}$ should be fairly close in mass to 173 GeV . Figure 2.5 shows the correction to the Higgs mass due to the top quark loop, and the corresponding loop correction from the top squark, which acts to cancel the divergence in the Higgs mass out.

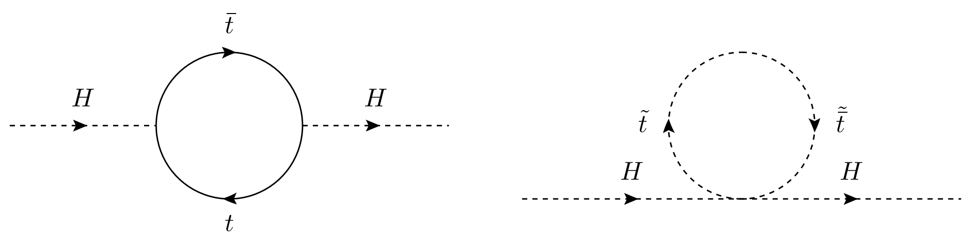

Figure 2.5: The loop contributing to the Higgs mass due to the top quark, left, and the cancellation of the loop due to the top squark, right.

Such naturalness arguments motivate a light $\widetilde{\mathrm{t}}$, and a bottom-up approach to any SUSY spectrum. The biggest Yukawa couplings come from the heaviest SM particles, i.e. the third generation. To keep corrections to the Higgs mass small, the third SUSY generation is expected to be the lightest, and in reach of the LHC [64, 65]. First generation squarks and sleptons can be much heavier, even up at the Plank scale, while keeping a natural SUSY.

2.3.4 Searching for Supersymmetry at Colliders

Having motivated SUSY as a extension of the SM which has the potential to very nicely solve the hierarchy problem, give us a DM candidate and unify the three fundamental forces at the GUT scale, we ask ourselves how best to search for any possible signs of it at a collider. In R parity conserving SUSY, the LSP exits the detector leaving nothing but an imbalance of momentum; at hadron colliders, this imbalance is evident in the transverse plane as $E_{\mathrm{T}}^{\mathrm{miss}}$. In addition, typical SUSY decay chains have multiple legs, as a heavy sparticle produced in the pp collision decays down the SUSY spectrum. A SM particle (which may itself decay) is emitted at each step until the energy is small enough that only the LSP can be emitted, along with a final SM particle. Each event has two such decay chains as the original sparticle is pair produced. The array of decays possible, as well as the energies involved, depend entirely on the SUSY spectrum considered, which in turn is dependent on the type of SUSY breaking. An example of this kind of SUSY decay chain is shown in Fig. 2.6. Here, the LSP is shown as $\tilde{\chi}_1^0$. Such $\tilde{\chi}^0$ states are a neutral superposition of higgsino, wino and bino states; the exact composition is again SUSY model dependent. Charged superpositions are written as $\tilde{\chi}^{\pm}$ and often feature in such decay chains.

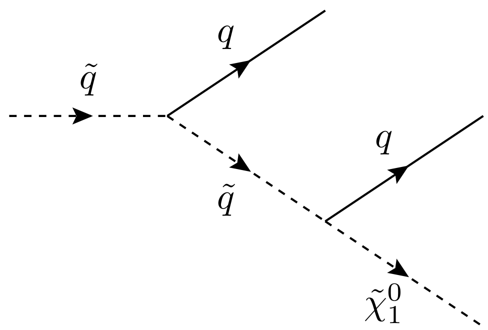

Figure 2.6: Example of a SUSY decay chain, in which there are several quarks emitted as well as the LSP. Two of these decay chains will be present in each event due to the pair production of the parent $\tilde{q}$.

To be sensitive to these SUSY signatures, which have high particle multiplicity and lots of energy in the final state, traditional searches have revolved around looking for multiple final state objects, plus a significant amount of $E_{\mathrm{T}}^{\mathrm{miss}}$. To be as model independent as possible, searches are generic. There are searches for multijet events (arising from a decay chain similar to that in Fig. 2.6), same or opposite sign dilepton events, multi-lepton events, events which have both leptons and jets, or photons, jets which are tagged as arising from a b-quark, events with lots of hadronic energy deposited (H_T): see Refs. [66–74]. Innovative methods of controlling the large backgrounds, particularly as a result of QCD multijet events, have been developed [75–77].

Stringent bounds were placed on the Compressed Minimal Supersymmetric Standard Model (CMSSM) during the first LHC run [78, 79]. It is a popular SUSY model which simply reduces the multitude of free parameters in the MSSM down to 5 by setting many of the masses to be equal. All scalar masses become m_0, all gaugino masses $m_{1/2}$, trilinear coupling are set to A_0, and the ratio of the VeV of the two Higgs doublets is $\tan\beta$. The fifth parameter is the sign of $\tan\beta$. Traditionally, searches are interpreted using the CMSSM as it produces a simple phenomenology, enabling mass scans in four dimensions (plus a sign) rather than over one hundred in the full MSSM. The phenomenology is also 'easily' discoverable: parameters are fixed at the GUT scale and extrapolated down to the electroweak scale (for example, the Z pole mass), making mass differences between particles relatively large and so decay products reasonably energetic. Limits from searches using the CMS detector are shown in Fig. 2.7. The lack of any sign of SUSY in these direct searches, as well as limits from indirect searches sensitive to the parameters of the CMSSM (such as $B_S \to \mu\,\mu$ [1]) have lead the community pursue less specific, alternative scenarios.

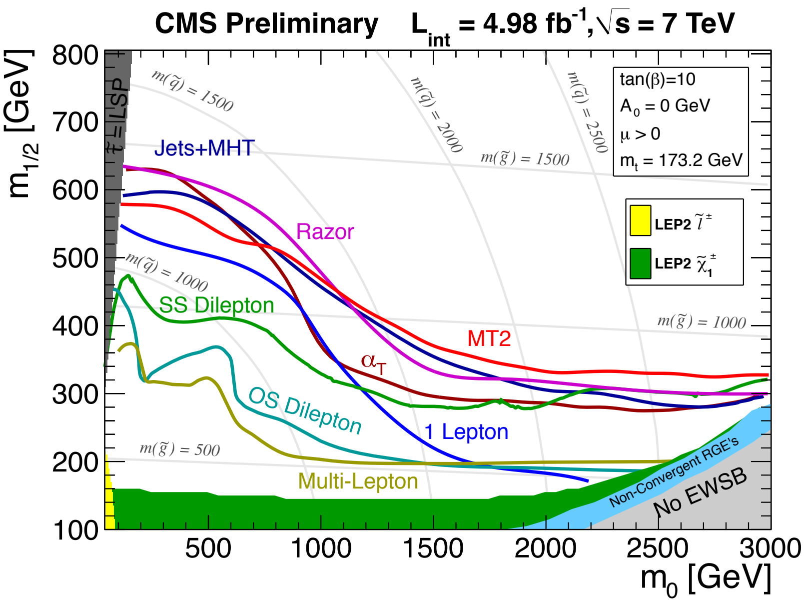

Figure 2.7: The limits on the $m_{1/2}, m_0$ CMSSM mass plane from CMS with the full 7 TeV dataset, taken from [80].

A more model independent approach has been adopted more recently, with the use of Simplified Model Spectra (SMS) [81–84], which allow searches to be interpreted in the mass planes of various sparticles: in the mass of the $\widetilde{\mathrm{t}}$, $\widetilde{\mathrm{b}}$, $\widetilde{\mathrm{q}}$ and $\widetilde{\chi}^0_1$ for example. All other sparticles than those probed are assumed to be very heavy and are integrated out.

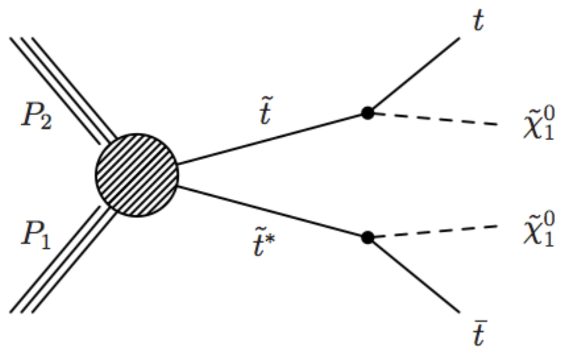

Figure 2.8: An example of a SUSY decay of the top squark. This is one of the simplified models probed by CMS at the LHC.

Figure 2.8 shows an example Feynman diagram for a particular decay of the $\widetilde{\mathrm{t}}$, one of the SMS hypotheses probed, which dominates if the top squark is heavy enough to produce an on-shell top quark when it decays. Other decays dominate when this is not true, which can then be targeted with searches that have different kinematics than that of Fig. 2.8: this will be the subject of Chapter 5. Such generic searches can also be simply applied to other models of BSM physics.

At 7 and 8 TeV, no evidence for SUSY has been found at the LHC; exclusion limits on squarks and gluinos are around 1 TeV at 95% Confidence Level (C.L.). Searches have ruled out huge swathes of phase space, see Fig. 2.7 and Fig. 2.9 that show the limits on the CMSSM and the combined CMS results on the $\widetilde{\mathrm{t}}$, $\widetilde{\chi}^0_1$ mass plane at SUSY 2013 respectively.

If SUSY is to persist as a convincing BSM theory, naturalness arguments in conjunction with a Higgs mass of $\sim$125 GeV imply that the third generation squarks should be light [86]. Either SUSY does not exist in a natural way and doesn't solve the theoretical problems in the SM that it has been proclaimed to, it is just out of reach at the 8 TeV LHC, or SUSY is somehow hidden. Fig. 2.9 has areas which are not covered by the exclusion regions, where it has been suggested that SUSY may be 'hiding'. Traditional searches loose sensitivity in these regions. For example, in the strip close to the kinematic limit, when the parent sparticle – $m_{\widetilde{\mathrm{t}}}$ in this case – is close in mass to $m_{\widetilde{\chi}^0_1}$, decay products become very soft, so would in hidden amongst the high QCD background. This kind

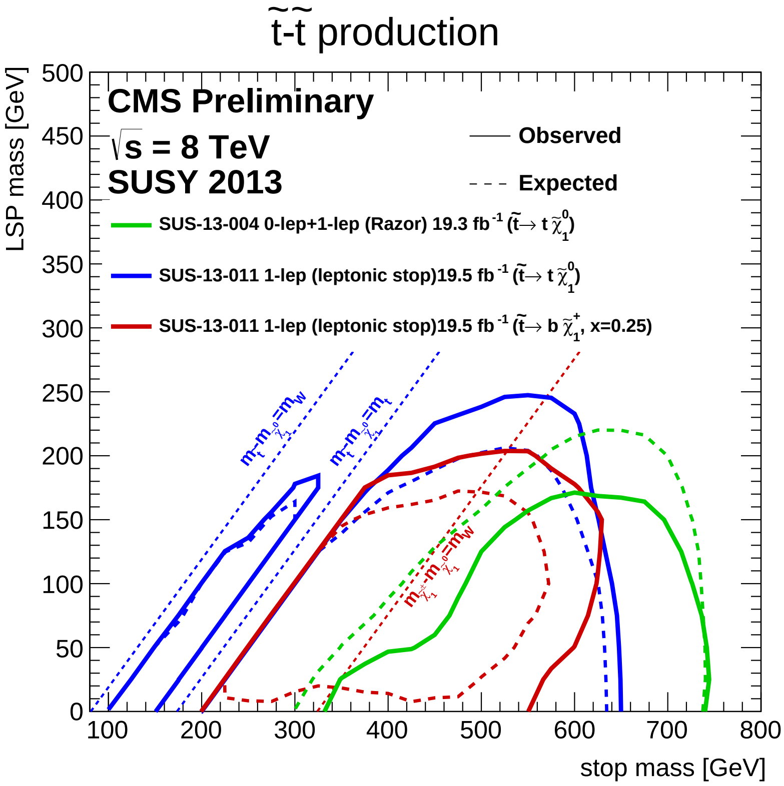

Figure 2.9: The limits on the $\tilde{t}$, $\tilde{\chi}^0_1$ mass plane from CMS at SUSY 2013 [85].

of mass spectrum, which is compressed, would not show up in the traditional SUSY searches that demand lots of visible energy: a different approach is necessary.

2.3.5 Supersymmetry with Compressed Mass Spectra

SUSY has compressed mass spectra when the symmetry breaking dictates that the various states are close in mass, for example see Fig. 2.10. Particularly, the LSP is close in mass to the Next-to-Lightest Supersymmetric Particle (NLSP), which, in many scenarios, is the $\tilde{t}$. There is no reason to assume that nature would not 'prefer' a compressed spectra: to keep as wide a net as possible over the SUSY phase space, compressed scenarios should be probed – we should look for both the types of spectra shown in Fig. 2.10. Further, it is not just the lack of any evidence for SUSY in the bulk phase space regions, where the mass difference between the LSP and the next lightest sparticle is typically > 100 GeV, but there are also phenomenological arguments which motivate the search for compressed SUSY, with a light $\tilde{t}$.

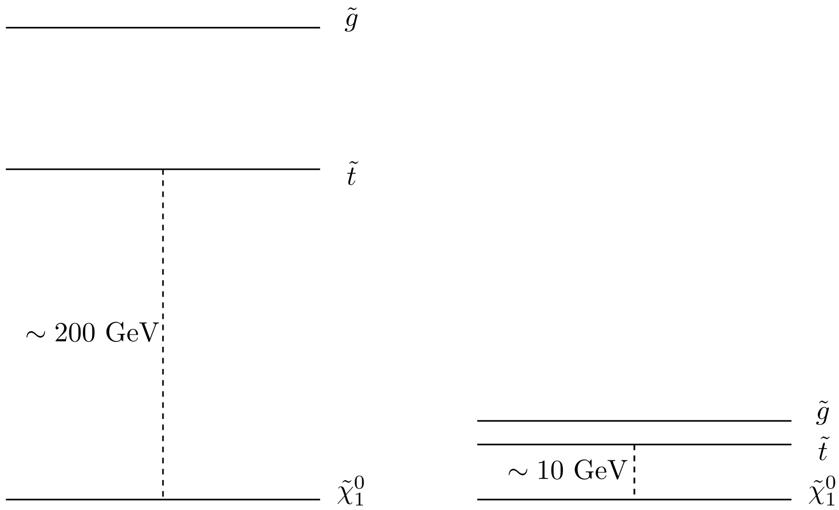

Figure 2.10: An example SUSY spectrum in the bulk region, left, and for a compressed spectrum, right. The mass difference between the NLSP and the LSP, here the $\widetilde{\mathrm{t}}$ and $\widetilde{\chi}^0_1$ receptively, is much reduced for the compressed scenario.

Any BSM candidate for DM must give the correct energy density of dark matter, which has been accurately measured by Wilkinson Microwave Anisotrophy Probe (WMAP) and the Planck space telescope [44, 87]. Any SUSY model, if it is to explain the origin of DM as the LSP, must therefore give the correct DM relic density (if nothing else is acting to increase or decrease the relic density). This requirement can dictate the nature of the neutralino (the DM candidate) [88, 89]. If the neutralino is a superposition of bino states, then the relic density is too large; if it is instead a composition of higgsino or wino states, then it is too small. However, if the neutralino is bino-like but has a few tens of GeV mass splitting with the lightest $\widetilde{\mathrm{t}}$, the correct relic density can be achieved [90–92].

Any compressed scenario will lead to soft decay products, as the energy from the parent sparticle goes mostly into producing the daughter particles with little left to boost the decay products. The question of how to efficiently select these events then presents itself – it is very difficult to pick out events that contain only a few soft particles; they would be lost in the SM electroweak, $\mathrm{t\bar{t}}$ and QCD events. Similarly, the $\widetilde{\chi}^0_1$ at the end of the decay chain will also be very soft, so $E_{\mathrm{T}}^{\mathrm{miss}}$ in each event is also small. Instead of looking for the decay products themselves, it is then more useful to search for states which are produced in association with the parent sparticles. Initial State Radiation (ISR) can lead to the emission of a high energy gluon or quark, giving a hard jet. It will also give a boost to the system, such that the $\widetilde{\chi}^0_1$ also have more momentum, and thus there will be a significant amount of $E_{\mathrm{T}}^{\mathrm{miss}}$. Such an event will then have a clear signature of one high momentum jet and large $E_{\mathrm{T}}^{\mathrm{miss}}$, where the decay products are too soft to observe. While

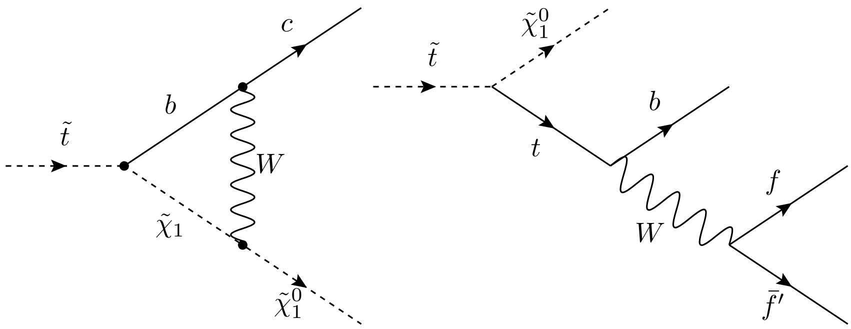

Figure 2.11: Feynman diagrams to show two contributing processes to the decays of the top squark: $\widetilde{\mathrm{t}} \rightarrow c\widetilde{\chi}_1^0$ (left) and $\widetilde{\mathrm{t}} \rightarrow b\widetilde{\chi}_1^0 f\bar{f}'$ (right).

the production cross section of a process with an ISR jet is of course lower than without, due to the additional factor of α_S, the gain in sensitivity to the signal far outweighs the lower event yield.

2.4 Decays of the top squark

We have discussed in the previous section the importance of a light top squark for natural SUSY. In order to optimise any search for such a light top squark, it is important to consider its decays in different regions of parameter space [93, 94].

For the case when the mass difference between the top squark and the LSP is greater than the mass of the top quark, $m_{\widetilde{\mathrm{t}}} - m_{\widetilde{\chi}_1^0} > m_t$, the dominant decay mode is simply $\widetilde{\mathrm{t}} \rightarrow t\widetilde{\chi}_1^0$. The Feynman diagram for $\widetilde{\mathrm{t}}$ pair production followed by this decay is shown in Fig. 2.8.

However, when the mass difference is less than the top quark, $m_{\widetilde{\mathrm{t}}} - m_{\widetilde{\chi}_1^0} < m_t$, things become more complicated. While the mass difference is above the mass of the W, $m_{\widetilde{\mathrm{t}}} - m_{\widetilde{\chi}_1^0} > m_W$, the three body decay mode $\widetilde{\mathrm{t}} \rightarrow Wb\widetilde{\chi}_1^0$ dominates, as the W can be produced on-shell. As the mass difference becomes smaller still, $m_{\widetilde{\mathrm{t}}} - m_{\widetilde{\chi}_1^0} < m_W$, both the flavour changing neutral current decay $\widetilde{\mathrm{t}} \rightarrow c\widetilde{\chi}_1^0$ and the four body decay $\widetilde{\mathrm{t}} \rightarrow b\widetilde{\chi}_1^0 f\bar{f}'$ can occur, where f is any fermion. Examples of Feynman diagrams that contribute to these are shown in Fig. 2.11. While the precise branching fraction of these decay modes is rather model dependent, it is usually assumed that due to phase space arguments, the four body decay is suppressed and $\widetilde{\mathrm{t}} \rightarrow c\widetilde{\chi}_1^0$ dominates [93]. Figure 2.12 summarizes the decays of the top squark, showing the relevant decay for the different kinematic regimes of $\widetilde{\mathrm{t}}$ and $\widetilde{\chi}_1^0$ mass.

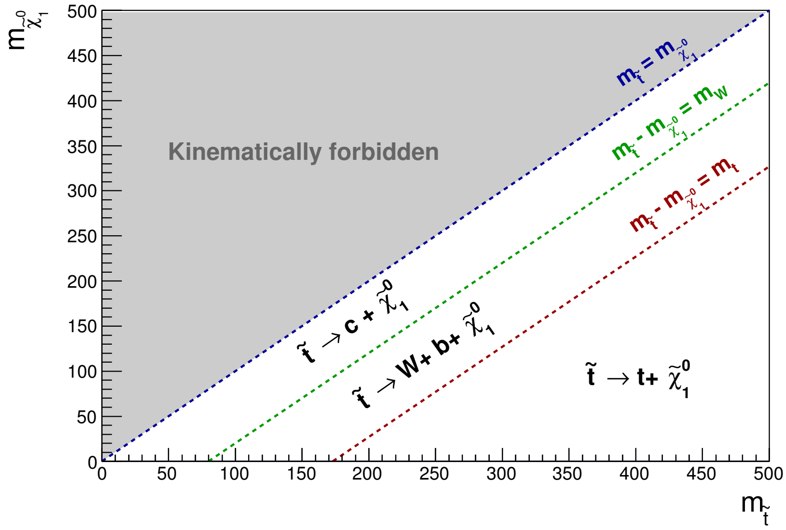

Figure 2.12: Phase space of the top squark and LSP. The grey region is kinematically forbidden: $m_{\tilde{\chi}_1^0} > m_{\tilde{t}}$ is at odds with the LSP definition. The coloured dotted lines and labels define each kinematic region, and the dominant $\tilde{t}$ decays are shown, where we have neglected the four body decay in the region where $m_{\tilde{t}} - m_{\tilde{\chi}_1^0} < m_W$.

In light of the arguments for searching for compressed SUSY, particularly in the third generation, Chapters 5 and 7 will describe searches for light stops decaying to a charm quark and a neutralino, using events with a monojet topology.

Chapter 3

The LHC and CMS experiment

"Insanity: doing the same thing over and over again and expecting different results."
— Albert Einstein, 1879 - 1955

Probing the physics of the SM and beyond at the TeV scale is only possible with the technologically unparalleled apparatus situated at the CERN. This chapter will introduce the hugely complex machinery of the LHC , which provides proton-proton collisions at centre-of-mass energies in excess of $\sqrt{s} = 7$ TeV , and outline the main features of the CMS experiment, of which the author is a member, with particular focus on those features relevant to the material presented in this thesis. Section 3.1 presents the main features of the LHC, and Section 3.2 provides an overview of the CMS detector. Physics bject reconstruction is described in Section 3.3 and the CMS trigger system is discussed in Section 3.4.

3.1 The LHC

The LHC is the world's largest and most energetic synchrotron particle collider. Housed in the tunnel built for the Large Electron-Positron Collider (LEP) collider that operated during the 1990's at CERN, the LHC is a double ring circular collider 27 km in circumference, and sits on the bedrock beneath the Franco-Swiss border, close to Geneva, Switzerland. It is designed for both proton-proton (pp) and heavy ion (PbPb) collisions at a centre of mass energy $\sqrt{s} = 14$ TeV and luminosity of $10^{34}\text{cm}^{-2}\text{s}^{-1}$.

Currently the world's only operating collider able to study physics directly at the TeV scale, the LHC consists of thousands of superconducting magnets which act to accelerate, bend and focus two beams of protons (or heavy ions) that circulate in opposite directions around the accelerator. A chain of accelerators, shown in Figure 3.1 and culminating with the SPS, inject bunches of approximately one hundred billion protons 25 or 50 ns apart at $\sqrt{s} = 450$ GeV into the two beams of LHC. Oscillating electric fields provided by 1232 superconducting dipole magnets act to accelerate the beams up to the operating centre of mass energy, which for the data used in this thesis was $\sqrt{s} = 8$ TeV, with bunch crossings every 50 ns. Once protons are accelerated to the operational $\sqrt{s}$, the LHC acts as a storage ring, and collisions can occur. Either side of four points around the LHC ring, very high precision magnetic fields, provided by quadrupole and higher order multipole magnets, position and focus the beams such that each bunch has a diameter of 16 μm. The chance of a pp collision with large momentum transfer at the four interaction points around the LHC ring is thereby increased, and the number of such collisions per bunch crossing, termed pile-up (PU) for the data used in this thesis was $\sim$20.

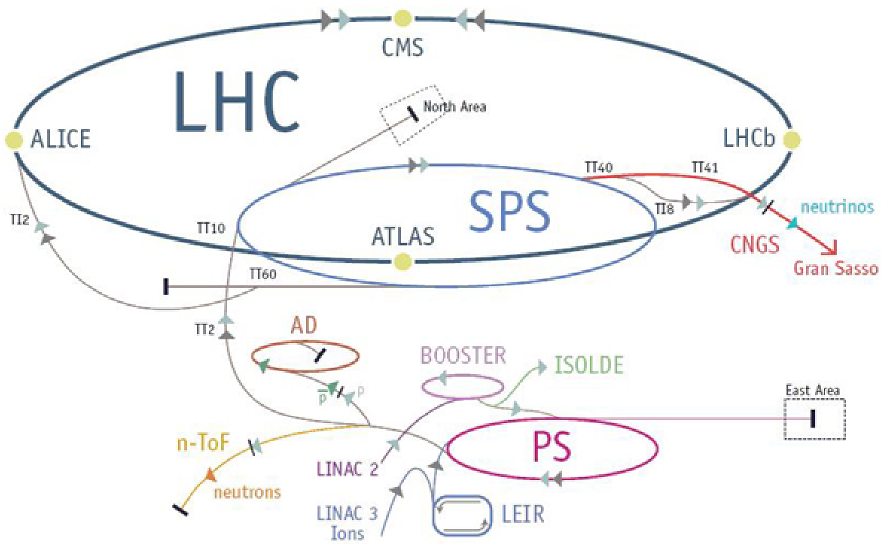

Figure 3.1: The LHC accelerator ring, showing the locations of the four main experiments at the four collision points.

Interaction points are at the centre of four large particle detectors, shown in Figure 3.1: A Large Ion Collider Experiment (ALICE) [95], A Toroidal LHC ApparatuS (ATLAS) [96], CMS [97] and Large Hadron Collider Beauty (LHCb) [98]. They act to identify particles produced as a result of a pp or PbPb bunch crossing through a combination of tracking and calorimetry, in order to reconstruct and measure physical processes, to test currently accepted theories and search for new physics.

3.2 The CMS Detector

The CMS detector is a general purpose particle detector situated at Point 5 on the LHC ring, designed to carry out many different measurements for various physics goals. Close to 4π solid angle reconstruction with efficient particle identification and reconstruction allows measurements of photons, muons, electrons, taus, hadronic showers and missing transverse momentum. A diagram of CMS is shown in Figure 3.2. It is 21.6 m long, 14.6 m in diameter and weighs 12500 T. It consists of different sub-detectors, each of which measures a different particle or property, and is built around a central 12.5 m long 4 T superconducting solenoid magnet and its iron return yoke. CMS consists of a barrel region, containing the solenoid, and endcaps to extend the forward and backward coverage.

The different sub-detectors are arranged in an onion structure. Closest to the beam line is the silicon tracking system. A very highly resolution pixel detector lies closest to the interaction region, followed by a granular strip detector. Charged particle momenta measurements are made using the curvature of tracks in the uniform magnetic field provided by the solenoid, as well as measurements of displaced vertices and impact parameters which are essential for identifying heavy flavor decays. Energy measurements are provided by the calorimeters, which lie outside the tracker; the Electromagnetic Calorimeter (ECAL) and Hadronic Calorimeter (HCAL). The highly granular ECAL consists of 70,000 transparent lead tungstate crystals. As electrons and photons pass through, they cause electromagnetic showers in the crystals, which produce scintillation light. The sampling HCAL consists of slabs of brass interleaved with plastic. Incident hadrons shower when passing through the absorber (brass), causing scintillation light to be produced in the active material (plastic) as the shower passes through. Scintillation light produced in the crystals, or plastic, is collected by photodetectors and used to infer the incident particle energy and position. The solenoid lies outside the HCAL and provides a 3.8 T axial magnetic field. Embedded in the iron return yoke of the magnet sits the muon system. Three different types of muon detectors are used to identify muons and make momentum and charge measurements over a large kinematic range. More information on the CMS detector can be found in Ref. [97].

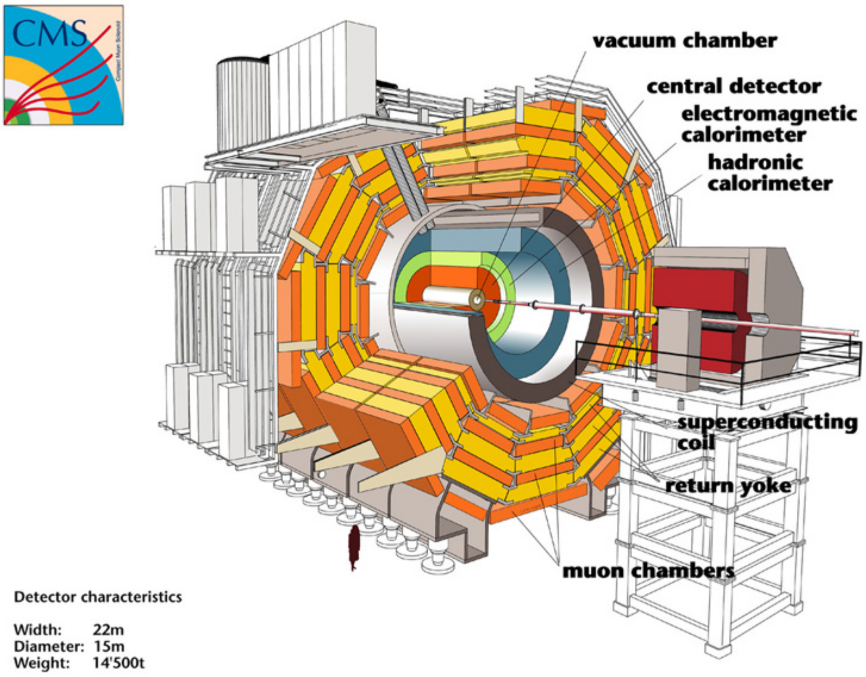

Figure 3.2: The CMS detector, with the main subsystems labelled.

CMS uses a right-handed coordinate system: the x-axis points south towards the centre of the LHC ring, the y-axis points vertically upwards and the z-axis is in the direction of the beam, where positive z is to the West. More natural is the coordinate system defined in terms of r, ϕ and θ. The azimuthal angle ϕ is measured from the x-axis in the xy plane, where the radial component is denoted r. The polar angle θ is defined in the rz plane, and the pseudorapity

$$\eta = -\ln\tan(\theta/2). \tag{3.1}$$

Convention is that the position of a particle is described in terms of η and ϕ, where $\eta = 0$ is along the y-axis and $\eta = \infty$ is along the beam direction; and $-\pi < \phi < \pi$. The distance between particles is commonly described in terms of the variable $\Delta R = \sqrt{\Delta\phi^2 + \Delta\eta^2}$.

The LHC is a hadron collider, and as such, collides non-fundamental particles. Inelastic collisions with large momentum transfer can occur between component quarks and gluons, however in a single bunch crossing there will also be many low energy, elastic, soft scatters, as well as the remnant part of any protons that have had a hard collision. As a result, the forward and backward directions are highly populated environments and therefore difficult to instrument due to high occupancy and radiation damage. CMS has endcaps to extend the detector coverage at high η, however it is not possible to reconstruct the momentum of a single interaction in the direction of the beam. Additionally, interesting physics is a result of a hard collision, where energy is available for the creation of new particles. It can be characterized by the amount of energy in the transverse (xy) plane. For these reasons, particle energy and momenta are described only in the transverse plane, where conservation laws can be applied. By conserving energy and momentum in the transverse plane, any imbalance can be assigned to a particle leaving the detector without any trace; for example from a neutrino, or, from new physics processes such as DM production A nearly hermetic detector (with close to 4π coverage in solid angle) allow excellent particle reconstruction and measurements of missing transverse energy, the 'tell-tale' sign of new physics, and make CMS perfectly suited to searching for physics beyond the SM.

3.2.1 The Tracking System

The tracker is designed for precise and efficient measurement of charged particle trajectories (and therefore position and momentum) as they emerge from the interaction point. Additionally, reconstruction of any secondary vertices is crucial for identifying heavy flavor decays such as jets that originate from b-quarks.

The LHC provides bunch crossings every 25 or 50 ns, resulting in $\sim$ 20 pp interactions, giving rise to of order 1000 particles. All of these traverse the tracker. The granularity of the tracker must be such that one can determine which of the $\sim$ 20 pp vertices each of the particles come from, and the electronics fast enough that the information is sent on in time for the next bunch crossing to arrive. With such high particle fluxes, the tracker is also subject to a huge amount of radiation damage. These conditions must be dealt with using the least amount of material possible in order to limit multiple scattering, photon conversion, bremsstrahlung and nuclear interactions. To meet such criteria, and to have an estimated lifetime of 10 years, the tracker is constructed entirely from silicon.

The tracker consists of an all silicon pixel and strip detector. Measuring 5.8 m in length and 2.5 m in diameter, with a total active area of 200 m^2, it surrounds the interaction region. The pixel detector has three layers in the barrel, at radii of 4.4 cm, 7.3 cm and 10.2 cm. In the endcaps, there are two disks at distances $z = \pm 34.5, \pm 46.5$ cm. The strip detector has a length of 5.8 m and a diameter of 2.4 m, and is composed of four subsystems: the Tracker Inner Barrel (TIB), Tracker Outer Barrel (TOB), Tracker Inner

Disks (TID) and Tracker Endcaps (TEC). The CMS tracker geometry is shown in Figure 3.3.

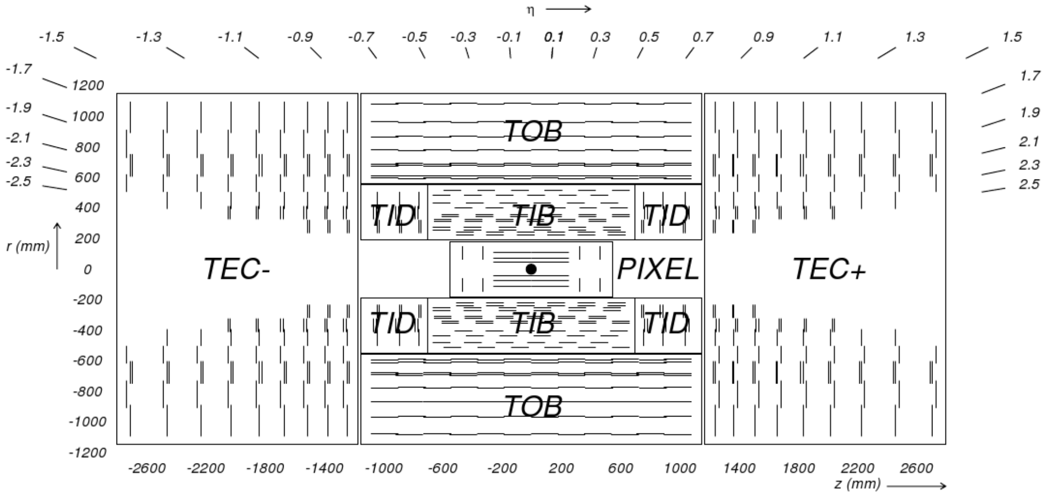

Figure 3.3: The CMS tracker, shown in the rz plane. The pixel detector is shown at the centre of the tracker, closest to the interaction region (shown by the black dot), and the strip detector surrounds it. The different subsystems of the strip detector are shown. Taken from Ref. [97].

The energy resolution of the tracker is shown in Figure 3.4, for samples of single muons with p_{T} of 1, 10 and 100 GeV . For a 100GeV muon, the resolution is 1-2% up to $|\eta| = 1.6$. Lower momentum objects have a better energy resolution as their tracks have increased curvature.

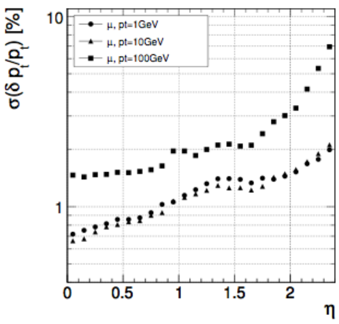

Figure 3.4: The energy resolution as a function of $|\eta|$ for CMS tracker, shown for single muons with $p_{\mathrm{T}} = 1$, 10 and 100 GeV .

3.2.2 The Electromagnetic Calorimeter

High resolution photon and electron position and energy measurements are provided by the lead tungstate ($PbWO_4$) crystal ECAL, which covers pseudorapidty up to $|\eta| < 3$. It is made up of the Electromagnetic Calorimeter Barrel (EB), covering the range $0 < |\eta| < 1.479$, and the Electromagnetic Calorimeter Endcap (EE), covering the range $1.479 < |\eta| < 3$.

Both fast response times (80% of scintillation light is emitted in 25 ns) and radiation hardness are required from the ECAL, motivating the choice of material. In addition, it is very dense (8.28 gcm^{-1}), has a short radiation length ($X_0 = 0.89$ cm), and small Molière radius (2.2 cm), making it well suited to a compact, fine granularity calorimeter. Arranged in a quasi-projective geometry, 61,200 crystals in the barrel and 7,324 crystals in the endcaps are tapered in shape and angled at 3° to ensure that particle trajectories avoid cracks between them. Barrel crystals have a front face of 22×22 mm^2 and a length of 23 cm, corresponding to 25.8 X_0. Endcap crystals have a front face of 28.6×28.6 mm^2 and length corresponding to 24.7 X_0. Electromagnetic showers are therefore expected to be contained within one crystal length, so only a single layer of crystals is needed. A preshower detector is place in front of the endcaps, with a thickness of $3X_0$, in the range $1.653 < |\eta| < 2.6$, in order to distinguish between single photons and photon pairs resulting from neutral pion decay. The ECAL geometry is shown in Figure 3.5.

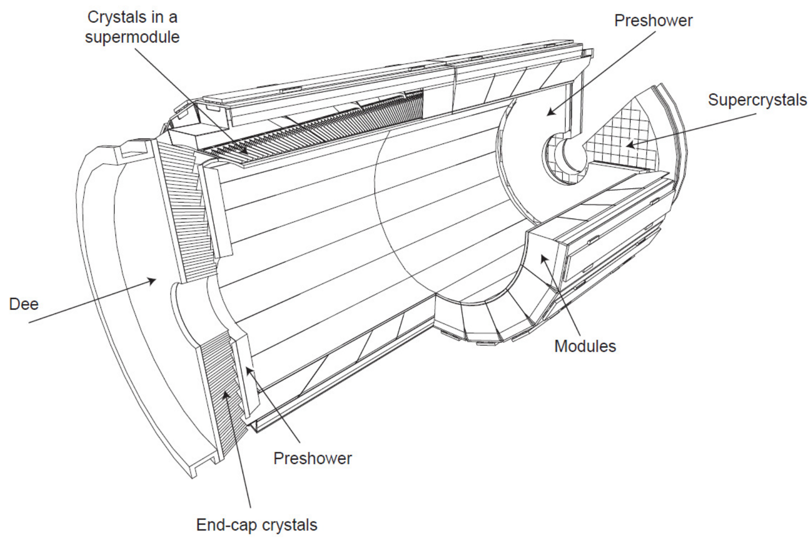

Figure 3.5: Geometric view of the CMS ECAL. Barrel crystals are arranged in modules and supermodules, and endcap crystals arranged in supercrystals. Also shown is the preshower detector.

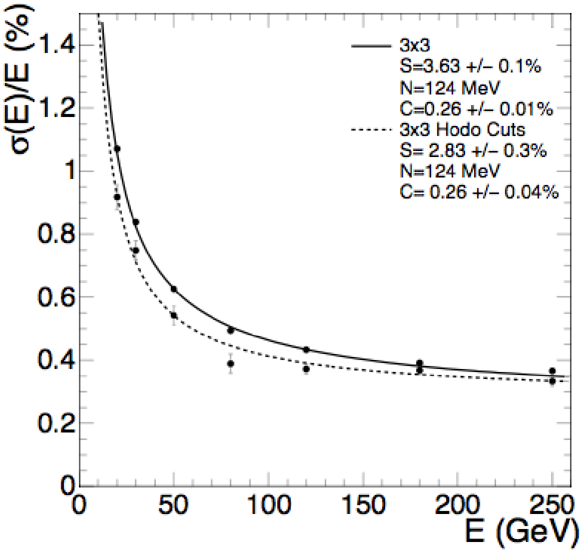

Figure 3.6: The energy resolution of an ECAL supercrystal, measured in a test beam. The lower set of points along the dashed line correspond to the energy measured in an array of 3×3 crystals, where events fall within a 4×4 mm region in the central crystal.

The very dense material $PbWO_4$ causes incident photons and electrons to shower. Resulting pair produced electrons and positrons, and radiated photons, cause scintillation light in the transparent, polished crystals. The amount of light produced is proportional to the incident particle energy, and is collected by an Avalanche Photo-Diode (APD) on the end of each crystal in the barrel, and a Vacuum Photo-Triode (VPT) in the endcaps. [check if use these acronyms again] These photodetectors also have to be radiation hard and operate successfully in the 3.8 T magnetic field, while providing significant amplification to signal. Both the crystal and photodetector performance has a strong temperature dependence, so the ECAL is kept at a constant temperature of 18° via a water cooling system, and is stable to $\pm 0.05\ ^\circ$C.

The energy resolution of the ECAL can be parametrised using the following equation:

$$\left(\frac{\sigma}{E}\right)^2 = \left(\frac{S}{\sqrt{E}}\right)^2 + \left(\frac{N}{E}\right)^2 + C^2, \tag{3.2}$$

where S is due to stochastic scattering, N is due to noise and C is the constant term. Measurements in test beam are shown in Figure 3.6, where the terms were found to be: $S = 2.8\%$, $N = 0.12$ GeV and $C = 0.30\%$.

3.2.3 The Hadronic Calorimeter

The HCAL provides complementary energy measurements of hadronic showers, crucial for measuring jets and missing transverse energy. It is a sampling brass calorimeter, built from alternating layers of large, absorbing brass plates, interleaved with scintillating plastic tiles arranged in trays. Sitting within the bore of the solenoid, the Hadron Barrel (HB) covers pseudorapidity $|\eta| < 1.3$, and the Hadron Endcaps (HE) on each side enclose $1.3 < |\eta| < 3$. To attain a most hermetic detector, there is also a Hadron Forward (HF), which extends coverage right up to $|\eta| < 5.2$.

The quality of the HCAL's measurements is dictated by the fraction of the hadronic shower that passes through the scintillator; the plastic must be thick enough to catch the majority of the shower. This demand for radial extension is at odds with the location of the HCAL, from the outer edge of the ECAL at $r = 1.77$ m, and the inner edge of the solenoid at $r = 2.95$ m. Providing a compromise, an outer hadronic calorimeter, Hadron Outer (HO), is placed outside of the vacuum tank of the magnet and supplements the HB. Using the solenoid coil as absorber material, it can identify late starting showers, providing sufficient containment for 11.8 interaction lengths.Five rings of HO are arranged along the z-axis of the detector, where the central ring at $\eta = 0$ has two layers at $r = 3.82$ m and 4.07 m, and the rest have a single layer at $r = 4.07$ m. Figure 3.7 shows the geometry of the HCAL.

Hadron showers are created in the brass absorber plates, through nuclear interactions in the material, and the plastic scintillator tiles produce blue-violet light when the shower passes through. It is read out using wavelength shifting fibres, sending the now green light down transparent fibres to Hybrid Photodetectors (HPD) which produce an electrical signal proportional to the incident hadron energy. The first layer of plastic tiles are placed in front of the first absorber plate in order to sample the incoming shower as it develops in the material between the ECAL and the HCAL. The final layer of scintillator placed after the final brass plate to catch any late developing showers. There are 70,000 plastic scintillator tiles in the HB and 20,916 tiles in the HE.

The HF uses a different technology in order to cope with the much harsher environment in which it is situated. With an average energy of 760 GeV deposited in the HF per pp collision at LHC design energy, peaking at the highest rapidity point closest to the beam line, radiation hardness and occupancy requirements demand alternative materials. Steel absorber plates are embedded with scintillating quartz fibres, which act to detect the

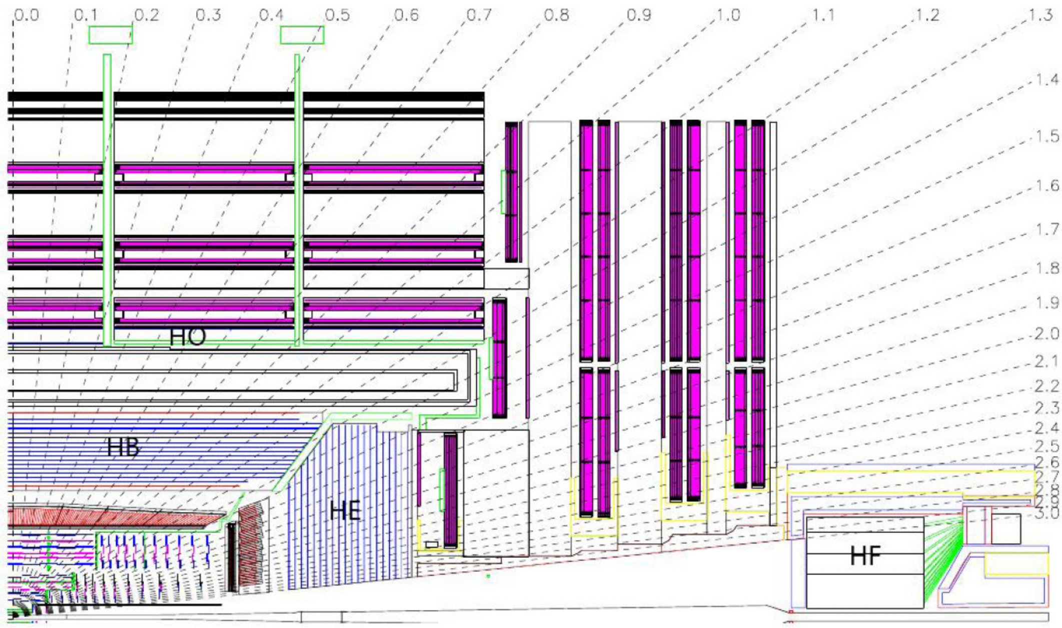

Figure 3.7: Longitudinal view of the CMS HCAL. Locations of the HB, HO, HE and HF are shown with values of η . The purple regions represent the muon detectors which further restrict the volume of the HO.

Cherenkov light emitted by charged particles in the shower. It is therefore most sensitive to the electromagnetic component of the shower.

The energy resolution of the HCAL was measured in pion beam tests. The energy response and resolution are shown in Figure 3.8, and the fractional energy response is parametrised as $\frac{\sigma}{E} = \frac{120\%}{\sqrt{E}} \oplus 6.9\%$.

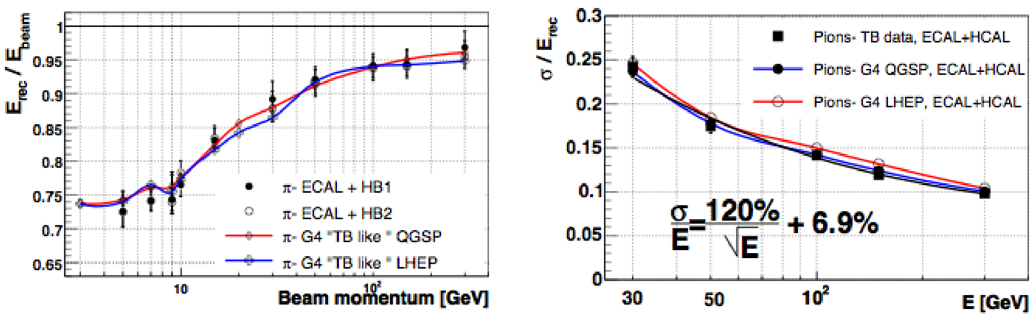

Figure 3.8: The raw energy response (left) and fractional energy resolution (right) as a function of energy, for pions, in team beam data.

3.2.4 The Muon System

Muons are a powerful tool for recognising signs of interesting physics. A relatively easy experimental signature to identify, muons can provide excellent 2- or 4-particle mass resolutions as, due to their larger mass, they do not suffer large radiative losses (as electrons do). Muon reconstruction is therefore a central design feature. Embedded in the iron flux-return yoke of the solenoid, the muon system combines three methods of gaseous detection to identify, carry out high resolution momentum measurements, and trigger events, up to $|\eta| < 2.4$. Figure 3.9 shows a cross section of one of the five wheels that make up the barrel section of muon system; there are also two planar endcaps which sit at either end of the detector and enclose it.

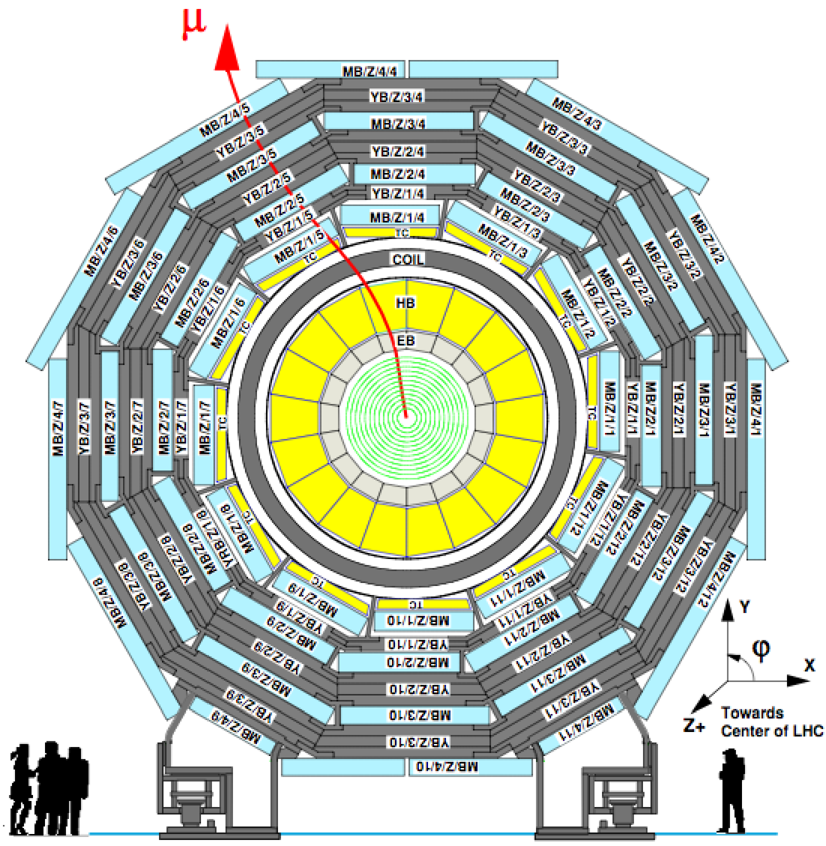

Figure 3.9: One of the 5 wheels of the barrel of the CMS muon system. Gaseous detectors are embedded in the iron return yoke of the solenoid; due to the small residual magnetic field in the barrel, DTs are used.

In the barrel ($|\eta| < 0.9$), magnetic flux is concentrated in the iron return yoke so the residual field is very small. There is also a low muon rate and neutron induced background, so DT chambers are used. In the endcaps ($0.9 < |\eta| < 2.4$), magnetic field and muon rate are much higher, so Cathode Stripe Chambers (CSCs) are used instead; they have a faster response time, higher granularity and better radiation hardness. Both the DT and CSCs have excellent position resolution. An additional system of Resistive Plate Chambers (RPCs) in both the barrel and endcaps provide an independent signal which has good time resolution (and poorer position resolution) and serves as a trigger.

By combining information from the tracker, and from either the DT or CSCs and RPCs, CMS has excellent muon reconstruction. Precise momentum resolution is achieved for the kinematic range, from 10 GeV to > 500 GeV , shown in Figure 3.10.

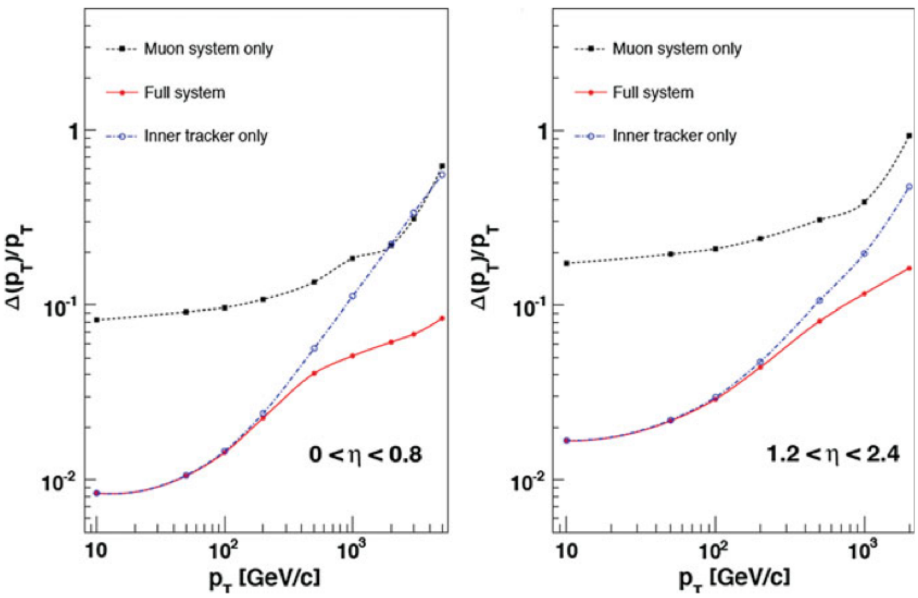

Figure 3.10: Muon transverse momentum resolution, shown as a function of muon p_{T} in the barrel (left) and the endcaps (right). The resolution of the tracker and muon system is shown, and the enhancement gained by combining the information.

3.3 Event Reconstruction

It is by piecing together the information from the various subsystems of the CMS detector that, for example, a track in the tracking system, or an energy deposit in the HCAL, can be attributed to a particle or "physics object". Figure 3.11 shows a slice of the whole detector with each of the main physics objects traversing it: muons, electrons, photons, and charged and neutral hadrons. Each of these leaves a different signature. Charged particles leave tracks in the silicon tracker, curved under the influence of the magnetic field. Electrons and photons cause electromagnetic showers, leaving energy deposits in the ECAL. Hadrons penetrate further, showering and leaving energy deposits in the HCAL. Muons are the only visible particles to reach the muon system, where they leave tracks.

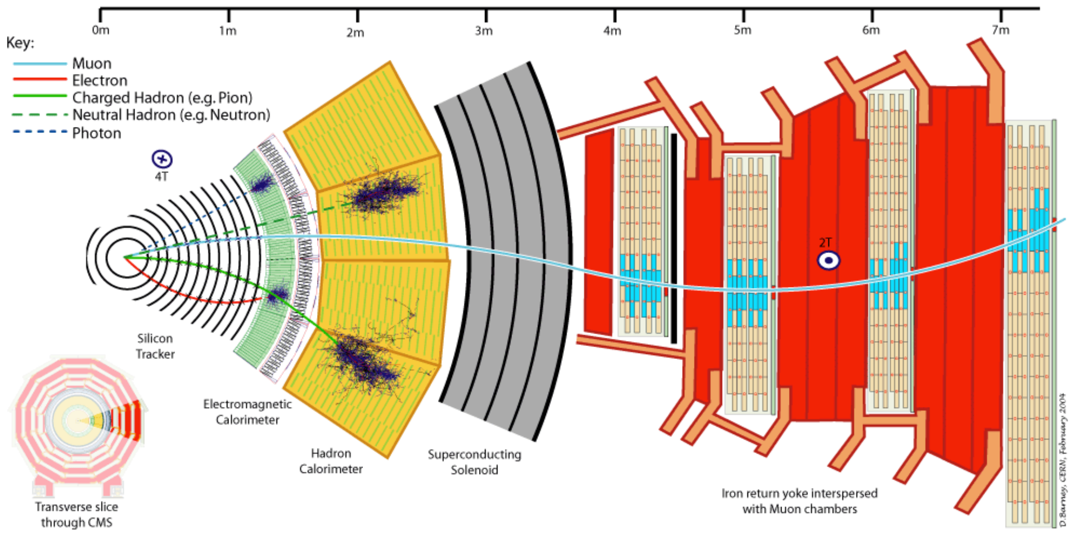

Figure 3.11: A slice of the CMS detector is shown, with various particles, or physics objects, traversing it. By combining information from each of the subdetectors, each of the particles produced in an event can be identified and the whole event reconstructed.

Particles can then be identified by combining tracking information with data from the calorimeters and muon system. If there is an energy deposit in the ECAL, the only way to distinguish between a photon or electron is by looking to see if there are hits in the tracker, leading to the position of the electromagnetic shower in the calorimeter. Similarly, the momentum measurement of the electron, determined using the curvature of the track it leaves (also used to reconstruct its charge), can be combined with the energy measurement made using the amount of scintillation light produced in the ECAL to get a better resolution. If there is no track leading to the electromagnetic shower, a photon is instead reconstructed. Hadronic showers in the HCAL due to charged and neutral incident hadrons can also be distinguished by their tracks. A muon will leave the tell-tale sign of hits in the tracker, and hits in the outer muon chambers, where position, momentum and charge measurements from both ensure the initial track in the silicon tracker matches up to the track in the muon system. Dual measurements also lead to enhanced resolution.

Below is a summary of the object reconstruction most relevant to the physics analysis described in Chapter 5. More information can be found in Ref. [99].

3.3.1 Jets

Copious numbers of quarks and gluons are produced during pp collisions in CMS, a consequence of the huge QCD cross section. Through the strong interaction they fragment and immediately hadronise, and a spray of hadrons is produced in the direction of an initial quark or gluon. Various algorithms have been developed in order to group the spray of hadrons into a "jet", and assign an energy, direction and transverse momentum to it.

In the analysis presented in this thesis (and in general at CMS), the anti-k_T algorithm [100] is used with a distance parameter, $R = 0.5$. It behaves like an idealised cone algorithm, using a distance parameter to cluster particles into cone shapes, with a radius R. Soft particles are clustered with nearby hard particles rather than with themselves, leading to conical jets, which – crucially – are resilient to soft radiation on the boundary of the cone. Likewise, the area of the jet is unaffected by soft radiation on the boundary, and is equal to πR^2. These features make the anti-k_T algorithm the preferential jet algorithm at CMS, due to its insensitivity to soft radiation that arises from sources such as PU; see Figure 3.12.

Several types of jets exist at CMS, in which the anti-k_T algorithm is given different inputs. Calorimeter (Calo) jets use information from the calorimeter only. ECAL crystals are grouped in 5×5 arrays into "towers", which measure 0.087×0.87 in $\Delta\phi \times \Delta\eta$ space (in the barrel region) and are matched to aligning blocks of HCAL. The sum of the energy deposits in both layers of calorimeter are used as inputs to the jet algorithm, where towers are treated as massless and an η dependent energy threshold has been placed on each tower to reduce the effect of instrumental noise.

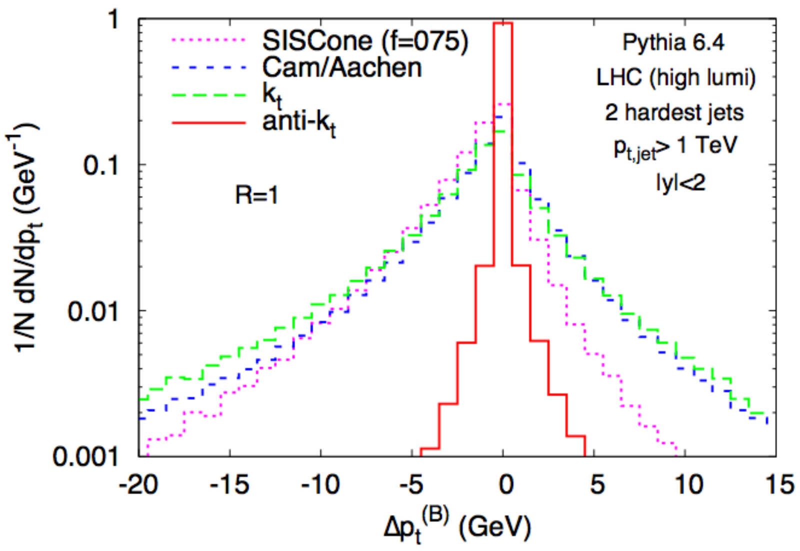

Figure 3.12: The relative insensitivity of the anti-k_T algorithm to PU is shown, compared to other common jet algorithms. The distribution of back reaction, corresponding to the net change in p_T to each of the two hardest jets (where each jet has $p_T > 200$ GeV), when adding PU$\sim$25 to the event, corresponding to LHC running conditions in the next phase of data taking starting in 2015. Taken from [100].

The Particle Flow (PF) algorithm [101] creates a list of all stable particles in an event: photons, electrons, muons, neutral hadrons and charged hadrons. Particle momentum, direction and type are determined using all of the subdetectors of CMS, which, with its silicon tracker, highly granular ECAL and strong magnetic field is ideally suited to the task. The reconstruction of the fundamental constituents of a typical jet – largely photons, charged hadrons and neutral hadrons – uses charged particle tracks and calorimeter clusters, termed “elements”. A traversing particle is expected to give rise to one, or several elements arising from separate subdetectors. To reconstruct a particle, these elements are therefore grouped into “blocks”: links of one, two or three elements that have arisen due to the same object. Blocks can then be interpreted as individual particles, and the resulting list of reconstructed particle flow particles gives a global description of each event. This list of particles is used as the input to the anti-k_T algorithm, producing PF anti-k_T jets.

The energy of a typical jet consists of energy from charged particles (65%), photons (25%) and neutral hadrons (10%). Therefore, typically, 90% of the jet energy can be reconstructed with good precision, utilising measurements from the high resolution silicon tracker and ECAL. Only 10% of the energy, arising from neutral hadrons, is reconstructed using the relatively poor resolution hadron calorimeter. Therefore, PF jets, made of reconstructed particles, are much closer to jets made of simulated, Monte Carlo (MC) generated particles than those that rely just on calorimeter information alone (such as Calo jets), see Figure 3.13. PF jets consequently have excellent position and energy resolution. Jet momentum resolution, defined as the ratio $(p_T{}^{\mathrm{rec}} - p_T{}^{\mathrm{gen}})/p_T{}^{\mathrm{gen}}$, (where "rec" is for reconstructed, i.e. PF or Calo jets, and "gen" is for jets taken from simulation) is shown in Figure 3.14. It is because of the excellent performance of the PF algorithm, as input to the anti-k$_T$ that it is used most commonly across CMS analyses, including in the analysis presented in this thesis.

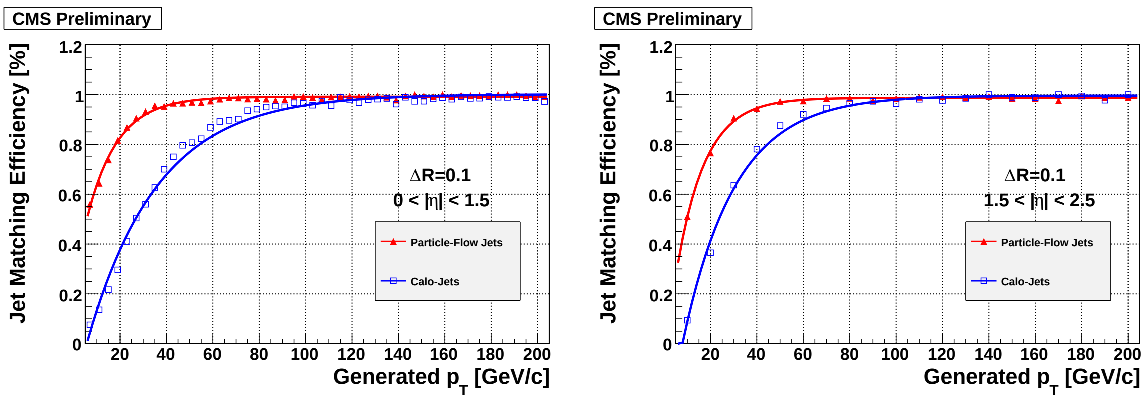

Figure 3.13: The efficiency of PF jets, and Calo jets, matched to generated jets in the barrel region (left) and the endcap (right), taken from [101]. The superior performance of PF jets is evident because they are more efficiently matched to the generator, "truth" jets, at a lower p_T threshold: termed a sharper turn-on.

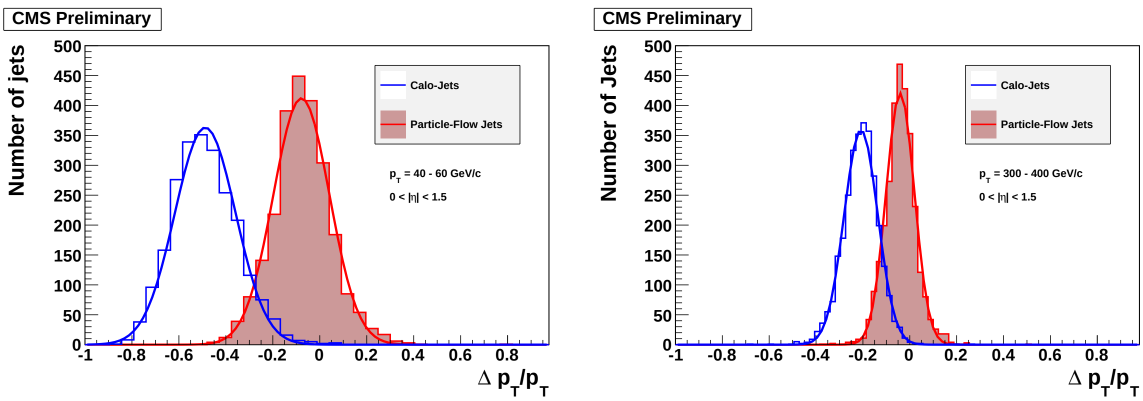

Figure 3.14: The momentum resolution, $(p_T{}^{\mathrm{rec}} - p_T{}^{\mathrm{gen}})/p_T{}^{\mathrm{gen}}$ of PF jets, and Calo jets, for low energy jets (40 GeV $< p_T <$ 60 GeV) (left) and for high momentum jets (300 GeV $< p_T <$ 400 GeV) (right) in the barrel region, taken from [101]. Not only are the peaks sharper for PF jets, meaning a smaller (and therefore better) overall momentum resolution, but it is also peaking much closer to zero, meaning the jet measurement is much closer to the generated jet momentum.

3.3.2 Missing Transverse Energy

As discussed in the previous sections, CMS is nearly hermetic, has coverage up to $|\eta| = 5$ and excellent particle reconstruction; a very complete picture of each event is available. As such, is it very well suited to make measurements of weakly interacting particles, such as neutrinos, that do not leave any trace within any subsystem of the detector; and are only evident through an imbalance of transverse momentum. New physics processes, such as R-parity conserving SUSY, would also lead to signatures involving a large imbalance in transverse momentum as the weakly interacting LSP exits the detector. DM production would also lead to such a signature. Measurements of missing transverse energy and momentum are therefore crucial to the search for new physics at CMS, as they have been crucial in previous discoveries – for example of the W boson [102], and in searches for other processes [103, 104].

The missing transverse energy vector, $\vec{E}_{\mathrm{T}}^{\mathrm{miss}}$ is formed by adding the transverse energy vectors $\sum \vec{E}_{\mathrm{T}}$ of all the particles formed in an event. The missing transverse energy vector $\vec{E}_{\mathrm{T}}^{\mathrm{miss}} = -\sum \vec{E}_{\mathrm{T}}$, where $|\vec{E}_{\mathrm{T}}^{\mathrm{miss}}| = E_{\mathrm{T}}^{\mathrm{miss}} = |\sum \vec{E}_{\mathrm{T}}|$; i.e., it is equal in magnitude and opposite in direction to the total visible energy in the event. In an analogous way to jets (and usually using such jets), $E_{\mathrm{T}}^{\mathrm{miss}}$ can be built using various algorithms. Calorimeter (Calo) $E_{\mathrm{T}}^{\mathrm{miss}}$, in the same way as Calo jets, is built from calorimeter information alone while PF $E_{\mathrm{T}}^{\mathrm{miss}}$ is calculated from all of the transverse energies of reconstructed particles in an event. In a similar way to the jet algorithms, a better resolution is achieved using the PF algorithm over calorimeter information alone, see Figure 3.15 However, because energy measurements of particle flow objects are driven by calorimeter resolution, particularly for large E_{T} objects, the improvement is less marked. In the analysis presented in this thesis, PF $E_{\mathrm{T}}^{\mathrm{miss}}$ is used, where any muons present have been removed from the calculation. It therefore mimics Calo $E_{\mathrm{T}}^{\mathrm{miss}}$, only with an enhanced resolution.

3.3.3 Muons

Muons are reconstructed using the muon systems and the tracker, and the reconstruction algorithms use the concept of "regional reconstruction". On the basis of an input or seed from the muon systems, the software only reconstructs the part of the tracker from which the muon causing the seed could originate. This means that only a very small part (typically a few percent) of the tracker volume must be processed to reconstruct a muon;

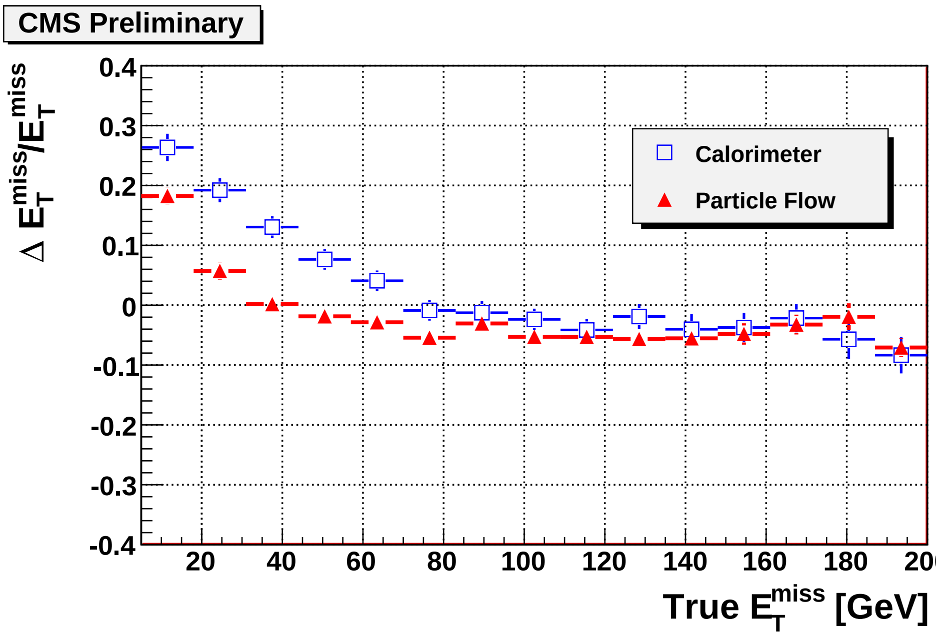

Figure 3.15: The momentum resolution, $(E_{T,rec}^{\text{miss}} - E_{T,\text{gen}}^{\text{miss}})/E_{T,\text{gen}}^{\text{miss}}$ of PF and Calo $E_{\text{T}}^{\text{miss}}$, taken from [101]. An improved resolution is seen using the PF algorithm, particularly at low values of $E_{\text{T}}^{\text{miss}}$. At higher $E_{\text{T}}^{\text{miss}}$ values, energy measurements are dominated by the calorimeter resolution and values using the two different methods converge.

thereby speeding up the procedure and reducing the CPU power necessary to process an event.

Muon reconstruction has three stages: local, standalone and global reconstruction. Starting with a seed which defines a region of interest, which could be from the Level 1 Trigger (L1) Trigger seeds (from the RPCs) or from patterns of hits found in the CSCs and/or DT, a local reconstruction is performed in surrounding compatible muon chambers. The standalone reconstruction uses information from just the muon system; measurements of track position, momentum and direction of travel are taken, and extrapolated to the nominal interaction point. Global reconstruction then extends the resulting muon trajectories to include hits in the silicon tracker. A track is extrapolated from the innermost muon chamber to the outer tracker surface, and compatible silicon layers determined. Candidates for the muon trajectory are built from pairs of hits in separate layers of the tracker and χ^2 of the fit is used to ensure a "good" muon candidate; to detect any bremsstrahlung or significant energy loss. High energy muons present particular difficulty as they suffer huge energy loss and severe electromagnetic showers in the muon system; the χ^2 probability of the fit compared to the the χ^2 probability of the tracker only trajectory allows accurate momentum reconstruction of such objects.

3.4 The Trigger

The pp interaction cross section is 100 mb , while for example, the W boson production cross section is some 6 orders of magnitude less than this, and the rare physics processes that CMS was built to search for, such as Higgs boson and SUSY production, many times smaller still; see Figure 3.16. The LHC delivers an unprecedentedly high instantaneous luminosity so that such rare physics processes occur, but this also implies that the vast majority of the collisions result in 'uninteresting' physics: namely relatively low energy, soft scattering events. It would be impossible to record the very high volumes of data that come out of CMS, some PB s^{-1}, and not useful to do so. Therefore, a very efficient method of recording those events that appear 'interesting' is necessary.

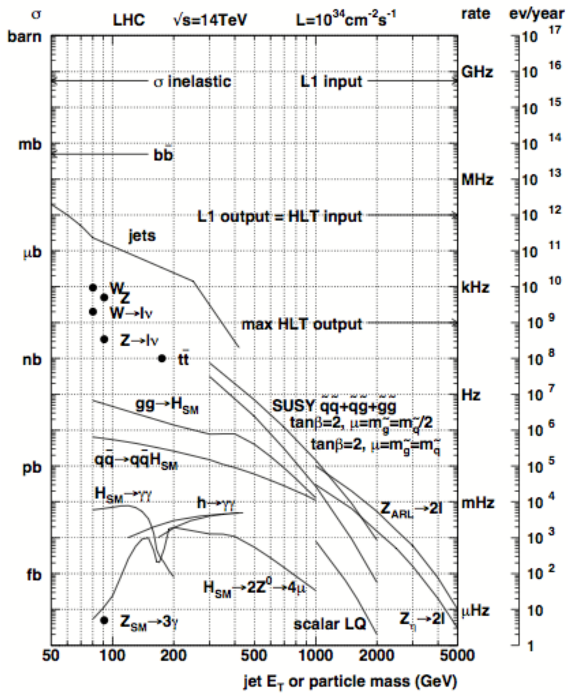

Figure 3.16: Inclusive pp cross sections (σ) for basic and rarer physics processes, showing some of the phenomena on the physics programme at CMS. Shown on the right are the interaction rates for LHC design luminosity, $10^{34}\mathrm{cm}^{-2}\mathrm{s}^{-1}$. Taken from [105].

A two tier trigger system reduces the 40 MHz LHC bunch crossing rate to an output of 100 Hz , which is then saved offline to be reconstructed ready for physics analysis. The hardware based L1 uses fast algorithms with coarse inputs from the calorimeter and muon system to efficiently select, online (that is at the same rate as LHC bunch crossings), those events that appear interesting, reducing the 40 MHz collision rate to

100 kHz. A software based Higher Level Trigger (HLT) running on the event filter PC farm at Point 5 takes the output of the L1 trigger and reduces it further to 100 Hz, using more sophisticated inputs and algorithms. Performance of the subdetectors and readiness to collect data, monitored by the Data Acquisition System (DAQ) system, is supervised by the trigger control system. Events passing HLT selection requirements are sent to the CERN Computing Centre where complex algorithms using all the information from the CMS detector are used to fully reconstruct the event. More information on the CMS trigger can be found in Ref. [105].

3.4.1 The L1 Trigger

Low granularity inputs from the calorimeter and muon system are used to quickly select possibly interesting events, based on predefined and programmable algorithms and criteria. Parts of the hardware are Field Programmable Gate Array (FPGA) based, allowing some flexibility in algorithms, while other parts are Application Specific Integrated Circuit (ASIC) based, with predefined criteria. Events are selected if they show signs of interesting physics; for example have jets, electrons/photons, or muons. Global quantities such as total transverse energy and total missing transverse energy are also used. In order to see if an event contains any of these physics objects above a pre-defined energy threshold or multiplicity, the L1 trigger is separated into the Calorimeter Trigger, which looks for jets, photons and electrons, and the Muon Trigger, which looks for muons. Global quantities are computed at the Global Trigger (GT) and combined with information from the Calorimeter and Muon triggers, and here a decision is made to keep or reject an event.

In the Calorimeter Trigger, information from the ECAL, HCAL and HF are combined. First, the calorimeter is split into different (geographical) regions, and electron, photon and jet finding algorithms run on the separate parts of the subdetectors at the Regional Calorimeter Trigger (RCT). Information from the different regions is then combined at the Global Calorimeter Trigger (GCT).In the Muon Trigger, information from the DT, CSCs and RPCs are combined. Muon track finding algorithms are applied to data from the DT and CSCs at the Regional Muon Trigger (RMT), and the Global Muon Trigger (GMT) combines information from all of the three subdetectors to get an enhanced resolution. Inputs from the GCT and GMT are then combined at the GT, where the decision to keep or discard an event is made. The architecture of the L1 trigger is shown in Figure 3.17.

There is an inbuilt latency of 3.2 μs in the L1 trigger, meaning that on the first bunch crossing, it takes up to 3.2 μs to transmit the necessary information, and make a decision. This is driven by the data storage available for information from the tracker and preshower detectors; they need so much data storage that it must be saved before a L1 accept decision, and subsequent event read out, can be made. The decisions on the rest of the bunch crossings follow at the rate of collisions, and the architecture is ready to accept another event every 25 ns.

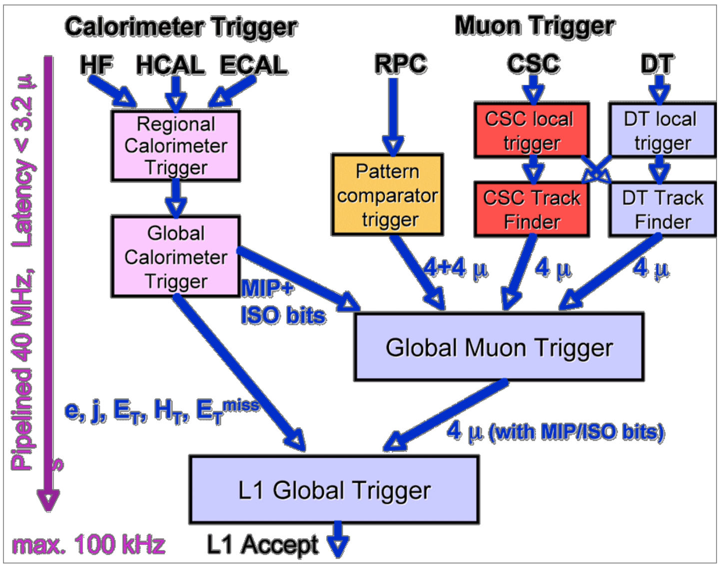

Figure 3.17: Architecture of the L1 trigger. The calorimeter trigger takes inputs from the ECAL, HCAL and HF. The muon trigger takes inputs from the DT, CSCs and RPCs. A decision is made at the L1 GT, using inputs from the GCT and the GMT, of whether to pass an event onto the HLT or discard it.

A L1 accept decision is based upon the results of the various physics object reconstruction algorithms. Typically, every physics analysis has a type of event it is searching for; a particular topology. For example, the monojet analysis looks for events with a final state of one high p_{T} jet and large missing transverse energy. At L1, it requires the global variable of an event, total missing transverse energy, above 36, 40 or 50 in L1 units of energy. A L1 trigger menu, comprised of all of the required L1 seeds for the whole physics programme at CMS, gives a certain bandwidth to each of the seeds. A low threshold seed will typically demand a large amount of bandwidth as more events are likely to be lower in energy, whereas a high threshold will require a lower bandwidth. Combined, the output to the HLT of all of the L1 seeds in the trigger menu must not exceed the design rate of 100 kHz.

3.4.2 The High Level Trigger

When an event is accepted by the L1 trigger, the full detector information for that event (consisting of around 1 MB of data) is passed onto the HLT. On the event filter farm, which consists of over 1000 PC's, all of the detector information for each event is processed. Information not available at L1 becomes available. The additional computing power and longer time scales mean the full granularity of the calorimeter and tracker information (as well as L1 objects), can be used as inputs to more complex algorithms. As a result, much more stringent requirements are used to select events of interest, creating datasets which are used for offline analysis.

An analysis will typically use more than one HLT trigger, and similarly more than one analysis might use the same trigger (and an event pass more than one trigger). For example, the monojet analysis uses a combination of three triggers which demand large missing transverse energy in every event, or a single high momentum jet in addition to large missing transverse energy. This allows events with a monojet topology to be selected efficiently; further kinematic and topological selections are applied offline to a dataset formed of events passing these trigger requirements. Similarly, every physics analysis uses a trigger (or triggers) suited to the topology under investigation.

In the same way that there is a L1 trigger menu, there is also a HLT menu comprised of all of the HLT trigger paths, and the bandwidths they require, which meets the needs of all of the physics analyses at CMS. The total bandwidth of the HLT menu must not exceed 100 Hz or 100 events saved offline per second, limited by the resources necessary to process and store events; namely Computer Processing Unit (CPU)s and disk space available.

Chapter 4

Jet Algorithms for the L1 Trigger Upgrade

In the hadron rich environment of the LHC, the hadronisation of quarks and gluons into jets is a major component of the physics programme of CMS. Whether for standard model analyses, Higgs searches, SUSY searches or exotic analyses, jet reconstruction is vital for both event selection and offline analysis, for a wide range of jet kinematic requirements. Efficient and reliable triggering on jets is therefore of key importance and the first stage of event selection, the L1 trigger, must have an effective jet algorithm. This is of particular significance as we look towards the LHC upgrade, when running conditions become increasingly challenging. Up to double the instantaneous luminosity and centre-of-mass energy lead to an increase of PU up to ~ 70 and far higher detector occupancies. Jet algorithms must maintain a similar performance in this next phase of LHC running as exhibited in the previous period of data collection. A new L1 jet algorithm is proposed, which exploits the full granularity of the calorimeter and uses event-by-event PU subtraction.

4.1 The LHC Upgrade

Following the tremendously successful operation during Run I in 2010-2012, where the CMS and ATLAS experiments collected around 5 fb^{-1} at 7 TeV and 20 fb^{-1} at 8 TeV , the LHC is currently in a period of shut-down, termed “Long Shutdown 1” (LS1). Magnet interconnections are being replaced and the dipole magnets are undergoing a quench training programme. These improvements to the LHC magnets will allow safe acceleration of protons up to 7 TeV in each beam, and sustained operation at $\sqrt{s} = 13$ TeV , eventually to achieve the design energy of 14 TeV . This will nearly double the available centre-of-mass energy as compared to Run I, potentially making Run II a discovery run – opening up more phase space and therefore opportunities for finding new physics. Instantaneous luminosity will also increase, with the aim of providing the number of events to give the statistical precision required to search for the rarest processes, as well as shed more light on the properties of the boson discovered during Run 1 [8, 9, 106]. After a period of a year or so of running after LS1 termed "Run II", the LHC will again undergo a period of shutdown, "Long Shutdown 2" (LS2), in which improvements to the accelerator injector chain will be made – with the aim of providing much greater instantaneous luminosities. The potential luminosity performance of two scenarios for future running of the LHC is shown in Table 7.1.

Scenario	# bunches	$\mathcal{L}$ (cm^{-2}s^{-1})	Pile-up	L (fb^{-1} /year)
25 ns	2760	9.2×10^{33}	21	24
50 ns	1260	2.2×10^{34}	40-76	45

Table 4.1: Two of the possible luminosity performances for LHC running during Run II, taken from [107].

If the machine operates at 50 ns , the instantaneous luminosity will double compared to that of Run I, with PU expected to more than double from around 20 inelastic collisions per bunch crossing to in excess of 70. Not only will the number of interactions per second increase due to the higher instantaneous luminosity, but the increased centre-of-mass energy means the energy of these interactions will also increase. Consequently, for a particular trigger (say, for example a single jet trigger), many, many more events will pass a particular energy threshold as compared to Run I. As a result, the trigger rate will soar.

For a single jet trigger, where the jet (reconstructed offline) is required to be above 128 GeV , 95% of jets which have been matched to this offline jet and reconstructed using the existing L1 jet algorithm are above 150 GeV – where the higher L1 threshold is due to poorer L1 reconstruction than offline reconstruction. In a typical run during 2012 (PU=15, $\mathcal{L} = 0.4 \times 10^{34}$ cm^{-2}s^{-1}), a L1 jet threshold of 150 GeV corresponds to a rate of 1.1 kHz . In the high PU test runs during 2012 that had a few bunches filled which could then be scaled up to high luminosity and PU, this trigger rate rose to 3.6 kHz (PU=45, $\mathcal{L} = 1.1 \times 10^{34}$cm^{-2}s^{-1} equivalent); and simulation shows that in similar conditions but at 14 TeV , a trigger rate of 14 kHz is expected. The total rate of all of the L1 triggers is capped at 100 kHz by design, and a balanced trigger menu is desirable to satisfy all of the physics demands of CMS. Therefore, individual trigger rates must be kept reasonably low to ensure the total L1 trigger rate is acceptable. The only way to maintain low trigger rates in the more challenging run conditions is to increase energy thresholds. Figure 4.1 shows an illustrative L1 trigger menu for the upgraded LHC, for bunch spacings of 25 and 50 ns . Thresholds have had to be significantly raised to maintain a total rate below 100 kHz ; for example, the single jet threshold is increased to 170 GeV and 205 GeV for 50 and 25 ns bunch crossings respectively.

	Current Level-1 $L = 1.1 \times 10^{34}$ cm^{-2}s^{-1}			Current Level-1 $L = 2.2 \times 10^{34}$ cm^{-2}s^{-1}		
Trigger Algorithm	Rate [kHz]	95% Threshold [GeV]	Plateau Efficiency	Rate [kHz]	95% Threshold [GeV]	Plateau Efficiency
Single e/γ	12	46	1.0	10	67	1.0
Single iso e/γ	10	38	0.9	9.4	52	0.9
Single Mu	12	23	0.95	11	42	0.95
Single isoTau	10	65	0.3	9.2	72	0.3
iso e/γ + e/γ	10	24 15	0.9	16	26 16	0.9
Mu + Mu	6.3	18 10	0.9	7.4	20 12	0.9
Tau + Tau	7.5	36 36	0.1	8.2	36 36	0.1
iso e/γ + Mu	9.6	21 11	0.85	6.2	24 12	0.85
Mu + e/γ	3.3	18 14	0.95	5.0	20 15	0.95
Single Jet	6.4	170	1.0	5.4	205	1.0
Double Jet	4.6	140 140	1.0	5.8	170 170	1.0
Quad Jet	9.4	4@71	1.0	4.8	4@96	1.0
Single iso e/γ + Jet	7.5	32 68	0.9	8.5	38 82	0.9
Single Mu + Jet	8.6	22 43	0.95	7.5	27 54	0.95
Single iso e/γ + H_T^{miss}	10	29 110	0.9	8.2	38 120	0.9
Single Mu + H_T^{miss}	4.6	18 89	0.95	9.8	20 93	0.95
H_T	3.9	500	1.0	5.4	580	1.0
Total Rate	94			92		

Figure 4.1: The projected L1 trigger menu using the current L1 system and algorithms, at 14 TeV , for illustration purposes. In the left hand column, all of the different triggers contributing to the menu are shown. In the centre (right-hand) columns, the projected L1 trigger rate, 95% threshold and plateau efficiency are shown for running conditions with bunch spacing of 50 ns , $\mathcal{L} = 1.1 \times 10^{34}$ cm^{-2}s^{-1}, PU=50 (25 ns, $\mathcal{L} = 2.2 \times 10^{34}$ cm^{-2}s^{-1}, PU=50), taken from [107].

For the physics requirements of CMS the necessary increase in L1 thresholds, and corresponding increase in offline (analysis) thresholds, is an unacceptable compromise as lower energy final states are crucial to many analyses and keeping as much physics, at as low thresholds as possible, is desirable. To cope with the challenges of the LHC upgrades, and to enable new algorithms (with better performance) to be developed so the physics performance of Run I can be maintained, or bettered, the CMS L1 trigger is also undergoing upgrades.

4.2 CMS Trigger Upgrade

Upgrades to the electronics of the calorimeter trigger, muon trigger and global trigger are under way in order to meet the triggering demands of CMS. These upgrades involve installing additional interconnections between the systems, reducing the current huge diversity of electronics cards to a small number of multi-purpose and adaptable cards, using high bandwidth optical links and modern, high powered FPGA processing chips. These upgrades not only allow more information from the detector subsystems to be used as inputs to improved (more sophisticated) algorithms, due to increased logic resources and fast links, but crucially also allow far more flexibility in the L1 trigger system. In Run I, the ability to adapt the trigger algorithms and menu to evolving LHC run conditions proved vital in reducing trigger rates and improving efficiencies. Increasing the flexibility by making more of the system adaptable, and more of the cards standardised, will only improve the trigger and enhance its longevity. Having the ability to easily update software and firmware, as well as trigger architecture, in response to unforeseen circumstances – not just in the planned LHC upgrades to 2016 but far beyond – will put CMS in an excellent position for data collection.

The new L1 trigger is being installed during LS1, and will be commissioned and run concurrently with the existing trigger during Run II. The upgraded system will be available for physics in 2016.Here, I discuss in detail the calorimeter trigger upgrade, as this is what the proposed jet algorithm, detailed in this chapter, relies upon. More information on the muon trigger and global trigger upgrade can be found in [107].

4.2.1 Calorimeter Trigger Upgrade

The calorimeter trigger uses information from the ECAL and HCAL to look for electrons/photons and jets, as described in the previous chapter. It currently is based upon a traditional trigger design; where the detector is spatially segmented into different processing nodes, each of which deals with the data from each geographical region, and does so at every bunch crossing. The desire for far more flexibility in triggering motivates a new approach to the upgrade trigger architecture, known as time-multiplexing. Instead of splitting the detector into geographical regions and sending the data to different processors at every bunch crossing, a Time-Multiplexed Trigger (TMT) places all of the data from the detector in a single processor across several bunch crossings. No data is thrown away at any stage of the process, and all of the data, at its full granularity, is available in the same card making many more algorithms possible.

Traditional Trigger Architecture

A conventional trigger architecture is shown in Figure 4.2. The calorimeter is split into geographical regions in $\eta - \phi$, and at every bunch crossing data from the individual regions are sent to different processors. Boundaries between these regions must be duplicated in each implicated processor, to ensure that any objects found along the boundary are sufficiently dealt with. To achieve a compact implementation, at each stage of the trigger process the volume of data is reduced and the minimal information with which to make a decision is passed onto the GT. Therefore, a lot of the information from an event is discarded before a decision at the GT is made. In addition, the current calorimeter trigger does not use the full granularity of information available, and the combined ASIC and FPGA hardware, although permitting some flexibility in algorithms and parameters, is restricted by a fixed data flow. Not all algorithms can therefore be implemented, and the coarse inputs limit the possible performance.

Energy clusters are built into physics objects with which the GT can make a decision over two processing layers. Trigger towers, consisting of groups of 5×5 crystals in the ECAL, and the corresponding blocks of the HCAL, are themselves grouped into 4×4 arrays or “regions”. These regions are used as inputs to the various object algorithms. In the first layer, the ‘Regional stages’ in Figure 4.2, the regions, or clusters of transverse energy are assigned a type; electron/photon-like, if energy is predominantly in the ECAL, otherwise hadron-like. In the second processing layer, the ‘Global Stages’, the cluster type is identified as an electron/photon or tau (for high energy or isolated deposits respectively), and non-isolated clusters are grouped together to form jets. The jet finding algorithm looks for energy deposits in windows of 3×3 regions, with the requirement that the central region has a larger transverse energy deposit. The top four candidates are passed onto the global trigger, with the rest discarded. Also in this layer of processing, the value and direction of total missing transverse energy are calculated from the sum of

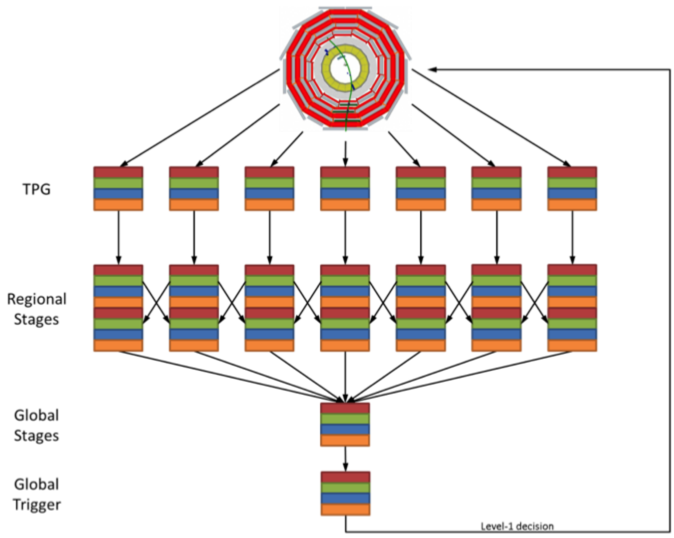

Figure 4.2: Conventional trigger architecture, showing data processing in regions. Taken from [?].

energy deposits across the calorimeter, and jet candidates above threshold are summed to give the total hadronic energy content, known as H_{T}.

Time Multiplexed Trigger

A time-multiplexed trigger architecture is shown in Figure 4.3. In a similar way as the HLT, it will consist of parallel nodes, each of which process individual events concurrently. All of the data from an event – from the whole $\eta - \phi$ range of the calorimeter and at full granularity – are sent to an individual processor. The first processor receives the data from the first bunch crossing over N clock cycles (where the length of a clock cycle is equal to the time between bunch crossings, 25 or 50 ns). The data from the second bunch crossing are sent to the second processor, again over N clock cycles, and so on; where there are more than N processors in total, as each processor needs time to process each event. After the first processor has processed all of the data from the first bunch crossing and passed it on to the next stage of the trigger, the 'Demux' in Figure 4.3 (some $N + X$ clock cycles after the first bunch crossing where X is the time taken to process and send on the data), it can then receive data from another bunch crossing. Developments in large FPGA chips and increased rate and volume of data transmission in optical fibres make this kind of architecture possible for the upgraded CMS calorimeter L1 trigger, whereas it was not when the current trigger was designed and built. The system latency, $N + X$, is now small enough, due to the increased processing power and bandwidths, that it is viable in hardware for the huge amounts of data and short time-scale that the trigger demands [108].

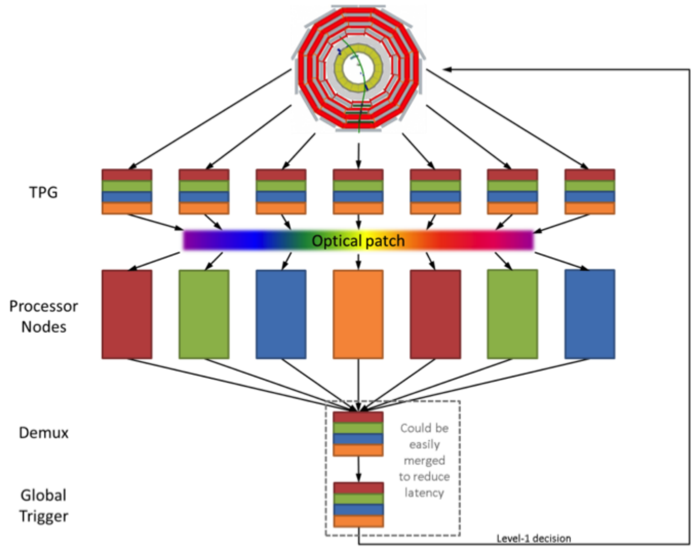

Figure 4.3: Time-multiplexed trigger architecture, showing data pipelining to different processing nodes. Taken from [**?**].

With all of the data, at full granularity, in one single processor, many more algorithms for object reconstruction are possible. Tower level calorimeter inputs (rather than region level inputs) will be available, increasing the granularity by a factor 4^2, with similarly improved spatial resolutions. There is also scope for an array of additional variables, using information from the whole calorimeter. For example, the average energy deposit for each row in $|\eta|$ or ring of ϕ can be calculated, and used to give an estimate of PU on an event-by-event basis. In the remainder of this chapter, a jet algorithm is proposed for the upgraded L1 calorimeter trigger. More detail on the CMS L1 calorimeter trigger upgrade can be found in Ref. [109].

4.3 Algorithm for jet reconstruction at L1

A jet algorithm to reconstruct, filter and calibrate L1 jets is proposed, for the upgraded CMS calorimeter trigger. It is assumed that all of the L1 calorimetric information for a single event streams through a single processor; that is, all of the information from a single bunch crossing can be processed in one single chip. This is compatible with the TMT architecture which will be available after LS2 at CMS.

Using tower level information, the algorithm creates a tunable sized jet at each site on the calorimeter, filters out zero-energy jets and repeats, to get the 'best' 13 jet candidates per event. The average jet energy density for each event is calculated, and subtracted from the energy deposited across the calorimeter in order to perform PU subtraction on an event-by-event basis. The 13 jet candidates are then calibrated to offline energy. This algorithm is compared to the current L1 jet algorithm.A much improved spatial resolution is seen, as well as enhanced, and crucially, more PU independent energy resolution. The resulting trigger turn-on curves for various jet energy thresholds, and trigger rates for single and multijet triggers are improved compared to the current algorithm, as well as the global variable H_{T} . This jet algorithm was the proposed jet algorithm in the CMS L1 Trigger Upgrade Technical Design Review, Ref. [107].

4.3.1 Jet Reconstruction

The proposed jet algorithm uses the full granularity of the calorimeters available at L1; that is, 5×5 ECAL crystals grouped together into towers, with the corresponding block of HCAL. In the centre of CMS, each tower measures 0.087×0.087 in the $\eta - \phi$ plane, with the η dimension increasing as η increases; see Figure 4.4. In total there are 72 towers in the ϕ direction, and for $|\eta| \leq 3.0$ (the barrel region), 56 towers in the η direction. The sum of energy deposits in both the ECAL and HCAL at each tower is used as input to the algorithm.

A group of $n \times n$ towers is combined to form a jet candidate, where the energy of that jet candidate is the sum of the $n \times n$ towers it consists of. The jet size, n, is completely flexible, as well as the jet shape. Jet sizes of 8×8 to 12×12 were studied, and both circular and square jets. This compares with the current L1 jet algorithm, which consists of equivalent 12×12 square jets - where the towers are incorporated into regions, each measuring 4×4 towers; see Figure 4.5 for a comparison of the current and proposed upgrade jet geometry. For circular jets the size n represents the length of the diameter, for square jets it represents the length of the side.

A candidate is created at each individual tower, using a "sliding window" approach. Only jet candidates with non-zero energies are passed onto the next stage, however there remains a huge jet multiplicity at this first stage of jet creation. There is a jet for every non-zero tower, and a huge number of overlapping jets as each tower contributes to n^2 different jets, or, equivalently, each jet candidate has $(2n-1)^2$ overlapping jets. Figure 4.6 shows some of jet candidates which overlap, shown in red, with a single jet

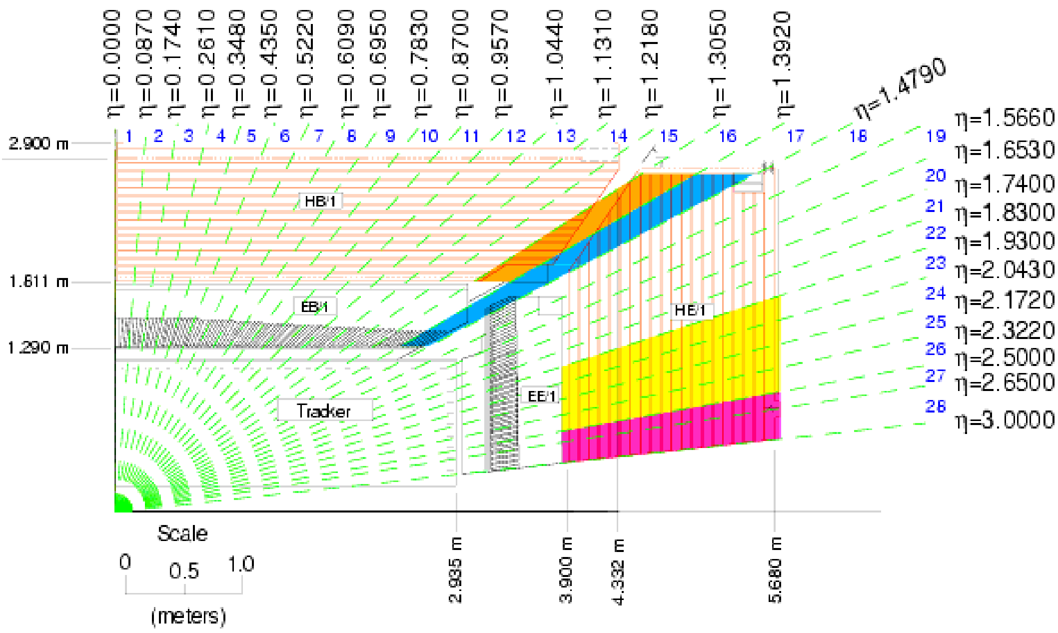

Figure 4.4: Layout of trigger towers in the $r - z$ projection, for $0 < \eta < 3.0$. Both ECAL and HCAL towers are shown.

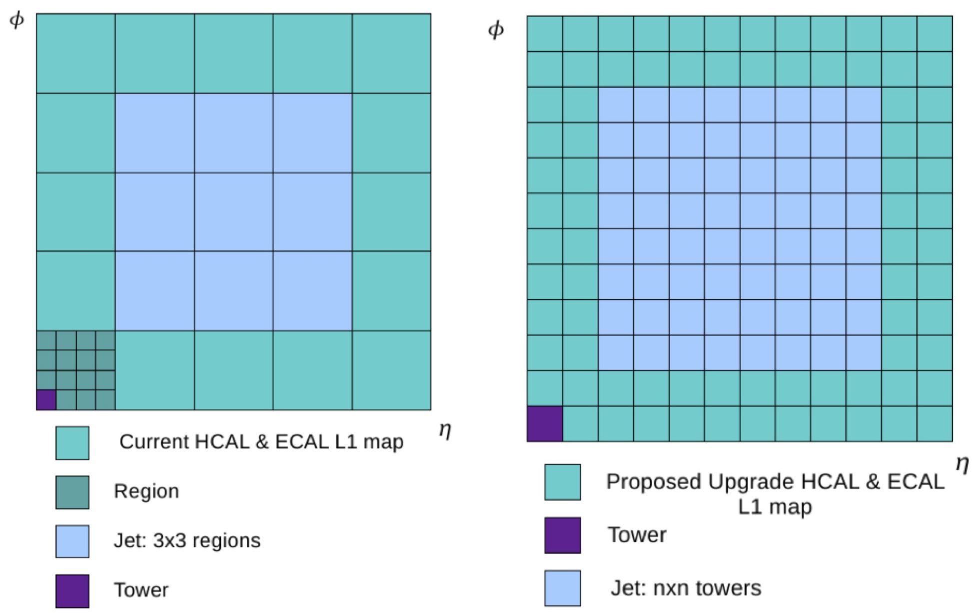

Figure 4.5: Comparison of the current L1 jet map, left, with the proposed upgrade jet map, showing a 8×8 square jet, right.

candidate measuring 4×4 towers and square in shape, shown in purple. The window of all overlapping candidates is shown in blue; and measures 10×10 towers. The resulting numerous overlapping jets must be sorted and filtered to find the highest energy jet of the candidates.

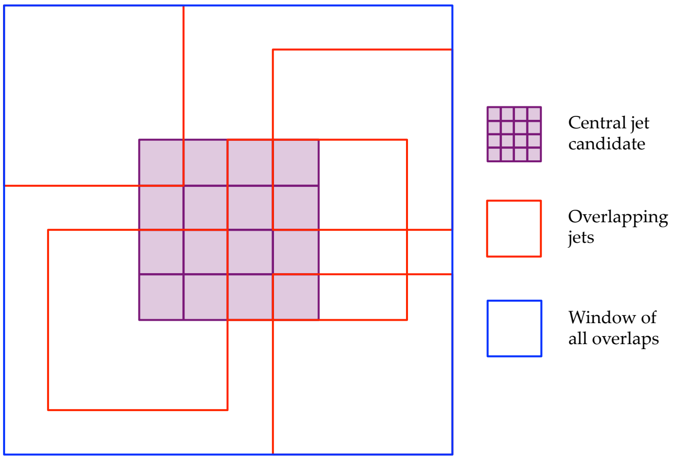

Figure 4.6: A few of the overlapping jets of one 4×4 jet (centre, purple), are shown in red. The window of all of the jet overlaps is shown in blue, measuring 10×10. These overlapping jets must be sorted and filtered to keep only the most energetic jet.

To give the best angular resolution, the η and ϕ coordinates of the jets are energy weighted,

$$\eta_{jet} = \frac{\sum \eta_{\text{tower}} \cdot E_{\text{tower}}}{\sum E_{\text{tower}}} \tag{4.1}$$

$$\phi_{jet} = \frac{\sum \phi_{\text{tower}} \cdot E_{\text{tower}}}{\sum E_{\text{tower}}}. \tag{4.2}$$

Here, the sum is over all of the towers in a jet window and $\eta_{\text{tower}}, \phi_{\text{tower}}$ are the coordinates of the individual towers within a jet, E_{tower} is the transverse energy deposit in the tower and η_{jet}, ϕ_{jet} are the coordinates of the jet.

In previous studies diameter 8 circular jets gave the best angular resolution, so these are presented here. Remake plots and include here

4.3.2 Jet Filtering

The jet collection must be sorted and filtered to remove the numerous overlaps. Firstly, all jets in each event are ordered in energy using a bitonic sort. This is a recursive parallel sorting algorithm suitable for implementation in hardware. It takes 2^N inputs and sorts in N steps using a series of bitonic sequences and splits.

However, there is often more than one overlapping jet of a particular energy. An asymmetry parameter in η and ϕ is also considered for each jet when this is the case:

$$\begin{aligned} A_{\eta,\phi} = &\sum (\text{Constituent tower energies in positive } \eta, \phi) \\ &- \sum (\text{Constituent tower energies in negative } \eta, \phi) \end{aligned} \tag{4.3}$$

A jet with all of its energy in the central tower will have $A_{\eta,\phi} = 0$ whereas a jet of the same energy with all energy deposits in an outer tower will have large $|A_{\eta,\phi}|$. If overlapping jets have the same energy, they are instead sorted to give the lowest asymmetry parameter. The first element in the sorted list is then the most energetic jet, with its energy concentrated most centrally within the $n \times n$ window.

The sorted list is then filtered to remove jets which overlap with with this first jet. The process is repeated until 13 separate jets are found. This number is somewhat arbitrary, and is limited by hardware at some high number.

Jets are sorted initially in one dimension, along η or ϕ, and overlaps in one dimension are removed. The resulting list of the most energetic jets along or around the calorimeter is then sorted in the other direction to give the final jet collection.

4.3.3 Event-by-event estimation of pile-up

The measurement of the PU contribution to the jet energy is evaluated event by event using a method inspired by the paper of Cacciari and Salam [110] and already used to correct offline jets. In a pp collision with a large number of overlapping proton-proton interactions, a large number of relatively soft jets originate from PU and are distributed roughly evenly across the calorimeter. The median jet transverse energy is therefore very likely to come from PU, and gives a good estimate of the typical transverse energy of a PU jet in the event. Further, the energy density of the median jet transverse energy gives a good estimation of the energy density due to PU across the calorimeter. The energy released by PU per unit area in each event, denoted by ρ, can therefore be estimated using the median jet transverse energy, and the area of the jet:

$$\rho^{\mathrm{L1}} = \frac{\langle E_{\mathrm{T}}^{\mathrm{L1\ jet}} \rangle}{A_{\mathrm{L1\ jet}}} \tag{4.4}$$

where $\langle E_{\mathrm{T}}^{\mathrm{L1\ jet}} \rangle$ denotes the median jet transverse energy, and $A_{\mathrm{L1\ jet}}$ denotes the jet area. The energy of all jets in an event can then be corrected for the energy density due to PU by simply subtracting from all jets in an event using

$$\text{PU corrected } E_T \quad = \quad E_T - \rho^{\,\mathrm{L1}} \times A_{\mathrm{L1\ jet}}, \tag{4.5}$$

because the energy density due to PU across the calorimeter is assumed to be uniform. This assumption is valid for PU values of order ~ 50, however as PU increases above 100 pp collisions in each bunch crossing, simulation shows many more soft PU jets are expected to lie in the forward regions of the detector, so an η dependent PU subtraction may be more suitable for very high PU scenarios. This is not investigated here, but is within the capabilities of the upgraded trigger system.

In the following we show the effect of PU subtraction in the measurement of the jet energy. The same quantity could also be used to correct contribution of PU to quantities used to defined electrons/photons; isolation parameters, and the ratio of transverse energy deposits in the HCAL and ECAL.

4.3.4 Calibration to the jet energy scale

The raw jet energies from the calorimeter towers must be corrected to the jet energy scale. Different regions of the calorimeter give different responses so a set of calibration constants in p_{T} and η are derived. A non linear regression method is used on an independent subsection of 20,000 events collected using single muon trigger; that is, events which contain a least one muon, which often implies hadronic activity in the opposite hemisphere to the muon and so the data sample provides a sufficient number of jets to do a statistically meaningful calibration.

Once the L1 upgrade jets have been created, sorted and filtered, the value of the average energy density due to PU, $\rho^{\,\mathrm{L1}}$, is calibrated to the jet energy scale by comparing it with ρ calculated offline for each event. The corrected PU subtraction parameter is applied to the L1 jets in the event according to Equation 4.5, in order that they can be calibrated to the offline jets which have been similarly PU subtracted. The leading offline jet in each event, where the jet is formed using the anti-$\mathrm{k_T}$ algorithm with radius parameter of 0.5 and inputs from the calorimeter alone, "AK5 Calo jets", is matched to a L1 jet within a cone of $\Delta R = \sqrt{(\eta_{\,L1} - \eta_{\,offline})^2 + (\phi_{\,L1} - \phi_{\,offline})^2} < 0.5$. The use of AK5 Calo jets gives reconstructed offline jets as close as possible to those created at L1, as both are built using calorimeter information alone. The values of p_{T} and η for the matched L1 and offline jets are used as inputs to a multi-variant analysis. This

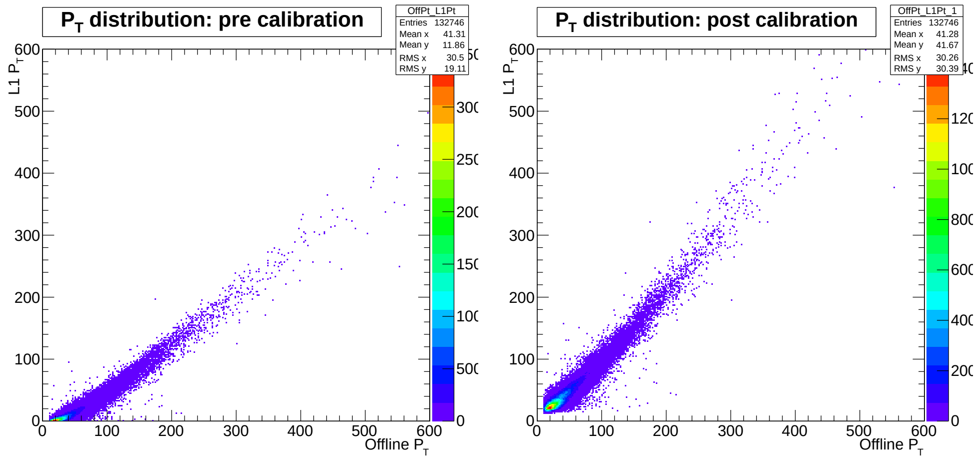

Figure 4.7: The p_{T} distribution of L1 jets that have been matched, within a cone of $\Delta R < 0.5$, to offline jets reconstructed with the anti-k$_{\mathrm{T}}$ algorithm using a radius parameter of 0.5 and calorimeter information as input only. The distribution shown before a p_{T} and η calibration has been applied is shown on the left, and after the calibration has been applied on the right. In both distributions, PU has been subtracted from both jet collections.

provides a lookup table of multiplication factors binned in values of the L1 jet η and p_{T}. Applying this calibration to the L1 jets gives a calibration independent of PU.

The distribution of L1 jet p_{T}, where each jet has been matched to an offline jet, before and after the calibration has been applied is shown in Figure 4.7. Momenta are much more closely matched after the calibration has been applied.

4.4 Upgrade L1 Jet Algorithm Performance

Jet performance can be characterised by angular and energy resolutions, efficiency of reconstruction and trigger rates. The proposed upgrade L1 jets were simulated using data that was collected in high PU conditions during 2012, where events were selected at random from the whole dataset, for example every 10$^{\mathrm{th}}$ event kept – termed "Zero Bias" data. The LHC run used for the study had an average of 45 primary vertices per bunch crossing.

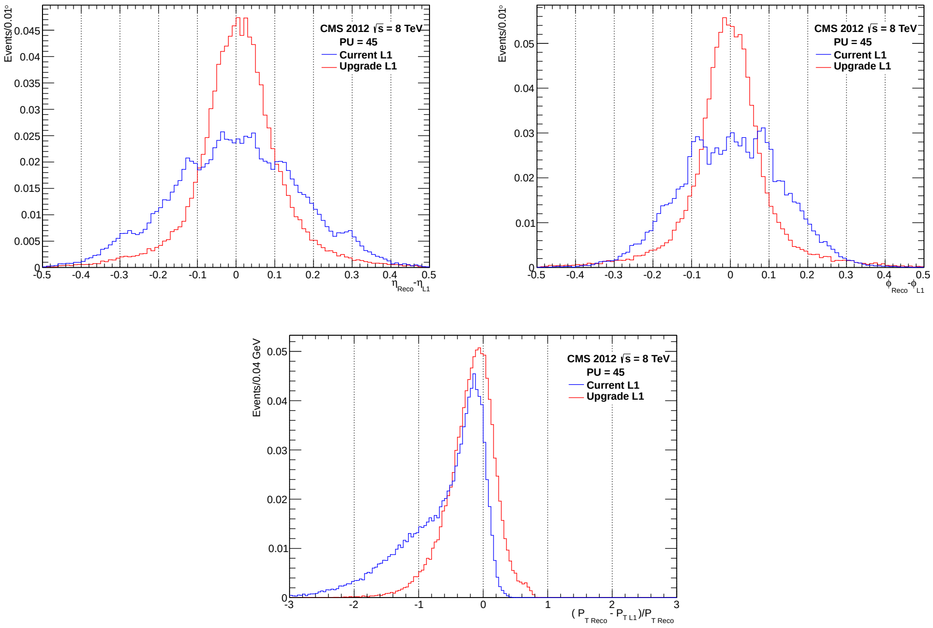

Figure 4.8: Resolution of η , ϕ and p_{T} for high PU data taken by the CMS detector in 2012. There is a clear improvement with the upgrade jets, plotted in blue, in both angular resolutions and energy resolution.

4.4.1 Angular and Energy Resolutions

Resolutions are measured as compared to offline AK5 Calo jets, as described in Section 4.3.4. The leading offline jet (which must have $p_{\mathrm{T}} > 20$ GeV) is matched to a L1 jet within $\Delta R < 0.5$, and the resolutions are defined as:

$$\sigma_{\eta} = \eta_{offline} - \eta_{L1} \tag{4.6}$$

$$\sigma_{\phi} = \phi_{offline} - \phi_{L1} \tag{4.7}$$

$$\sigma_{p_{\mathrm{T}}} = \frac{{p_{\mathrm{T}}}^{L1} - {p_{\mathrm{T}}}^{offline}}{{p_{\mathrm{T}}}^{offline}} \tag{4.8}$$

Angular and energy resolutions of the proposed upgrade algorithm compared to the current system are shown in Figure 4.8. There is a much improved angular resolution as the upgrade jets take advantage of the full granularity of the calorimeter. In high PU data, the energy resolution is improved due to the PU subtraction. With the current L1 jet algorithm, there are a significant number events in which the leading offline jet has been matched to low energy PU L1 jets, giving a negative value of $\sigma_{p_{\mathrm{T}}}$ and giving rise to the significant negative tail in the distribution.

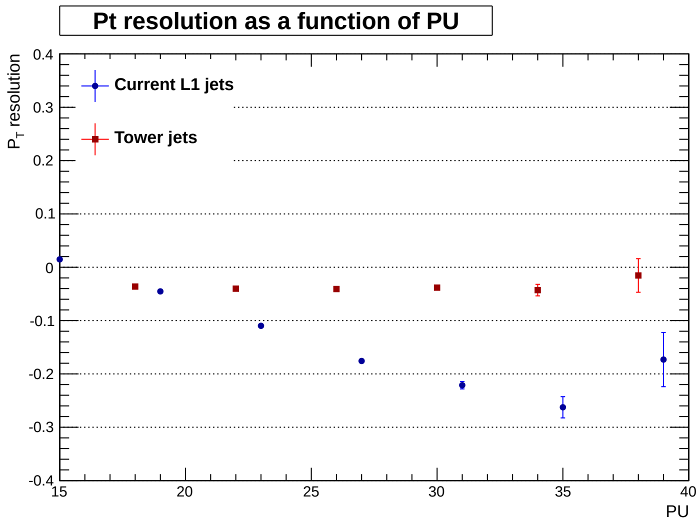

Figure 4.9: The PU dependency of the L1 jet energy resolution for both the current algorithm and the upgrade algorithm, where the resolution is taken as the RMS of the PU distribution shown in Figure 4.8, for different PU bins. There is a clear improvement with the upgrade jets, plotted in blue, which shows independence of PU up to PU $\sim$ 40.

Crucially, the energy resolution of the upgrade jet algorithm shows a much reduced dependence on PU, shown in Figure 4.9. This is evidence that the event-by-event PU subtraction has the intended effect, reducing the worsening effect of additional primary vertices on the jet energy resolution, and the upgrade jet algorithm is therefore is expected to show a reduction in rates as compared to the current algorithm.

4.4.2 Trigger efficiencies

The trigger efficiencies for various L1 jet transverse energy thresholds are measured, as compared to AK5 Calo jets, to show the effectiveness of the proposed algorithm at reconstructing jets which have been measured offline, which are treated as the "truth". If the leading L1 jet in each event above a certain energy threshold is matched to an offline jet, the energy of the matched offline jet is plotted. All matched offline jet energies are also plotted. By taking the ratio between these two distributions we attain trigger turn on curves, shown in Figures 4.10 and 4.11.

The sharpness of the turn on curve is due to the energy resolution of the jet algorithm. If all of the L1 jets have reconstructed energies that exactly equal the energies of the offline jets to which they are matched, i.e. $\sigma_{p_T} = 0$, there would be a step function at

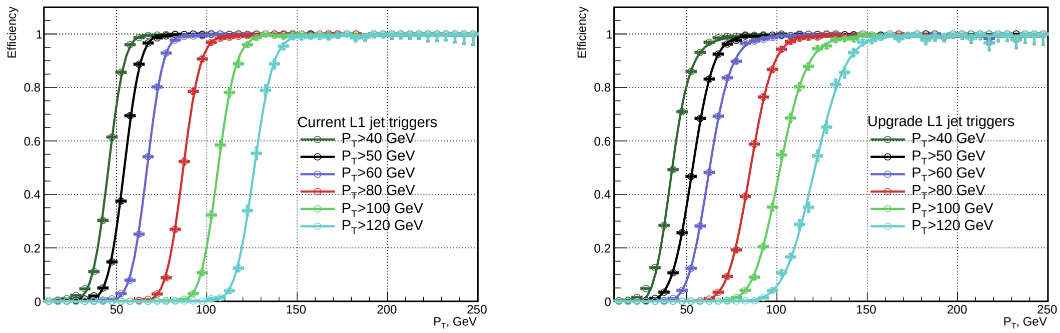

Figure 4.10: On the left are the trigger turn on curves for the current jet algorithm and on the right are the trigger turn on curves for the upgrade jet algorithm, for various single jet trigger thresholds, and were calculated using relatively low PU data.

the value of the jet energy threshold of the trigger. The turn on would be instant at the specified trigger threshold. The plateau efficiency of the turn on is dictated by the matching efficiency of the jet algorithm. If all L1 jets are perfectly matched to offline jets then the algorithm is fully efficient at reconstructing jets at L1 and the plateau efficiency is 1.

The turn on curves shown in Figure 4.10 are taken from data taken using the same single muon trigger as was used for jet calibration, where the presence of at least one muon in each event implies there is often hadronic activity in the opposite hemisphere of the detector to the muon. This is a relatively low PU set of events, with approximately 20 p-p interactions per bunch crossing. Figure 4.11 shows the performance at PU of approximately 45, a data sample which has lower statistical precision, hence the larger error bars. The sizeable negative tail shown in the momentum resolution for the current algorithm in Figure 4.8 is evident in the bump at low momentum in the left hand plot. Events in which relatively soft jets due to PU have been reconstructed above threshold at L1 are matched to very soft PU jets reconstructed offline and cause the behaviour at low p_T . Because the soft PU jets have effectively been removed from the upgrade L1 jet collection, this is not the case for the upgrade trigger turn ons.

The PU subtraction of the proposed upgrade algorithm is also evident in the upward shift in energy of the turn on curves, going from the current algorithm to the upgrade algorithm. For a requirement of, for example, one 40 GeV jet at L1, the offline value at which 95% of events pass the trigger is 51.4 GeV for the current algorithm in the high PU dataset; and 62 GeV for the upgrade algorithm. Table 4.2 shows the offline transverse momentum value at which the trigger is 95% efficient for the various turn on curves

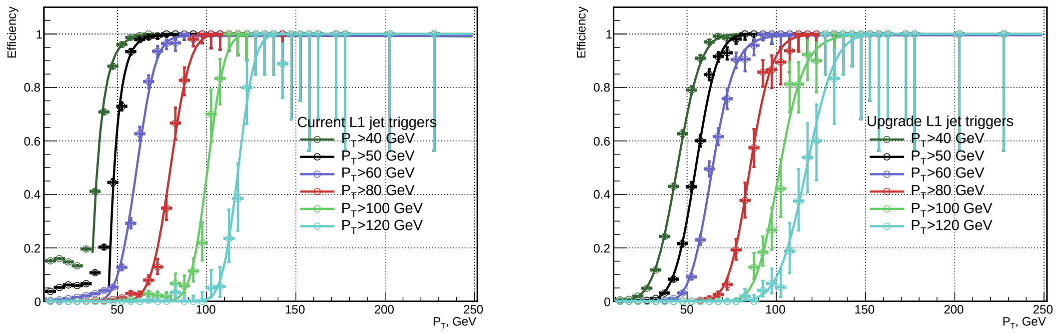

Figure 4.11: On the left are the trigger turn on curves for the current jet algorithm and on the right are the trigger turn on curves for the upgrade jet algorithm, for various single jet trigger thresholds, using relatively high PU data.

shown in Figure 4.11. A lower typical hadronic energy at L1 in events reconstructed using the upgrade algorithm, due to the PU subtraction, drives the 95% efficiency values up. Plateau efficiency values are 1 in both algorithms, meaning the upgrade jet algorithm (like the current algorithm) is fully efficient at large jet p_{T} values.

Table 4.2: The 95% efficiency values for various L1 jet transverse momentum thresholds, in GeV , and plateau efficiency values for the current and upgrade algorithm, for turn on curves taken in high PU data and shown in Figure 4.11.

	Current L1		Upgrade L1	
L1 threshold	95% efficiency	Plateau	95% efficiency	Plateau
40	51.4	1	62.0	1
50	59.5	1	70.9	1
60	75.4	1	83.7	1
80	94.1	1	103	1
100	112.9	1	123.6	1

4.4.3 Jet trigger rates

As discussed in Section 4.1, the purpose of building a new trigger is to be able to better control the trigger rates at reasonable energy thresholds in the future LHC running, which is not possible with the current system. The projected trigger rates of the proposed jet algorithm in the next phases of LHC running are therefore compared to the current system, in order to show the improvement in rates, and subsequent reduction in energy thresholds possible with the upgraded CMS L1 calorimeter trigger.

Without any requirements on events that are recorded, i.e. Zero Bias data where all events are kept, the rate is equivalent to the instantaneous luminosity multiplied by the inelastic proton-proton cross section, $R = L \times \sigma_{pp}$. In events where there are additional primary vertices in the bunch crossing, PU>1, it takes the number of interacting vertices to get the process in question to occur, so there is an inverse proportionality to the PU, $R = L \times \sigma_{pp}/PU$. The rate of events to pass a particular trigger at L1, $\mathrm{R_{L1}}$, for a given luminosity and PU scenario can then be written as

$$\mathrm{R_{L1}} = \mathrm{R_{ev}} \cdot \frac{L \times \sigma_{pp}}{\mathrm{PU}}, \tag{4.9}$$

where $\mathrm{R_{ev}}$ is the normalised trigger pass rate per event, which for a given set of events is simply the number of events passing a certain trigger divided by the total number of events. Using this equation, the L1 trigger rates can then be extrapolated to a given luminosity and PU scenario.

The rates for several jet triggers are plotted in Figure 4.12, in terms of the L1 jet energy. Usually, the offline cut used in analysis is dictated by the allowed trigger rate, which corresponds to a particular L1 threshold, and therefore to a 95% efficiency value – where the 95% efficiency value is a low as possible to maintain as much phase space as possible (given the rate restrictions). It is therefore also helpful to show the rate in terms of the 95% efficiency, which enfolds both trigger rate and efficiency of the proposed algorithm and enables a fair comparison between the current and proposed upgrade algorithm. The conversion from the online, L1 jet energy to offline 95% threshold is taken from the turn on curves shown in Figure 4.11, using the linear conversion function shown in Figure 4.13. Figure 4.14 shows the single and quad jet (where four jets are required) trigger rates vs the 95% efficiency. The current and upgrade single jet rates are comparable, as the PU subtraction does very little to the leading jet in the event, whereas the multi jet triggers, such as the quad jet trigger, see a significant reduction in rate as PU jets are removed from the event.

4.4.4 Other jet variables

Other offline variables, constructed from jets, have been widely used in the data analyses at CMS at 7 and 8 TeV , both at trigger level and offline. They therefore also will also

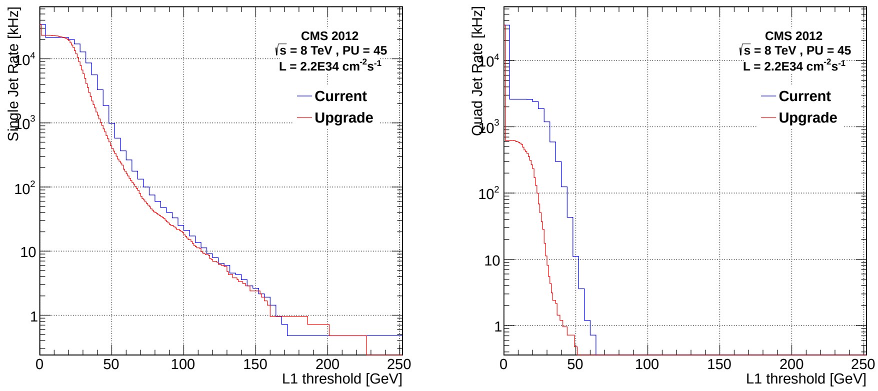

Figure 4.12: Rates of single and quad jet triggers. The single jet trigger shows similar performance to the current system, while the multi-jet trigger show a large reduction in rate

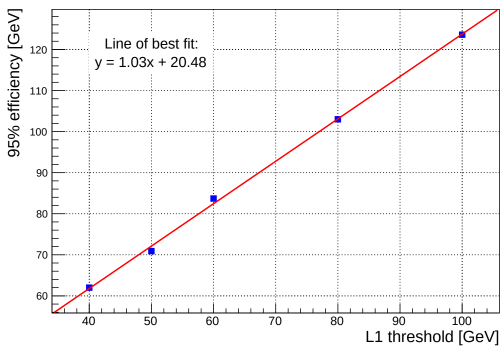

Figure 4.13: Conversion between the L1 jet threshold and the 95% efficiency as measured offline, for the proposed upgrade jet algorithm, using the turn on curves shown in Figure 4.11.

benefit from the upgraded calorimeter trigger, and shown here are the improvements in rates for H_{T}, the transverse hadronic energy which is defined as the scalar sum of jet transverse momenta in each event:

$$H_{\mathrm{T}} = \sum |p_{\mathrm{T}}{}^{\mathrm{jet}}| \tag{4.10}$$

where the sum is over all jets in each event. H_{T} is commonly used for analysis which search for SUSY, for example in Ref. [111]. It gives a good indication of the amount of hadronic energy in an event and so the energy transfer in the original inelastic p-p collision, which should be high for new physics processes to occur. It is particularly sensitive to the number of primary vertices in each bunch crossing, as soft PU jets are included in the sum. The addition of PU subtraction on an event-by-event basis in

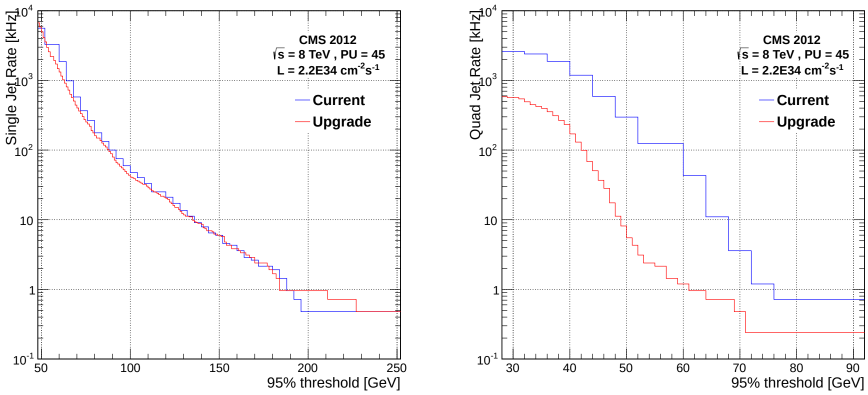

Figure 4.14: Rates of single and quad jet triggers. The single jet trigger shows similar performance to the current system, while the multi-jet trigger show a large reduction in rate

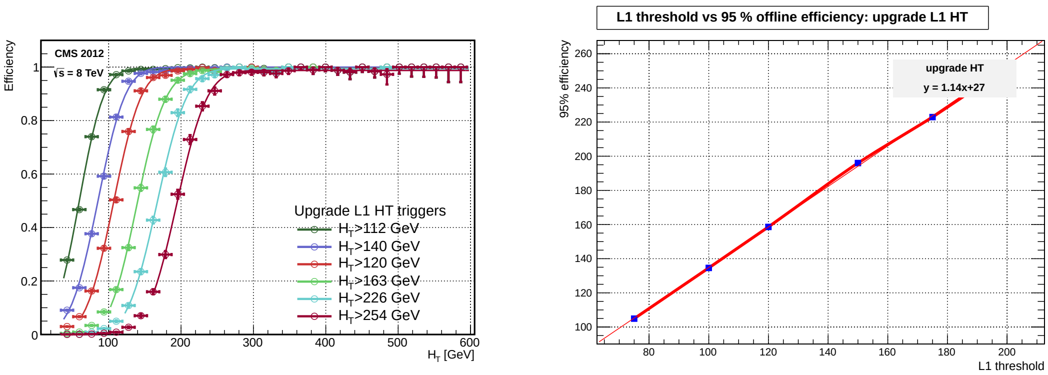

Figure 4.15: The trigger turn on curves for the H_{T} variable, left, and the conversion between the L1 H_{T} threshold and the 95% efficiency as measured offline, using H_{T} constructed with the proposed upgrade algorithm.

the proposed upgrade jet algorithm therefore has the potential to lead to significant improvements in the rate. The trigger turn on curves for various H_{T} thresholds using the upgrade jet algorithm are shown in Figure 4.15 together with the conversion between the L1 threshold and the 95% offline efficiency. The trigger rate of the H_{T} in terms of both the L1 threshold and the 95% efficiency are shown in Figure 4.16, which shows a rate reduction of nearly an order of magnitude when using the upgrade algorithm compared to the current algorithm, in terms of the 95% efficiency. This is a much fairer comparison between the two algorithms than the rate in terms of the L1 threshold, as the current H_{T} and $H_{\mathrm{T}}^{\mathrm{miss}}$ values at L1 are not corrected to the jet energy scale.

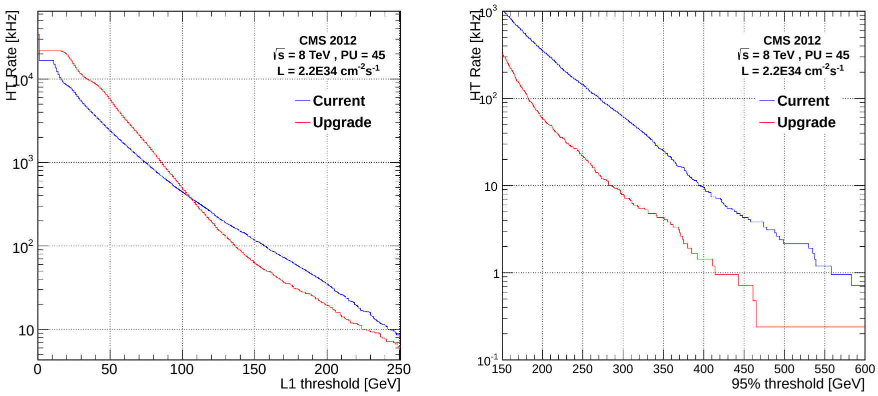

Figure 4.16: Rates of H_{T} triggers, vs L1 threshold (left) and 95% offline threshold (right), where the conversion between L1 threshold and 95% efficiency is taken from Figure 4.15. There is a significant reduction in rates with the proposed upgrade algorithm.

4.5 Conclusion

The proposed upgrade jet algorithm, which is possible to implement with the upgraded CMS calorimeter trigger based upon a TMT architecture, shows significant improvements over the current L1 jet algorithm. By utilising event-by-event PU subtraction at L1 for the first time, the dependency of PU of the L1 jet algorithm is much reduced. By taking advantage of the full tower level granularity of the calorimeter, the angular resolutions of the algorithm are also much improved. This will lead to large improvements in topological calculations at the GT, where two or more objects are used to calculate some quantity which is used in triggering; for example transverse mass, and determining jets arising from Vector Boson Fusion processes such as Higgs boson production. While similar trigger rates are seen for the single jet triggers, there are big improvements in the multijet trigger rates; and a factor of two reduction in the quad-jet trigger rate. The H_{T} variable also sees a factor 10 reduction in rate. These rate reductions will allow lower energy thresholds in the upgraded CMS L1 calorimeter trigger, as compared to the current L1 jet algorithm, and help to maintain the energy thresholds and jet rates that were used in 7 and 8 TeV data taking.

This upgrade jet algorithm was proposed in Ref. [107], and the majority work was done during 2012. Many improvements to the algorithm are possible, using different PU subtraction techniques, different jet shapes, and additional parameters such as jet substructure variables. Indeed, since this work was completed improvements have been made, and documented elsewhere [112].

Chapter 5

Searching for SUSY with compressed mass spectra using monojet events

"Physics, as we know it, will be over in six months."
— (1928) Max Born, 1882 – 1970

This chapter and the next describe a search for events containing a single energetic jet and missing transverse momentum, using a data sample collected at 8 TeV by the CMS detector at the CERN LHC and corresponding to an integrated luminosity of 19.7 fb^{-1}. In this chapter, we describe the event selection of the search as well as background estimations and the associated systematic uncertainties.

5.1 Introduction

The monojet signature of a high p_{T} jet and an imbalance of momentum in the transverse plane is the discovery signal for many new physics scenarios that have genuine missing energy in the final state. Searches for Large Extra Dimensions in the framework of the Arkani-Hamed, Dimopoulos, and Dvali (ADD) model [54], for DM using effective field theory and simplified models, and Unparticle production [113] have been presented in previous searches both at the LHC and the Tevatron [114–121] using the monojet channel. Signals are commonly invisible; for example the theorized DM is a Weakly

Interacting Massive Particle (WIMP) candidate, and as such, does not interact with any part of the detector. It therefore leaves no signal but an imbalance of momentum in the transverse plane, which is balanced by an ISR particle. In this case, the ISR particle is a quark or gluon, leading to a high p_{T} jet. Searches have also been conducted using other radiated particles: photons (termed "monophoton") and W or Z bosons ("mono-W" or "mono-Z") [115, 122–128]. However, because monojet searches have the advantage of higher production cross sections (as the strong coupling constant α_s is greater than the electromagnetic or weak coupling constants), they typically lead to stronger limits.

A search for compressed SUSY in the third generation is motivated in Chapter 2. Such signals are slightly different: Feynman diagrams are shown in Fig. 5.1. The final state does not just consist of missing transverse momentum balanced by an ISR jet; there are also sparticle decay products. These are therefore not pure monojet signals. However, when the mass difference between the parent sparticle and the LSP decreases below 80 GeV, decay products become increasingly soft and indistinguishable from SM backgrounds. Events that have an energetic ISR jet produced in association with parent sparticles, which recoils against the missing transverse momentum due to the LSP leaving the detector ("boosted events"), provide a clear signature in such scenarios. One high p_{T} jet alongside large $E_{\mathrm{T}}^{\mathrm{miss}}$ give rise to a monojet final state, in events where the soft sparticle decay products are too soft to observe.

Searches are for the pair production of top squarks ($\widetilde{\mathrm{t}}\widetilde{\bar{\mathrm{t}}}$) that decay to charm quarks and the LSP, $\widetilde{\mathrm{t}}\widetilde{\bar{\mathrm{t}}} \rightarrow \mathrm{c}\bar{\mathrm{c}}\,\widetilde{\chi}^0_1\widetilde{\chi}^0_1$, and bottom squarks ($\widetilde{\mathrm{b}}\widetilde{\bar{\mathrm{b}}}$) that decay to bottom quarks and the LSP, $\widetilde{\mathrm{b}}\widetilde{\bar{\mathrm{b}}} \rightarrow \mathrm{b}\bar{\mathrm{b}}\,\widetilde{\chi}^0_1\widetilde{\chi}^0_1$. By selecting events using particles produced alongside $\widetilde{\mathrm{t}}\widetilde{\bar{\mathrm{t}}}$ or $\widetilde{\mathrm{b}}\widetilde{\bar{\mathrm{b}}}$, the search is sensitive to mass differences of less than 10 GeV. The search presented here is a re-optimization of the well-established search detailed in Refs. [119–121], performed by the author as part of the CMS monojet group. By modifying the search criteria to cut out the soft jets, sensitivity to compressed mass spectra is achieved.

5.2 Data samples

The data for this search were collected using a combination of two triggers at the HLT. The first requires events to have $E_{\mathrm{T}}^{\mathrm{miss}} > 120$ GeV. The second, a dedicated monojet trigger, requires a central jet ($|\eta| < 2.6$) with $p_{\mathrm{T}} > 80$ GeV and $E_{\mathrm{T}}^{\mathrm{miss}}$ (calculated without muons) to be greater than 95 or 105 GeV. These triggers also have coarse noise cleaning filters applied. The first has various requirements on the energy deposits in the HCAL to

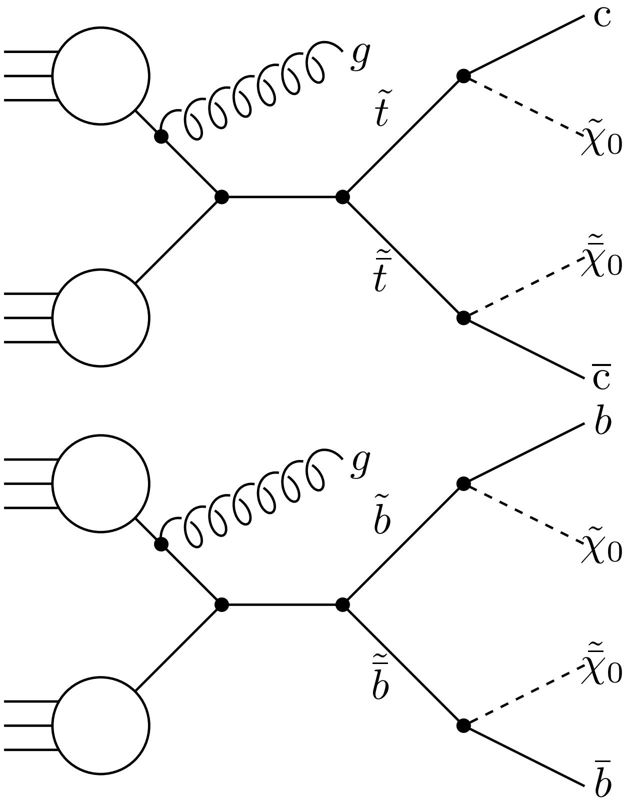

Figure 5.1: Feynman diagrams of the signals probed. The top diagram shows the FCNC process $\widetilde{\mathrm{t}}\,\widetilde{\bar{\mathrm{t}}} \rightarrow \mathrm{c}\bar{\mathrm{c}}\,\widetilde{\chi}^0_1\,\widetilde{\chi}^0_1$ and the bottom diagram shows the process $\widetilde{\mathrm{b}}\,\widetilde{\bar{\mathrm{b}}} \rightarrow \mathrm{b}\bar{\mathrm{b}}\,\widetilde{\chi}^0_1\,\widetilde{\chi}^0_1$. In both cases, an ISR gluon leads to an energetic jet, and balances the $E_{\mathrm{T}}^{\mathrm{miss}}$ due to LSPs escaping the detector leaving no trace.

cut out noisy events, and the second demands that the neutral energy deposited in the ECAL is less than 95% of the total energy deposited. They are seeded by L1 triggers which require the missing transverse momentum, calculated using L1 seeds and in L1 energy units, to be greater than 36, 40 or 50 for the first trigger, or greater than 40 for the second trigger.

Very few events with $E_{\mathrm{T}}^{\mathrm{miss}}$ (reconstructed offline) below 100 GeV will pass the analysis triggers described above, which require $E_{\mathrm{T}}^{\mathrm{miss}}$ (calculated online) to be above 120 GeV , or, (without muons) to be above 95 or 105 GeV . However, most events with $E_{\mathrm{T}}^{\mathrm{miss}}$ (reconstructed offline) above 200 GeV will pass the same analysis triggers. To calculate the efficiency of these triggers in terms of the key analysis variables, $E_{\mathrm{T}}^{\mathrm{miss}}$ and the p_{T} of the leading jet, an independent sample of events collected using a trigger requiring a single isolated muon with $p_{\mathrm{T}} > 24$ and $|\eta| < 2.4$ is used. The efficiency is given by the ratio of the number events passing the analysis triggers to the number of events passing the reference trigger. It is shown in the trigger turn-on curves in Figure 5.2

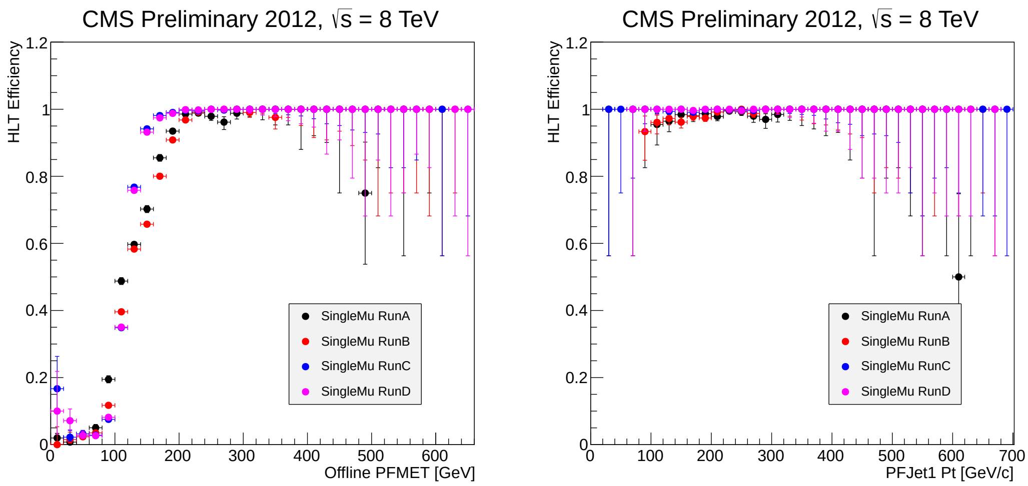

Figure 5.2: The trigger efficiency as a function of the $E_{\mathrm{T}}^{\mathrm{miss}}$ (left) and p_{T} of the leading jet (right).

Table 5.1: Datasets used in this analysis, with a total integrated luminosity of 19.7 fb^{-1}.

Era	Dataset	Int. Lumi. [pb^{-1}]
2012A	/MET/Run2012A-22Jan2013-v1/AOD	889
2012B	/MET/Run2012B-22Jan2013-v1/AOD	4429
2012C	/MET/Run2012C-22Jan2013-v1/AOD	7152
2012D	/METParked/Run2012D-22Jan2013-v1/AOD	7315

as a function of $E_{\mathrm{T}}^{\mathrm{miss}}$ and the p_{T} of the leading jet, as reconstructed offline. Here, the different colours show the different runs of the LHC during Run I. The dedicated monojet trigger described above was introduced for Run C, which increased the efficiency of the combination of the triggers for lower values of $E_{\mathrm{T}}^{\mathrm{miss}}$ and leading jet p_{T} compared to Runs A and B. The plots in Figure 5.2 show that the trigger paths become almost 100% efficient at $p_{\mathrm{T}}(j_1) \sim 110$ GeV and $E_{\mathrm{T}}^{\mathrm{miss}} \sim 220$ GeV.

The specific datasets used for this analysis, along with their integrated luminosities, can be found in Table 5.1. The data are from a 'good-run' list of LHC runs, in which each of the subsystems of the CMS detector were operating well, and therefore event reconstruction was optimal. Events were re-reconstructed using the `CMSSW_5_3_9_patch3` release of the CMS software (CMSSW), and form a part of the legacy dataset from Run I of CMS running.

5.3 Background MC simulation

MC simulation of SM backgrounds are used, directly and indirectly, to estimate the contribution of SM backgrounds to the number of events in the search regions. The SM processes considered are; single top quark and top quark pair production ($\mathrm{t\bar{t}}$), W or Z bosons produced in association with jets, diboson (W W, W Z, Z Z, W γ and Z γ) production and QCD multijet processes.

The simulation of each sample follows a similar procedure. Events are generated using a matrix element event generator such as MADGRAPH [129, 130], which simulates the underlying process at parton level. The event is then passed through a parton showering programme, usually PYTHIA [131–133] in which partons undergo hadronization: quarks hadronize into jets. It is finally passed through a simulation of the CMS detector to mimic the detector's response to the event. All simulated SM background events have gone through a GEANT4 [134, 135] simulation of the detector. This is a 'full' simulation, computationally expensive and providing accurate responses to the simulated physics objects. For simulation of signal (detailed later), a 'fast' simulation [136] is used instead as it is around 100 times faster to process each event and has a comparable accuracy.

Samples of Z bosons decaying invisibly (Z ($\nu\bar{\nu}$) + jets), $\mathrm{t\bar{t}}$, and diboson events are simulated using MADGRAPH 5 interfaced with PYTHIA 6.4.24. To evaluate the content of the proton in the initial state, the CTEQ6L Parton Density Functions (PDFs) are used [137]. Samples are simulated using the custom CMS event tune Z2*, which is derived from the Z1 tune [133] which uses the CTEQ5L PDFs, whereas the Z2* uses the CTEQ6L set. Simulated Z + jets and W + jets events are generated in the same way, where a cut has been placed on the transverse momentum of the boson, $p_{\mathrm{T}} > 100$ GeV, in order to increase the number of generated events that pass offline selection requirements (and where the production cross section has been modified accordingly). QCD multijet events are generated with PYTHIA 6.4.24, again using tune Z2* and CTEQ 6L1 PDFs. Single top quark processes (s-channel, t-channel and tW-channel production) are generated using POWHEG [138, 139]. Decays of the τ lepton are simulated using the TAULOA 27.121.5 package [140].

To ensure no double counting in phase space between the underlying event and the fragmentation and hadronization process, the MLM shower matching prescription [141] is used, in which partons from the matrix element calculation are matched to jets resulting from the hadron shower. In order to avoid double counting photons from the PYTHIA shower in W + jets and W γ samples (and similarly for Z + jets and Z γ samples), events from the W + jets and Z + jets simulation which have a photon from ISR or Final State Radiation (FSR), of $p_{\mathrm{T}}(\gamma) > 5$ GeV, are removed.

5.4 Object reconstruction

In Chapter 3 the CMS detector and reconstruction methods are discussed at length, including those used in this analysis. Here, I briefly recap the important features of the object reconstruction and give more detail on the object definitions.

5.4.1 Jets and $E_{\mathrm{T}}^{\mathrm{miss}}$

Jets and $E_{\mathrm{T}}^{\mathrm{miss}}$ are reconstructed using a PF technique [101]. The algorithm produces a unique list of particles in each event, using the combined information from all CMS subdetectors. This list is then used as input to the jet clustering, which reconstructs jets using the anti-k_{T} algorithm [100] with a distance parameter of 0.5. The missing transverse energy vector is computed as the negative vector sum of the transverse momenta of all particles reconstructed in the event, except muons.

Jet energies are corrected to establish a uniform calorimeter response in η and an absolute response in p_{T} calibrated at the particle level. Jet Energy Scale (JES) corrections are derived from simulation, and a residual correction is derived from the data by measuring the p_{T} balance in dijet events [?]. The jet energy corrections used are 'L2L3Residual' and 'L1FastJet'. To resolve any ambiguity in the reconstruction of jets and leptons, a jet is removed from the event if the energy fraction of an electron or muon in the jet is greater than 0.5.

5.4.2 Leptons

Leptons are also reconstructed using the PF algorithm and the definitions of objects are in accordance with the CMS recommendations. In addition to muons, electrons and τ leptons are also used in the analysis. Muons either pass a "loose" or "tight" selection criteria (which has more stringent requirements). Electrons must pass a "loose" selection criteria, and the Hadron–Plus–Strips (HPS) algorithm with "loose" criteria is used to reconstruct hadronically decaying τ leptons (τ_{h}).

A loose muon must have p_{T} greater than 10 GeV, and be tagged as a Global or Tracker muon – meaning that it must have independent tracks from both the tracker and the muon systems that join together, or that a series of hits in the tracker matches up with at least one hit in the muon system [142]. A tight muon must have p_{T} greater than 20 GeV and be central – $|\eta| < 2.4$. It must also be considered a Global muon, with additional requirements on the global muon track. There must be at least one hit from the muon chambers included in the global track, and the χ^2 of the global track must be less than 10. These requirements suppress mistaken muon identification as a result of hadronic punch-through from the HCAL and the magnet, and suppress muons originating from in-flight decays. There must also be hits in at least two of the muon stations, which acts to reduce the number of accidental track-to-segment matches. In order to suppress the number of cosmic muons (and further suppress muons from in-flight decays), the transverse impact parameter of the track (d_{xy}) as reconstructed in the tracker must be less than 2 mm from the primary vertex. Requiring the longitudinal impact parameter (d_z) to be less than 5 mm has a similar effect, as well as reducing the number of muons which originate from PU. Additional demands on the number of hits in the pixel system (> 0) and the number of tracker layers with hits (> 5) further suppress in-flight muon decays, and guarantee a good measurement of the muon p_{T}.

The electron identification used in the analysis is loose. To be classified as an electron, a track in the tracker must match up to a supercluster in the ECAL. The p_{T} must be greater than 10 GeV, and the electron reconstruction avoids the gap between the ECAL barrel and endcap where there is no instrumentation: $1.44 < |\eta| < 1.56$. In addition, various simple parameters regarding the supercluster shower shape, matching between the ECAL cluster and track, the ratio of energy deposited in the ECAL and HCAL, and impact parameters distinguish between primary electrons and those originating from bremsstrahlung and photon pair conversion. More information can be found in Ref. [143].

To ensure that electrons and muons are isolated – not close to a jet or other object – they must satisfy requirements on the isolation parameter R, defined as

$$R = \frac{\sum E_{\mathrm{T\ charged\ hadrons}} + \sum E_{\mathrm{T\ neutral\ hadrons}} + \sum E_{\mathrm{T\ photons}}}{p_{\mathrm{T}}}, \tag{5.1}$$

where the hadrons and photons are considered in a cone with radius $\sqrt{\Delta\phi^2 + \Delta\eta^2} = 0.4$ around the lepton direction. Tight muons must have $R < 0.2$, and loose electrons must have $R < 0.15$. Isolations are corrected for the effect of PU using $\Delta\beta$ corrections [144].

The τ lepton decays hadronically 65% of the time, with the dominant decay modes consisting of one or three charged $\pi^{\pm}$ mesons, and up to two neutral π^0 mesons. The HPS algorithm first reconstructs the π^0 component of the τ_h decay using a PF anti-$\mathrm{k_T}$ jet with distance parameter 0.5, and then combines with charged hadrons to build a τ_h. 'Strips' are constructed from PF photons and electrons, starting with the most energetic electromagnetic particle within the seed jet, and combining all surrounding electromagnetic particles. Strips with $p_\mathrm{T} > 1$ GeV are then combined with charged hadrons to provide a τ_h candidate. Here, the candidate must have $p_\mathrm{T} > 20$ GeV and $|\eta| < 2.3$ and the loose requirements of the algorithm are used which correspond to approximately 1% of jets to be misidentified as a τ_h. Again, $\Delta\beta$ corrections account for PU. More information can be found in Ref. [145].

5.5 Event selection

The aim is to select signal candidate events while rejecting as much background as possible. A final state with one, high p_T leading jet, and large $E_\mathrm{T}^\mathrm{miss}$ from the LSPs leaving the detector form the basis of the event selection in order to be sensitive to compressed SUSY signatures.

5.5.1 Event Cleaning

The first stage of the event selection, after the trigger, is to reject any events that have passed the trigger due to instrumental noise or non-collision backgrounds.

Events are required to have at least one well-reconstructed primary vertex [146], where it is reconstructed in a 24 cm window along the beam axis, within a radius of $\rho < 2$ cm orthogonal to the plane of the beam. To reject events that have "scraping" tracks due to beam-gas interactions close to the interaction point, in events where there are 10 or more tracks at least 25% must be good quality; that is, satisfy various requirements on the number of hits, the p_T of the track, the χ^2 of the combination of hits which build the track etc. To remove events with spurious $E_\mathrm{T}^\mathrm{miss}$ reconstruction, different methods of calculating the $E_{\mathrm{T}}^{\mathrm{miss}}$ are compared. The value of $E_{\mathrm{T}}^{\mathrm{miss}}$, reconstructed using the PF algorithm, must be comparable with the $E_{\mathrm{T}}^{\mathrm{miss}}$ calculated using calorimetric information only: events with (PF $E_{\mathrm{T}}^{\mathrm{miss}}$ - calo $E_{\mathrm{T}}^{\mathrm{miss}}$)$> 2\times$ calo $E_{\mathrm{T}}^{\mathrm{miss}}$ are discarded.

Beam-halo and other beam-related backgrounds [147], which arise when the beams interact with the beam pipes, can deposit energy in both the ECAL and HCAL leaving no associated tracks. Cosmic muons also can give rise to fake $E_{\mathrm{T}}^{\mathrm{miss}}$, or leave similarly spurious deposits - leading to fake jets - as they deposit energy in one or more of the subdetectors while leaving no tracks, or tracks which do not originate from the primary vertex. Similarly, instrumental noise can lead to large apparent deposits in the ECAL or HCAL. Stringent requirements are therefore placed on the neutral and charged hadronic and electromagnetic content of jets:

- Leading jet charged electromagnetic fraction < 0.7
- Leading jet charged hadronic fraction > 0.2
- Leading jet neutral electromagnetic fraction < 0.7
- Leading jet neutral hadronic fraction < 0.7
- Second jet neutral electromagnetic fraction < 0.9
- Second jet neutral hadronic fraction < 0.7

These conditions also reject high p_{T} photons and electrons which are misidentified as jets due to energy deposits in the HCAL; the energies assigned to neutral hadrons in the ECAL and HCAL must sum to less than 70% of the total jet energy. In addition, jets are also required to pass a loose identification criterion which rejects fake jets due to calorimeter noise.

The distributions for the neutral and charged energy fractions of the first and second jet in events (where jets are p_{T} ordered) before and after these set of noise cleaning cuts are applied are shown in Figures 5.3 and 5.4. They are very effective at removing noisy events, with good data/MC agreement after the cuts have been applied.

5.5.2 Signal region event selection

Once events passing the trigger have been filtered to remove noise and fakes, events are selected to optimise signal acceptance while rejecting as much background as possible.

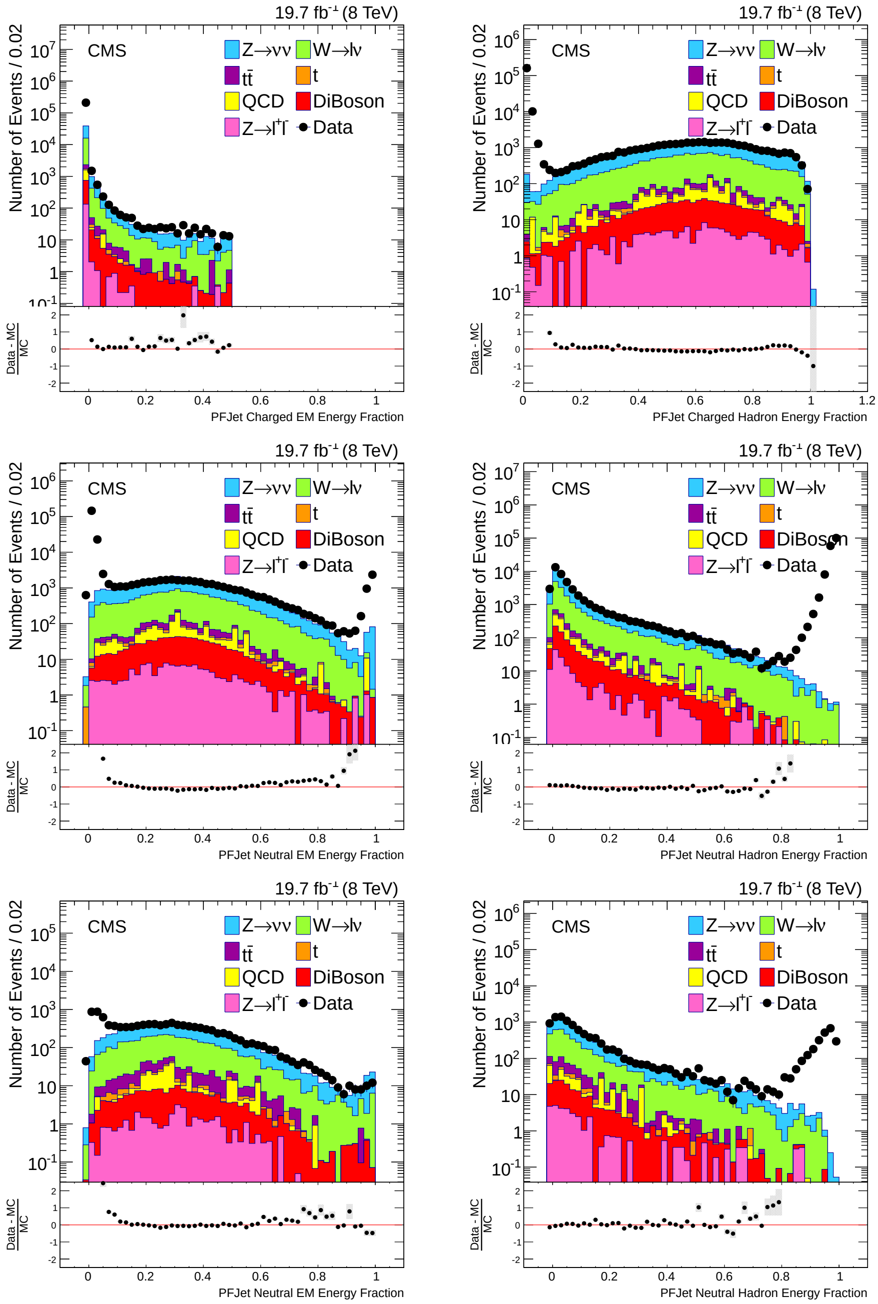

Figure 5.3: Hadronic and electromagnetic energy fractions from charged and neutral particles, before cleanup cuts on these quantities are applied. We require the charged hadronic fraction of the jet to be above 20% and the neutral electromagnetic and hadronic energy fractions to be below 70% of the total leading jet energy. We require the neutral electromagnetic energy to be below 90% and the neutral hadronic energy of the second jet to be below 70% of the total second leading jet energy.

To satisfy trigger requirements, and ensure all events comfortably pass the HLT trigger selection, events are required to have $E_{\mathrm{T}}^{\mathrm{miss}} > 250$ GeV and the most energetic jet (j_1) in

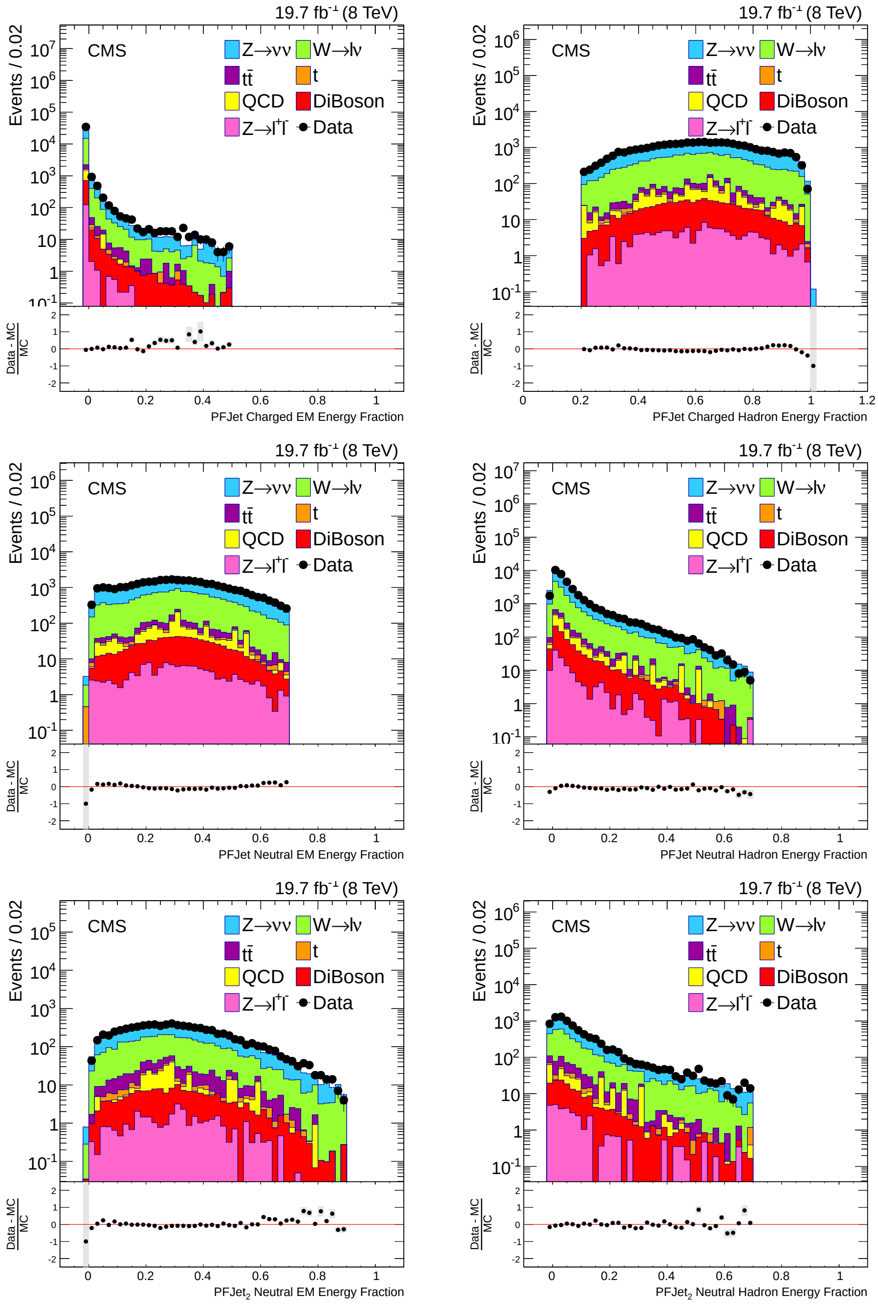

Figure 5.4: Hadronic and electromagnetic energy fractions from charged and neutral particles, after clean-up cuts on these quantities are applied.

the event is required to have $p_{\mathrm{T}}\left(\mathrm{j}_1\right) > 110$ GeV and $\left|\eta\left(\mathrm{j}_1\right)\right| < 2.4$. Signal acceptance is increased by allowing events where there is a second jet originating from ISR (or FSR); however the signal also has soft final-state jets originating from the sparticle decay products. To ensure that these soft final-state jets coming from charm or bottom quarks remain invisible within the event selection, and a monojet signature is maintained, the

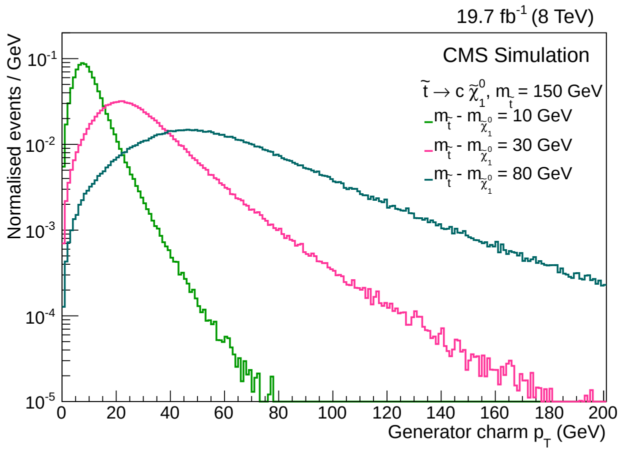

Figure 5.5: Charm quark p_T spectra for mass splittings across the phase space range, $m_{\tilde{t}} - m_{\tilde{\chi}^0_1} = 10, 30, 80$ GeV , for a top squark mass of 150 GeV .

p_T threshold at which the second and third jets are counted must be high enough that the soft-hadronic (signal) decay products fall below it for a good range of signal phase space while keeping the QCD multijet background at a manageable level. Figure 5.5 shows the p_T distribution of charm quarks, taken from simulation, for a few representative mass hypotheses in the process $\tilde{t}\bar{\tilde{t}} \to c\bar{c}\,\tilde{\chi}^0_1\tilde{\chi}^0_1$. Placing the jet counting threshold at $p_T > 60$ GeV , and requiring $|\eta| < 4.5$, is a good compromise between signal efficiency and background rejection. Events are therefore vetoed if they contain more than 2 jets, where $p_T(j_1) > 110$ GeV and $|\eta| < 2.4$; $p_T(j_2) > 60$ GeV and $|\eta| < 4.5$; and the third jet is counted (and the event rejected) if it has $p_T(j_3) > 60$ GeV and $|\eta| < 4.5$. A monojet-like topology in signal events is therefore maintained, allowing the search to be sensitive to both highly compressed spectra and extending the scope to larger mass differences.

In order to reduce the background from Z and W -boson decays, events with leptons are rejected. Events containing a PFElectron with $p_T > 10$GeV and passing the WP95 selection and isolation requirements are rejected. Events containing a PFMuon with $p_T > 10$ GeV and reconstructed as a Global and/or PF muon are also rejected. This follows recommendations from the 2012 Muon POG for a loose ID PF muon.

The analysis is performed in 7 inclusive regions of the leading jet p_T ; $p_T > 250$, 300, 350, 400, 450, 500 and 550 GeV .

5.5.3 Control region event selection

A control sample of μ +jet events is used to estimate backgrounds in a data-driven way. In order to get a very clean control sample muons are required to pass Tight Muon selection requirements as recommended by the Muon POG. In addition to kinematic and identification requirements, muon candidates are also required to be isolated using the combined relative isolation variable as defined by the Muon POG for a cone of radius 0.12.A summary of the kinematic, identification and isolation selection criteria for muons is shown below.

Muon Identification

- $p_{\mathrm{T}} > 20$ GeV
- $|\eta| < 2.4$
- Global and PF muon
- $|d_{xy}| < 2$ mm
- $|dz| < 5$ mm
- $\chi^2/\mathrm{dof} < 10$
- R < 0.12
- Tracks associated to muons must satisfy:
  - at least one hit in pixel,
  - at least one muon chamber hit included in the global-muon track fit
  - segments in at least two muon stations.
  - at least 5 tracker layers with hits

A summary of all the selection criteria is given in Appendix **??**. Some of the kinematic distributions are shown in Figure 5.6.

Table 5.2 lists the number of events selected at each step of the analysis, for data and simulation.

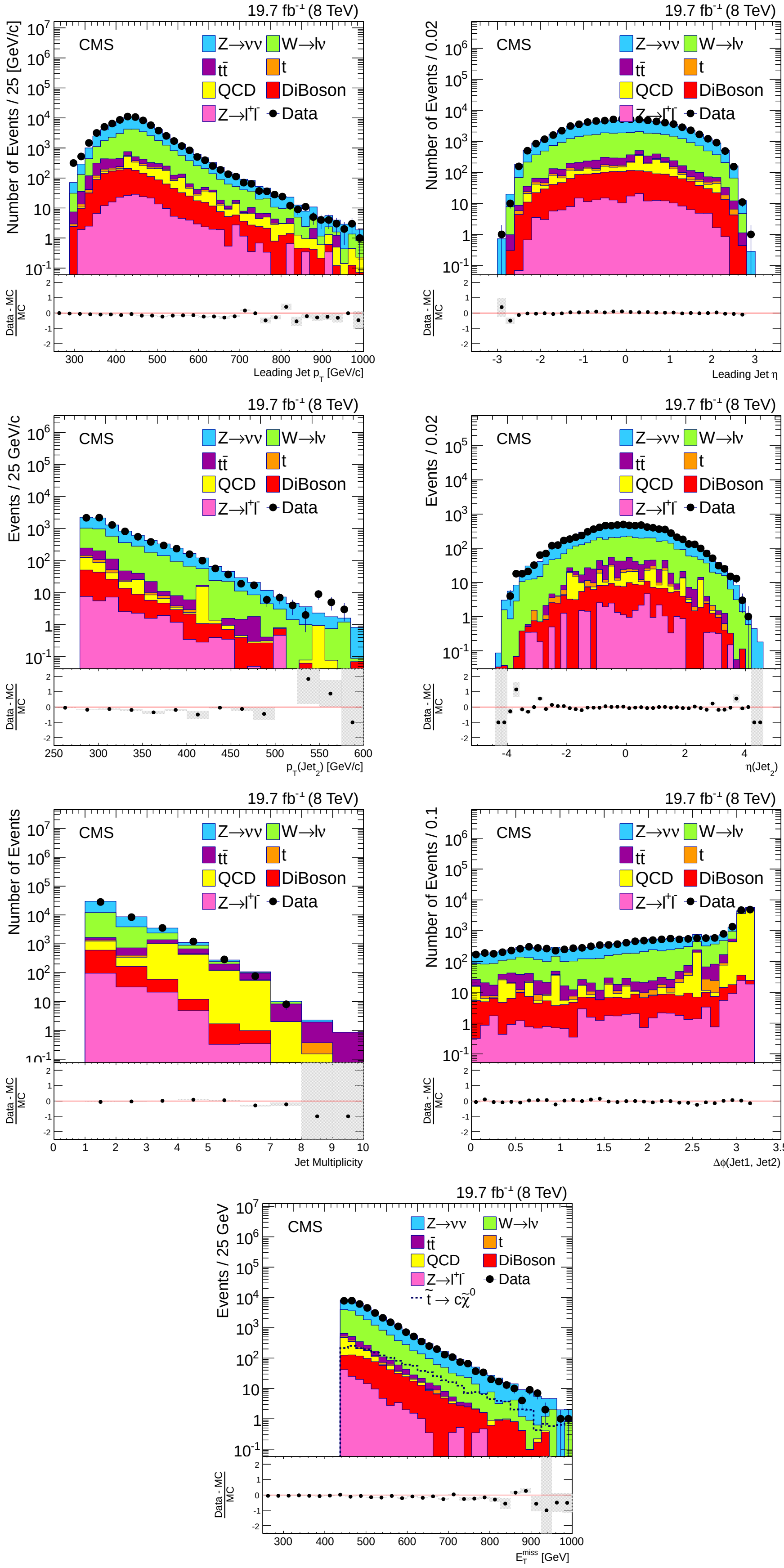

Figure 5.6: Plots of basic selection variables. All figures except for the p_T and η of the second leading jet are N-1 plots so all cuts are applied except the one being plotted (the leading jet p_T cut for all plots except the jet p_T and jet η is set to 110 GeV). The

Table 5.2: Number of events selected at each step of the analysis, for data and simulation. Backgrounds are obtained from MC and normalised as described in Appendix **??**.

Selection	W + jets	Z + jets	Z $\rightarrow \nu\bar{\nu}$ + jets	Diboson	$t\bar{t}$	Single top	QCD	Total BG
Cross section (pb)	228.9	40.5	588.3	234.0	1.085e6	114.8	105.7	
Trigger	2514352	190332	4337526	65666	461413	77284	5429269	13075841
$E_{\mathrm{T}}^{\mathrm{miss}} > 200$ GeV	317656	30242	134578	9572	63174	9289	87605	652117
Noise Cleaning	292550	27880	123420	8706	59412	8525	81668	602162
$p_{\mathrm{T}}(\mathrm{j}_1) >$110 GeV	279323	26652	117513	8045	53353	7752	80844	573484
$N_{\mathrm{jets}} \leq 2$	254058	24413	109313	7287	29364	5596	44247	474278
$\Delta\phi(j_1, j_2) < 2.5$	237533	22947	104158	6984	25312	4815	8433	410181
Muon veto	106236	1511	104152	4051	9826	1892	7444	235112
Electron veto	79407	1004	104065	3459	6557	1325	7401	203218
Tau veto	71808	807	103106	3248	5599	1147	7047	192762
$p_{\mathrm{T}}(\mathrm{j}_1) >$250 GeV, $E_{\mathrm{T}}^{\mathrm{miss}} >$250 GeV	13641	127	22615	639	602	172	819	38615
$p_{\mathrm{T}}(\mathrm{j}_1) >$300 GeV	6873	75	11093	369	344	97	546	19397
$p_{\mathrm{T}}(\mathrm{j}_1) >$350 GeV	3182	40	5231	206	178	49	332	9218
$p_{\mathrm{T}}(\mathrm{j}_1) >$400 GeV	1501	25	2617	113	91	21	181	4549
$p_{\mathrm{T}}(\mathrm{j}_1) >$450 GeV	751	17	1335	64	48	11	92	2318
$p_{\mathrm{T}}(\mathrm{j}_1) >$500 GeV	376	11	727	36	27	5.2	61	1244
$p_{\mathrm{T}}(\mathrm{j}_1) >$550 GeV	204	7.4	406	21	18	3.2	34	693

5.6 Data driven background estimation

The dominant backgrounds remaining after the monojet event selection are electroweak backgrounds from "invisible Z" decays and W + jets. Both of these backgrounds are estimated from data by selecting a control sample of μ +jet events, where Z $\rightarrow \mu^+\mu^-$ + jets is used to predict the invisible Z background and W $\rightarrow \mu\nu$ + jets is used to predict the remaining W + jets background. This muon control sample is derived from the same dataset as the signal.

The control samples are obtained by applying the full monojet selection with the exception of the lepton veto. To obtain a sample of Z $\rightarrow \mu^+\mu^-$ events, one well identified and isolated muon satisfying the selection in Section 5.5 is required and the invariant mass of this muon with another reconstructed muon in the event is required to be between 60 and 120 GeV. A sample of W $\rightarrow \mu\nu$ + jets is similarly obtained by requiring one well identified and isolated muon and with a reconstructed W transverse mass between 50 and 100 GeV.

Tables 5.3 and 5.4 show the event yields obtained for the Z $\rightarrow \mu^+\mu^-$ and W $\rightarrow \mu\nu$ control samples and the predicted backgrounds from MC.

Table 5.3: Event yields for the Z $\rightarrow \mu^+\mu^-$ data control samples and the backgrounds from MC. 50% uncertainty is assigned to each background (i.e. from $t\bar{t}$, single top, and diboson events) and these are combined in quadrature to get the total uncertainty on the number of background events in the Z $\rightarrow \mu^+\mu^-$ sample.

	Z + jets	W + jets	Z $\rightarrow \nu\bar{\nu}$ + jets	$t\bar{t}$	Single t	QCD	Diboson	All MC	Data
p_T (j$_1$) >250 GeV	3067	0	0	37	5.7	0	68	3177	2547
p_T (j$_1$) >300 GeV	1577	0	0	21	2.2	0	41	1641	1235
p_T (j$_1$) >350 GeV	757	0	0	9.9	0.9	0	24	791	567
p_T (j$_1$) >400 GeV	382	0	0	4.8	0.9	0	13	401	277
p_T (j$_1$) >450 GeV	198	0	0	0.7	0	0	8.2	207	150
p_T (j$_1$) >500 GeV	109	0	0	0	0	0	4.4	113	79
p_T (j$_1$) >550 GeV	62	0	0	0	0	0	2.6	65	40

Table 5.4: Event yields for the $W \rightarrow \mu\nu$ data control samples and the backgrounds from MC. 50% uncertainty is assigned to each background (i.e. from Z + jets, $t\bar{t}$, single top, QCD and diboson events) and these are combined in quadrature to get the total uncertainty on the number of background events in the $W \rightarrow \mu\nu$ sample.

	Z + jets	W + jets	Z $\rightarrow \nu\bar{\nu}$ + jets	$t\bar{t}$	Single t	QCD	Diboson	All MC	Dat
p_T (j$_1$) >250 GeV	11436	183	0	608	158	0.3	197	12582	1137
p_T (j$_1$) >300 GeV	5712	94	0	313	80	0.3	121	6320	547
p_T (j$_1$) >350 GeV	2694	44	0	151	41	0.3	71	3001	254
p_T (j$_1$) >400 GeV	1349	22	0	76	22	0.3	41	1509	125
p_T (j$_1$) >450 GeV	712	9.9	0	41	13	0.3	22	798	668
p_T (j$_1$) >500 GeV	389	6.6	0	20	7.8	0.3	13	437	352
p_T (j$_1$) >550 GeV	223	3.7	0	11	4.8	0.3	6.5	249	184

A comparison between data and MC for the dimuon invariant mass and momentum after all the selection cuts and a p_T (j1) cut of 250 GeV is shown in Figure 5.7.

A comparison between data and MC for the transverse mass and momentum of the W after the full selection and for p_T (j$_1$) > 250GeV is shown in Figure 5.8.

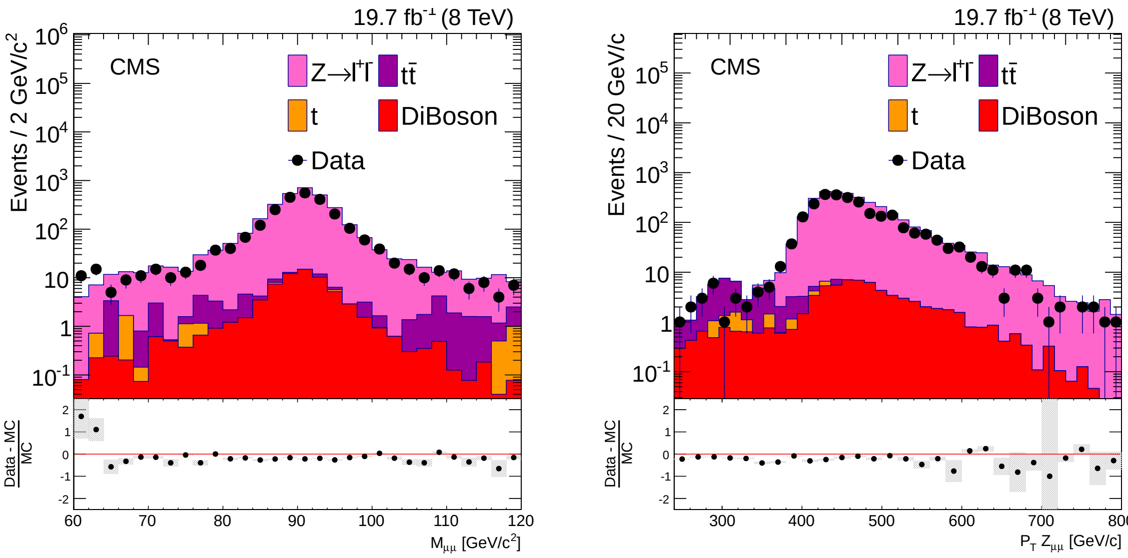

Figure 5.7: Invariant mass and transverse momentum of the dimuon pair in the Z $\rightarrow \mu^+\mu^-$ control sample.

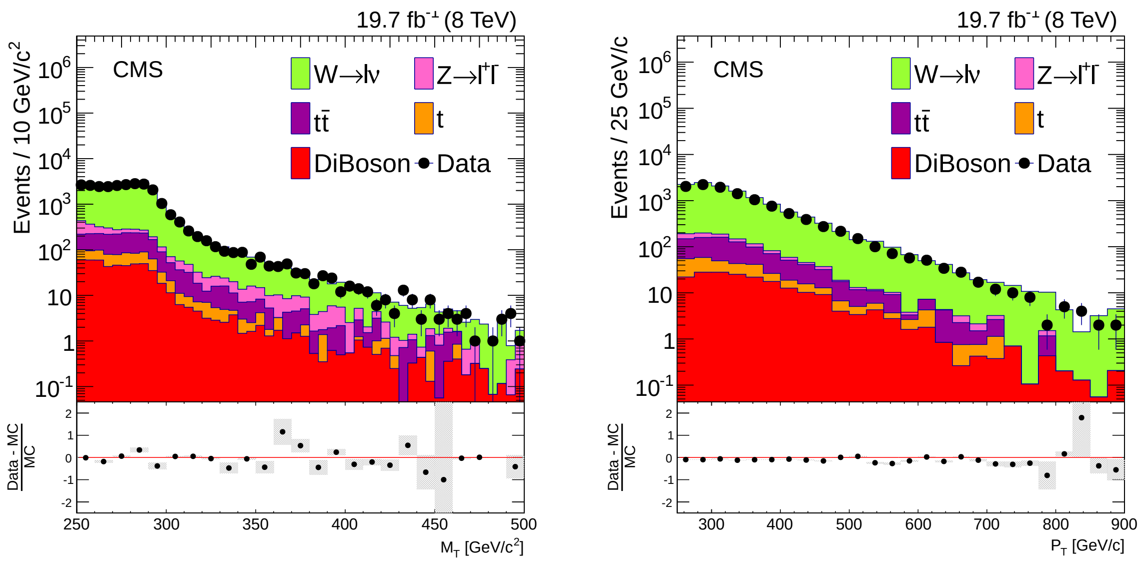

Figure 5.8: Transverse mass M_T of the muon (left) and transverse momentum of $W^{\pm}$ candidates in the W mass window, $50 - 100\text{GeV}$ in the $W \rightarrow \mu\nu$ sample.

5.6.1 Estimation of Z $\rightarrow \nu\bar{\nu}$ background

The Z $\rightarrow \mu^+\mu^-$ and Z $\rightarrow \nu\bar{\nu}$ events share similar kinematic characteristics and by interpreting the pair of muons as missing energy, the topology of the process in which the Z boson decays to neutrinos can be reproduced. The missing transverse energy in the Z $\rightarrow \mu^+\mu^-$ event is defined as the vector sum of the transverse momentum of the muons and the $E_{\mathrm{T}}^{\mathrm{miss}}$. The number of Z $\rightarrow \nu\bar{\nu}$ events can then be predicted using:

$$N(Z \rightarrow \nu\nu) = \frac{N_{obs} - N_{bgd}}{A * \epsilon} \cdot R \tag{5.2}$$

where N_{obs} is the number of observed dimuon events, N_{bgd} is the number of background events contributing to the dimuon sample, A is the fiducial and kinematic acceptance of the detector and the efficiency of the Z mass window cut, ϵ is the selection efficiency of the event and R is the ratio of branching fractions for the Z decay to neutrinos and a pair of muons. These factors are determined as follows:

- N_{bgd} : The dimuon sample comprises predominantly of Z $\rightarrow \mu^+\mu^-$ events with less than 1% contamination from background. The backgrounds are taken from Monte Carlo and a 50% uncertainty is assigned to the number.
- A : The acceptance A is defined as the fraction of all generated events where the muons are reconstructed with $p_{\mathrm{T}} > 20$ GeV and $|\eta| < 2.1$ and the invariant mass of the muons is within 60 GeV and 120 GeV. This is obtained from Z+jets MC using generator level information.
- ϵ : The event selection efficiency ϵ is defined as the efficiency of reconstructing muons passing all the identification and isolation criteria and with a reconstructed invariant mass between 60 and 120 GeV, given that they are within the detector acceptance. The efficiency is taken from MC. It is corrected by a scale factor to account for the difference in selection efficiency between data and MC.
- R : The ratio of the branching fraction $R = (\frac{BF(\mathrm{Z}(\nu\bar{\nu}))}{BF(\mathrm{Z}(\mu\mu))})$ is obtained from [?] and is 5.942 ± 0.019 when $l = \mu$.

The selection of Z $\rightarrow \mu^+\mu^-$ events relies upon counting the number of events at each $p_{\mathrm{T}}(\mathrm{j}_1)$ cut, which is correlated to the PF METnoMu. We interpret the muons as missing energy, and add their p_{T} into the PF MET in the redefinition of the $E_{\mathrm{T}}^{\mathrm{miss}}$. The momentum is balanced by $p_{\mathrm{T}}(\mathrm{j}_1)$. This exploits the similar kinematics of Z $\rightarrow \nu\bar{\nu}$ and Z $\rightarrow \mu^+\mu^-$ events, treating the muons as neutrinos. The estimate of METnoMu and $p_{\mathrm{T}}(\mathrm{j}_1)$ therefore relies upon successfully identifying both muons in the muonic Z decay, in order to add them into the $E_{\mathrm{T}}^{\mathrm{miss}}$ and imitate an invisible Z decay where of course both neutrinos contribute to the $E_{\mathrm{T}}^{\mathrm{miss}}$ and so $p_{\mathrm{T}}(\mathrm{j}_1)$.

If either (or both) muons in a $Z \rightarrow \mu^+\mu^-$ decay is not properly identified, for example the muon does not pass identification requirements but the track is reconstructed, the energy of the muon will be included within the PF MET calculation and our procedure does not remove it. This event is likely to fail a METnoMu or $p_T\,(j_1)$ cut. It will not contribute to the total number of $Z \rightarrow \mu^+\mu^-$ events and therefore reduce the total $Z \rightarrow \nu\bar{\nu}$ estimation. However, if it had of been a $Z \rightarrow \nu\bar{\nu}$ event, both neutrinos would lead to genuine missing energy and so in missing such events we have under-estimated the $Z \rightarrow \nu\bar{\nu}$ background.

In order to correct for this effect we count the number of events in MC where METnoMu $/p_T$ gen Z < 0.7 in each inclusive $p_T\,(j_1)$ bin. A threshold value of 0.7 is chosen as the Z resolution is ~ 0.3 and we wish to count events in the tail of the Z mass spectrum. This gives an estimate of the number of events where we have not properly measured or identified one or two of the muons. The ratio, typically $< 5\%$, is calculated in each $p_T\,(j_1)$ bin and combined with the difference in efficiency for a TL or TT muon selection. A correction factor dependent on the signal region of order 5% is therefore applied.

A correction factor is also applied to R, to account for contamination from g^*. α is the fraction of g^* component in the Z, found from the difference in normalised $Z \rightarrow \mu^+\mu^-$ and $Z \rightarrow \nu\bar{\nu}$ samples in the Z mass window. β is the fraction of events lying outside the Z mass window in $Z \rightarrow \nu\bar{\nu}$ MC. The g^* contamination can be estimated using

$$g^* fraction = \frac{1-\alpha}{1-\beta} \tag{5.3}$$

Normalised across all $p_T\,(j_1)$ bins, we find a correction factor of 1.017.

Table 5.5 shows the observed $Z \rightarrow \mu^+\mu^-$ event yields and the correction factors for various E_T^{miss} cuts. Also shown is the estimated $Z \rightarrow \nu\bar{\nu}$ background and the total uncertainty on it.

5.6.2 Estimation of W + jets background

The second most dominant background arises from W+jet events that are not removed by the explicit lepton veto cut. These can come from hadronically decaying taus or events in which the lepton (electron or muon) is not identified, not isolated or not within the acceptance region. Such events in which the electron, muon or hadronic tau are effectively

Table 5.5: Summary of the Z $\rightarrow \mu^+\mu^-$ event yields and the efficiency factors used to predict the Z $\rightarrow \nu\bar{\nu}$ +jets background.

$p_{\mathrm{T}}\,(\mathrm{j}_1)$ (GeV)	> 250	> 300	> 350	> 400	> 450	> 500	> 550
N_{obs}	2547	1235	567	277	150	79	40
N_{bgd}	111	64	35	19	8.9	4.4	2.7
Acceptance A	0.805	0.833	0.851	0.864	0.881	0.905	0.896
Efficiency ϵ	0.862	0.843	0.822	0.802	0.775	0.751	0.754
g* corr. factor	1.017	1.017	1.017	1.017	1.017	1.017	1.017
Z $\rightarrow \nu\bar{\nu}$	21209 ± 1115	10077 ± 592	4597 ± 324	2250 ± 197	1250 ± 137	663 ± 94	334 ± 65

Table 5.6: Summary of the contributions to the total uncertainty on Z $\rightarrow \nu\bar{\nu}$ +jets background from the various factors used in the data-driven estimation.

$p_{\mathrm{T}}\,(\mathrm{j}_1)$ (GeV)	> 250	> 300	> 350	> 400	> 450	> 500	> 550
Statistics (N^{obs})	2.1	3.0	4.5	6.5	8.7	12	17
Background (N^{bgd})	1.6	2.0	2.4	2.7	2.9	2.9	3.5
Acceptance	2.0	2.1	2.1	2.2	2.4	2.5	2.9
Efficiency	2.1	2.1	2.3	2.6	3.3	4.4	5.5
R	2.0	2.0	2.0	2.0	2.0	2.0	2.0
Total	5.3	5.9	7.0	8.8	11	14	19

'lost' are estimated by using the $W \rightarrow \mu\,\nu$ +jets control sample. The W $\rightarrow \mu\,\nu$ events are first corrected for the acceptance (A') and efficiency of reconstructing the events ($\epsilon\,'$) in the detector to obtain the total number of generated events (N^{μ}_{tot}).

$$N^{\mu}_{tot} = \frac{N_{obs} - N_{bgd}}{A'\epsilon\,'} \tag{5.4}$$

This is subsequently weighted by the inefficiency factors (detailed below) to obtain the predicted number of events that would not be rejected by the lepton veto and thus remain in the monojet sample.

The total number of $W \rightarrow \mu\,\nu$ +jets events that are out of the acceptance and not identified/isolated can be written as:

$$N_{lost\mu} = N^{\mu}_{tot} * (1 - A_{\mu}\,\epsilon_{\,\mu}). \tag{5.5}$$

where A_{μ} is the acceptance and $\epsilon_{\,\mu}$ is the efficiency of the muon selection used in the lepton veto definition.

Similarly, for an estimation of the 'lost' electron background, we start with N^{μ}_{tot} and multiply by the ratio of the $W \rightarrow \mu\,\nu$ +jets and $W \rightarrow e\nu$ +jets events that are predicted at the generator level in MC (f_e) to obtain N_{tot} for electrons. The lost electron background is given by:

$$N^{e}_{tot} = N^{\mu}_{tot} * f_e, \;\text{ where } f_e = \frac{N^{e}_{gen}}{N^{\mu}_{gen}} \tag{5.6}$$

$$N_{loste} = N^{e}_{tot} * (1 - A_e\epsilon_{\,e}) \tag{5.7}$$

$$\tag{5.8}$$

where A_e is the acceptance and $\epsilon_{\,e}$ is the efficiency of the electron selection used in the lepton veto definition. The electron acceptance is obtained using generator level MC and the selection efficiency is also obtained from MC with an assumed data/MC scale factor of 1.0.

The component of the W + jets background from hadronic tau events is estimated in the same way. The ratio of the generated W $\rightarrow \mu\,\nu$ and hadronic tau events (f_{τ}) is taken from MC and used to obtain N_{tot} for tau events. This is subsequently weighted by the inefficiency of the tau selection used in the veto to obtain the 'lost' hadronic tau background.

$$N_{tot}^{\tau} = N_{tot}^{\mu} * f_{\tau}\,, \;\; \text{where } f_{\tau} = \frac{N_{gen}^{\tau}}{N_{gen}^{\mu}} \tag{5.9}$$

$$N_{lost\tau} = N_{tot}^{\tau} * (1 - A_{\tau}\,\epsilon_{\,\tau}\,) \tag{5.10}$$

$$\tag{5.11}$$

The tau ID efficiency is estimated from MC with a data/MC scale factor of 1.0 and assigned an uncertainty of 6% as recommended by the Tau POG. The electron and muon discriminants in the Tau ID selection can also result in the Tau veto rejecting electron and muon events. The probability of an electron or muon to fake a tau is estimated from the W + jets MC and found to be negligible (below 0.1%).

All of the above components can be summarised in a Master Equation for estimating the 'Lost' W background:

$$N_{lost} = \frac{N_{obs} - N_{bgd}}{A'\epsilon\,'} * \Big[(1 - A_{\mu}\,\epsilon_{\,\mu}\,) + f_e * (1 - A_e\epsilon_{\,e}) + f_{\tau}\,(1 - A_{\tau}\,\epsilon_{\,\tau}\,)\Big] \tag{5.12}$$

The factors in this equation used to estimate the lost muon, electron and hadronic tau backgrounds are detailed in Table 5.7. A summary of the estimated remaining W+jet events in the monojet sample is shown in Table 5.8.

The uncertainty on the W + jets estimation includes; the statistical uncertainty on the number of single-muon events in the data, a 50% uncertainty on the background events obtained from MC, an uncertainty on acceptance from PDFs (2%) and MC statistics and an uncertainty on the selection efficiency ϵ from the variation in the data/MC scale factor and MC statistics. A summary of the fractional contributions of these uncertainties to the total error on the W + jets background is shown in Table 5.9. It is dominated by statistical uncertainty on N_{obs} and 50% uncertainties assigned to N_{bkg}.

5.6.3 QCD Background Estimation

The QCD background is predicted using MC, with a scale factor derived from a QCD rich control region. The standard monojet event selection is applied to events, apart from those cuts which remove the majority of the QCD: $\Delta\phi\,(\mathrm{j}_1,\,\mathrm{j}_2) < 2.5$ and $N_{jets} < 3$. The p_{T} requirement used to count jets is varied between 20 and 80 GeV .

Table 5.7: Estimation of the remaining W + jets background from the lost electron, muon and hadronic tau contributions.

$p_T\,(j_1)$ (GeV)	>250	>300	>350	>400	>450	>500	>550
N_{obs}	11371	5477	2547	1258	668	352	184
N_{bgd}	1146	608	307	160	86	48	26
A'ϵ'	0.345	0.345	0.341	0.346	0.349	0.361	0.371
N^{μ}_{tot}	29666	14125	6573	3176	1666	841	425
Lost Muon							
$A_{\mu}\,\epsilon_{\mu}$	0.887	0.895	0.901	0.908	0.908	0.906	0.907
$N_{lost\mu}$	3350	1484	649	292	152	79	40
Lost Electron							
$A_e\epsilon_e$	0.615	0.684	0.734	0.771	0.793	0.815	0.823
f_e	0.374	0.465	0.548	0.610	0.653	0.706	0.727
N_{loste}	4273	2077	958	444	225	110	55
Lost Tau							
$A_{\tau}\,\epsilon_{\tau}$	0.253	0.284	0.298	0.296	0.294	0.341	0.325
f_{τ}	0.212	0.235	0.235	0.228	0.212	0.201	0.195
$N_{lost\tau}$	4704	2377	1083	510	249	112	56
N_{lost}	12328 ± 707	5939 ± 366	2690 ± 180	1246 ± 92	627 ± 52	301 ± 29	150 ± 18

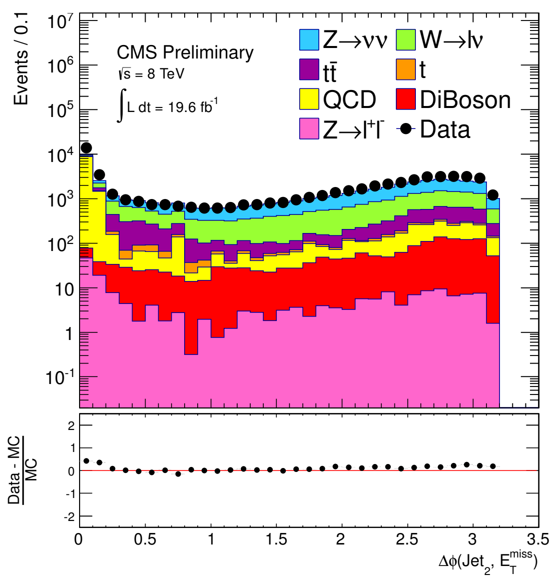

Figure 5.9: The QCD rich region dominated by back to back jets, $\Delta\phi\,(E_T^{miss}, j_2) < 0.3$, shown for a jet counting cut of 60 GeV for $p_T\,(j_1) > 250$GeV ..

Table 5.8: Summary of the estimated total remaining W + jets background.

$p_{\mathrm{T}}\,(\mathrm{j}_1)$ (GeV)	>250	>300	>350	>400	>450	>500	>550
N^{μ}_{tot}	29666	14125	6573	3176	1666	841	425
$\mathrm{N}_{lost\mu}$	3350	1484	649	292	152	79	40
N_{loste}	4273	2077	958	444	225	110	55
$\mathrm{N}_{lost\tau}$	4704	2377	1083	510	249	112	56
N_{lost}	12328 ± 707	5939 ± 366	2690 ± 180	1246 ± 92	627 ± 52	301 ± 29	150 ± 18

Table 5.9: Summary of the contributions (in %) to the total uncertainty on the W + jets background from the various factors used in the data-driven estimation.

$p_{\mathrm{T}}\,(\mathrm{j}_1)$ (GeV)	>250	>300	>350	>400	>450	>500	>550
Statistics (N_{obs})	1.0	1.5	2.3	3.2	4.4	6.2	8.6
Background (N_{bgd})	3.3	3.7	4.0	4.2	4.2	4.3	4.4
A'	2.0	2.0	2.0	2.0	2.0	2.1	2.1
$\epsilon\,'$	2.0	2.1	2.2	2.4	2.7	3.1	3.7
A_μ	0.1	0.1	0.2	0.2	0.3	0.4	0.5
$\epsilon_{\,\mu}$	0.1	0.1	0.2	0.2	0.3	0.4	0.6
A_e	0.7	0.9	1.0	1.1	1.2	1.3	1.3
$\epsilon_{\,e}$	0.7	0.9	1.0	1.1	1.2	1.3	1.4
A_τ	0.2	0.2	0.2	0.2	0.2	0.3	0.3
$\epsilon_{\,\tau}$	0.2	0.2	0.2	0.2	0.2	0.3	0.3
Total	5.7	6.2	6.7	7.4	8.2	9.7	12

The control region $\Delta\phi\,(E_{\mathrm{T}}^{\mathrm{miss}}\,, j_2) < 0.3$ is selected as this is within the signal region. Figure 5.9 shows a comparison of the data and MC for $\Delta\phi\,(E_{\mathrm{T}}^{\mathrm{miss}}\,, j_2)$. The event yields for data and MC in this region are shown in Table 5.10 for each jet counting p_{T} threshold and for $p_{\mathrm{T}}\,(j_1) > 250\mathrm{GeV}$. A scale factor on the QCD background is derived using the Equation 5.13. Here, 'other backgrounds' are the sum of Z $\rightarrow \nu\,\bar{\nu}$ + jets, W + jets (corrected for the data driven estimate), $\mathrm{t\bar{t}}$, diboson, Z $\rightarrow \ell\ell$ + jets and single top. The uncertainty on this scale factor is due to 50% uncertainty on each of the 'other backgrounds' and the statistical uncertainty on number of events.

$$QCD_{s.f.} = \frac{\text{Data} - \text{Other backgrounds}}{\text{QCD MC}} \tag{5.13}$$

Averaging across jet counting thresholds, the scale factor at each inclusive $p_{\mathrm{T}}\,(\mathrm{j}_1)$ bin is found with associated error. Scale factors for each $p_{\mathrm{T}}\,(\mathrm{j}_1)$ bin are shown in Table 5.11. These are applied to the final QCD estimation, and error is combined with 50% uncertainty assigned to the QCD background from MC. A more detailed description of this study, including the breakdown of individual backgrounds can be found in Appendix **??**. We find a correction factor of 1.53 at $p_{\mathrm{T}}\,(\mathrm{j}_1) > 250\mathrm{GeV}$ is required, decreasing to 1.35 at $p_{\mathrm{T}}\,(\mathrm{j}_1) > 550\mathrm{GeV}$. This is greater than the factor from the dijet resonance analysis of 1.24, but this is a different region of phase space so it is not unexpected. More detail on the QCD estimation can be found in Appendix **??**.

Table 5.10: Event yields from MC and data at $p_{\mathrm{T}}\,(\mathrm{j}_1) > 250\mathrm{GeV}$ for different values of the p_{T} threshold used for jet counting in the QCD rich region $\Delta\phi\,(E_{\mathrm{T}}^{\mathrm{miss}}, j_2) < 0.3$. Relative uncertainty on a scale factor derived from the data is also shown.

Jet p_{T} (GeV)	Data	Total Bkg	QCD	Data/MC	$\mathrm{QCD}_{s.f}$	Uncertainty
> 20	21428	15987	10110	1.340	1.538	0.321
> 30	20568	15141	10089	1.358	1.538	0.325
> 40	19938	14543	10057	1.371	1.536	0.329
> 50	19307	13974	9930	1.382	1.537	0.335
> 60	18708	13522	9852	1.384	1.526	0.341
> 70	18110	12921	9603	1.402	1.540	0.347
> 80	17435	12485	9455	1.397	1.523	0.354

Table 5.11: QCD scale factor derived from QCD rich control region for each inclusive $p_{\mathrm{T}}\,(\mathrm{j}_1)$ bin with relative error

$p_{\mathrm{T}}\,(\mathrm{j}_1)$ (GeV)	$\mathrm{QCD}_{s.f.}$	Relative Error
250	1.534	0.336
300	1.490	0.336
350	1.465	0.341
400	1.428	0.350
450	1.402	0.359
500	1.365	0.369
550	1.347	0.377

To provide a further cross check that the QCD prediction is sensible, we check the agreement for $\Delta\phi\,(E_{\mathrm{T}}^{\mathrm{miss}}\,, j_3)$. Figure 5.10 shows the distribution for a jet counting threshold of 60 GeV and $p_{\mathrm{T}}\,(\mathrm{j}_1) > 250$GeV ; data agrees with MC within errors assigned.

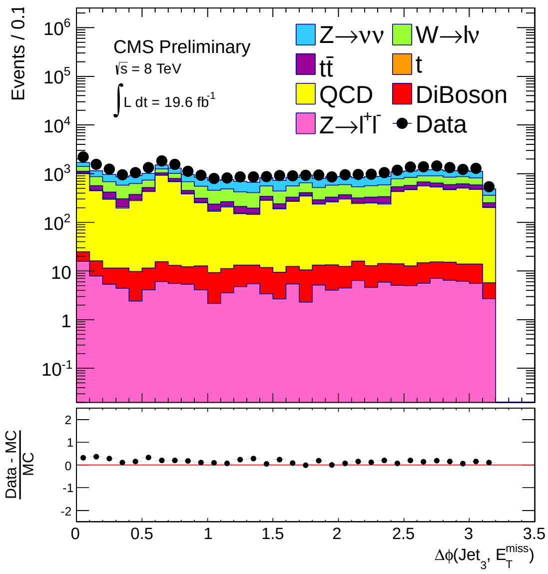

Figure 5.10: $\Delta\phi\,(\mathrm{E}_{\mathrm{T}}^{\mathrm{miss}}\,, \mathrm{j}_3)$, shown for a jet counting threshold of 60 GeV for $p_{\mathrm{T}}\,(\mathrm{j}_1) >$ 250GeV .

5.6.4 Diboson background estimation

The diboson background from WW, WZ and ZZ processes are estimated using MC with NLO cross sections. The W γ , Z $\rightarrow \nu\,\bar{\nu}\,\gamma$ and Z $\rightarrow \ell^+\ell^-\,\gamma$ backgrounds are absorbed into the data driven estimates of W + jets and Z $\rightarrow \nu\,\bar{\nu}$ + jets, and into the MC estimate of Z $\rightarrow \ell^+\ell^-$ + jets respectively. By absorbing W γ and Z $\rightarrow \nu\,\bar{\nu}\,\gamma$ into the main data driven backgrounds we reduce their errors, and in doing so reduce the total errors of the analysis. This is due to the 50% uncertainty assigned to all backgrounds estimated using MC, which contribute to the errors on W + jets and Z $\rightarrow \nu\,\bar{\nu}$ + jets (see Tables 5.9 and 5.6.) A summary of this, and the gain in using this inclusive method can be found in Appendix **??**.

Chapter 6

Results and Interpretation

"Physics, as we know it, will be over in six months."
— (1928) Max Born, 1882 – 1970

We show the results and interpretations of a search for events containing a single energetic jet and missing transverse momentum, using a data sample collected at 8 TeV by the CMS detector at the CERN LHC and corresponding to an integrated luminosity of 19.7 fb^{-1} . In this chapter, we show the results of the search described in Chapter 5 and interpret these in the context of SMS of SUSY in the third generation.

6.1 Signal MC simulation

Signal MC are Simplified Model Spectra (SMS) [148]. The use of SMS samples allows one to quantify the dependence of experimental limits in a more general way, compared to a Constrained Minimal Supersymmetric Scenario (CMSSM). Signal samples were generated using MadGraph 5 and showered with Pythia 6 with up to 2 partons, and the CMS detector response simulated using the CMSSW FastSim prescription. The MLM matching prescription is used to avoid double counting between the matrix element calculations and parton showering. Stop and sbottom production Cross sections are taken from the LHC SUSY Cross Section Working Group [149].

Stop signal simulation contains events where pair produced stops decay to a charm-neutralino pair with 100% branching fraction in the $(m_{\tilde{t}}, m_{\tilde{t}} - m_{\tilde{\chi}_1^0})$ mass plane from $m_{\tilde{t}}$ =100 GeV to 350 GeV in steps of 25 GeV , and $m_{\tilde{t}} - m_{\tilde{\chi}_1^0}$ = 10, 20, 30, 40, 60, and

Table 6.1: Summary of the SM background predictions and their corresponding uncertainties compared to the data.

$p_T\,(j_1)$ (GeV)	> 250	> 300	> 350	> 400	> 450	> 500	> 550
$Z \to \nu\bar{\nu}$ +jets	21209 ± 1115	10077 ± 592	4597 ± 324	2250 ± 197	1250 ± 137	663 ± 94	334 ± 65
W+jets	12328 ± 707	5939 ± 366	2690 ± 180	1246 ± 92	627 ± 52	301 ± 29	150 ± 18
$t\bar{t}$	602 ± 301	344 ± 172	178 ± 89	91 ± 46	48 ± 24	27 ± 14	18 ± 9.0
$Z \to \ell^+\ell^-$ +jets	127 ± 64	75 ± 38	40 ± 20	25 ± 13	17 ± 8.3	11 ± 5.6	7.4 ± 3.7
Single top	172 ± 86	97 ± 49	49 ± 24	21 ± 10	11 ± 5.7	5.2 ± 2.6	3.2 ± 1.6
QCD Multijets	786 ± 473	508 ± 306	304 ± 184	162 ± 99	80 ± 49	52 ± 32	28 ± 18
Diboson	639 ± 320	369 ± 184	206 ± 103	113 ± 56	64 ± 32	36 ± 18	21 ± 10
Total SM	35862 ± 1474	17409 ± 803	8064 ± 437	3907 ± 250	2098 ± 160	1096 ± 106	563 ± 71
Data	36582	17646	8119	3896	1898	1003	565

80 GeV. There are two additional points at $m_{\tilde{t}}$ =250, 275 GeV and $m_{\tilde{t}} - m_{\tilde{\chi}^0_1} = 5$ to probe the monojet limit towards stop-neutralino degeneracy. An additional set of stop events at $m_{\tilde{t}} = 200$ GeV and $m_{\tilde{t}} - m_{\tilde{\chi}^0_1} = 10$, 80 GeV were showered with up to 3 partons. The difference in signal acceptance between the 2-parton and 3-parton samples is found to be small; a table of acceptances for both samples can be found in Appendix **??**, which shows at $\Delta M = 10$ GeV, there is $< 1\%$ difference between the two showering methods.

An additional interpretation of pair produced sbottom quarks, which both decay to a bottom-neutralino pair with 100% branching fraction is also investigated. These SMS sbottom signal samples are produced in the same way as the stop samples; with a larger range of phase space covered. Here, we analyse $m_{\tilde{b}}$ =100 GeV to 450 GeV in steps of 25 GeV, and $m_{\tilde{\chi}^0_1} = 1$, 50, 100... GeV, for $m_{\tilde{\chi}^0_1} < m_{\tilde{b}}$. There are also points generated along the degeneracy line, at $m_{\tilde{b}} - m_{\tilde{\chi}^0_1} = 10$ GeV.

‘

6.2 Results

A summary of the predictions and corresponding uncertainties for all the SM backgrounds compared to the data are shown in Table 6.1. No significant deviation from the standard model is observed.

6.3 Systematic Uncertainties on Signal

The systematic uncertainties on the background event yields have been described in detail in the previous section. The dominant source of uncertainty on the signal is from uncertainty due to ISR modelling.

The selection of signal events (and therefore the signal acceptance) in this analysis relies on a high-p_{T} ISR jet, so the modelling of ISR must be reliable. The predicted and measured p_{T} spectra of recoiling systems against ISR jets is studied in [71] for Z + jets, $\mathrm{t\bar{t}}$ and other processes. The simulation is found to over predict the data by 20% for ISR jets with $p_{\mathrm{T}} > 250$ GeV . All signal acceptances have been weighted by a factor of 0.8 to correct for this difference between data and simulation. The uncertainty due to mismodelling of ISR jets is assigned 20% to account for this difference for the high p_{T} ISR jets involved.

Other sources of uncertainty considered are:

- jet energy scale (JES), emulated by shifting the jet 4-vector by an η and p_{T} dependent factor related to the response. After these corrections, the uncertainty due to the energy scale of these corrected jets on signal acceptance using a representative signal point was found to be 5%. In addition, a cross-check of the Jet and $E_{\mathrm{T}}^{\mathrm{miss}}$ energy scale for the monojet topology is performed using $\mathrm{Z} \rightarrow \mu^{+}\mu^{-}$ events. A detailed description of this cross-check can be found in Appendix **??**. The $E_{\mathrm{T}}^{\mathrm{miss}}$ scale derived using this method is found to be consistent with that from the recommended JES uncertainty.

- uncertainties on the parton density function. The PDF uncertainty for a representative signal sample was found to be less than 2%.

- the difference in acceptance that is obtained from generating signal events with up to 3 partons in MADGRAPH rather than 2 partons (< 4% for $p_{\mathrm{T}}(\mathrm{j}_1) > 500$ GeV).

The total uncertainty on the signal is taken to be a conservative 25%. The error on the luminosity measurement is 2.6% [150].

6.4 Interpretation and exclusion limits

To interpret the consistency of the observed number of events with the background expectation in the context of a model, and also to facilitate comparison with previous results, we set limits on the production cross section of top and bottom squarks as a function of the top and bottom squark mass and the LSP mass.

The CL_s method is used to estimate a 95% credible interval limit for a signal cross section in a counting experiment [**?**, 151]. Given the integrated luminosity, signal acceptance, background expectation and number of observed events (with associated uncertainties), the 95% CL upper limit on the signal cross section is set. The theory top squark production cross sections, equal to the bottom squark production cross sections, and $\pm 1\sigma_{\,\mathrm{theory}}$ bands are from a collaboration between the ATLAS, CMS and LPCC SUSY working groups. Theory uncertainties are dominated by PDF uncertainties and calculations are detailed in [149].

Expected limits are calculated as a function of $p_{\mathrm{T}}\,(\mathrm{j}_1)$ for every $(m_{\tilde{\mathrm{t}}}, m_{\tilde{\chi}_1^0})$ or $(m_{\tilde{\mathrm{b}}}, m_{\tilde{\chi}_1^0})$ using the background expectation in each signal region. The signal region where the best (i.e. lowest) expected limit is found is selected as the optimal region in which to set limits for that mass point. A fluctuation in the number of $Z(\mu\,\mu)$ events at $p_{\mathrm{T}}\,(\mathrm{j}_1) > 450$ GeV means we have discounted this bin from the limit setting procedure in order to smooth the curves out.

The expected limits for each mass point in the stop, LSP mass plane at every $p_{\mathrm{T}}\,(\mathrm{j}_1)$ bin can be found in Figure 6.1. The temperature plots in Figure 6.2 show the best expected limit across the phase space range for both stop, LSP mass planes and sbottom, LSP mass planes. Figure 6.3 shows the expected and observed limits on the stop production cross section for the optimised $p_{\mathrm{T}}\,(\mathrm{j}_1)$ bin, as a function of the top squark mass for mass differences between the top squark and LSP $(m_{\tilde{\mathrm{t}}} - m_{\tilde{\chi}_1^0})$ of $10, 20, 30, 40, 60$ and 80 GeV . Figure 6.4 shows the optimised expected and observed limits for various bottom squark masses as a function of mass difference, $m_{\tilde{\mathrm{b}}} - m_{\tilde{\chi}_1^0}$. Figure 6.5 shows 95% CL expected $\pm 1\sigma_{\,\mathrm{exp}}$ and observed limits $\pm 1\sigma_{\,\mathrm{theory}}$ on the top squark production cross section as a function of top squark mass and LSP mass, and top squark mass and ΔM. The observed and expected limits on the stop production cross section are also tabulated in Tables 6.2 and 6.3.

Figure 6.6 shows the 95% CL expected $\pm 1\sigma_{\,\mathrm{exp}}$ and observed limits $\pm 1\sigma_{\,\mathrm{theory}}$ on the bottom squark production cross section as a function of bottom squark mass and

Table 6.2: The expected limits on the production cross section of stops for different values of $m_{\tilde{t}} - m_{\tilde{\chi}_1^0}$. Also shown are the $+1\sigma$ expected limits in superscript, and the -1σ expected limits in subscript.

$p_{\mathrm{T}}\,(\mathrm{j}_1)$ (GeV)	> 250	> 300	> 350	> 400	> 450	> 500	$>$
$m_{\tilde{t}} - m_{\tilde{\chi}_1^0} = 10$	$82.98 \pm^{115.7}_{57.15}$	$37.63 \pm^{53.28}_{28.11}$	$23.89 \pm^{33.84}_{17.85}$	$15.48 \pm^{21.93}_{11.56}$	$11.02 \pm^{17.5}_{8.489}$	$8.128 \pm^{12.9}_{6.259}$	6.14
$m_{\tilde{t}} - m_{\tilde{\chi}_1^0} = 20$	$129 \pm^{178.2}_{88.96}$	$57.03 \pm^{81.5}_{39.17}$	$32.37 \pm^{46.33}_{22.24}$	$20.32 \pm^{28.99}_{13.96}$	$14.1 \pm^{20.16}_{9.686}$	$10.59 \pm^{15.01}_{7.916}$	7.65
$m_{\tilde{t}} - m_{\tilde{\chi}_1^0} = 30$	$210.1 \pm^{298.7}_{145}$	$89.51 \pm^{128.1}_{61.5}$	$51.35 \pm^{72.03}_{35.58}$	$29.23 \pm^{41.85}_{20.08}$	$19.03 \pm^{26.95}_{14.22}$	$14.7 \pm^{20.82}_{10.98}$	10.6
$m_{\tilde{t}} - m_{\tilde{\chi}_1^0} = 40$	$259.8 \pm^{357.1}_{176.1}$	$122 \pm^{174.5}_{83.85}$	$66.71 \pm^{95.04}_{46.13}$	$39.01 \pm^{55.84}_{26.8}$	$26.05 \pm^{37.15}_{17.9}$	$18.67 \pm^{26.73}_{12.83}$	13.3
$m_{\tilde{t}} - m_{\tilde{\chi}_1^0} = 60$	$312.9 \pm^{447.9}_{214.6}$	$156.1 \pm^{218.8}_{106.8}$	$98.48 \pm^{138.1}_{68.23}$	$54.47 \pm^{78.02}_{37.43}$	$35.69 \pm^{51.11}_{24.52}$	$27.33 \pm^{39.08}_{18.78}$	20.2
$m_{\tilde{t}} - m_{\tilde{\chi}_1^0} = 80$	$346 \pm^{482.5}_{240.3}$	$175.4 \pm^{247.4}_{120}$	$99.73 \pm^{142}_{69.04}$	$62.38 \pm^{89.35}_{42.86}$	$45.92 \pm^{65.77}_{31.55}$	$32.57 \pm^{46.64}_{22.37}$	26.

LSP mass. The region of compressed phase space from approximately $m_{\tilde{b}} = 275$ GeV, $m_{\tilde{b}} - m_{\tilde{\chi}_1^0} = 0$ GeV to $m_{\tilde{b}} = 165$ GeV, $m_{\tilde{b}} - m_{\tilde{\chi}_1^0} = 85$ GeV is excluded at 95% CL. This limit is from 'monojet'-like events, that are boosted such that an ISR jet is radiated and balances the p_{T} of LSPs leaving the detector (giving rise to $E_{\mathrm{T}}^{\mathrm{miss}}$). The region of phase space from approximately $m_{\tilde{b}} = 165$ GeV, $m_{\tilde{\chi}_1^0} = 40$ GeV to $m_{\tilde{b}} = 275$ GeV, $m_{\tilde{\chi}_1^0} = 0$ GeV is also excluded. Here, dijet events dominate; the $\mathrm{N}_{jet} \leq 2$ requirement allows for events in which two jets, originating from the bottom quark decay products, passing the event selection. At least of these b-jets must be very energetic, above the optimal p_{T} threshold of that point of phase space. If there are two jets in the event, either the other b-jet or an ISR jet, it must be above 60 GeV. Again, the $E_{\mathrm{T}}^{\mathrm{miss}}$ in these events arises from boosted LSPs leaving the detector, only now they are balanced by the momenta of the b-jets. Figure 6.6 also shows that bottom squarks are excluded for $m_{\tilde{b}} < 165$ GeV for all LSP masses.

Table 6.3: The observed limits on the production cross section of stops for different values of $m_{\tilde{t}} - m_{\tilde{\chi}_1^0}$.

$p_{\mathrm{T}}\,(\mathrm{j}_1)$ (GeV)	> 250	> 300	> 350	> 400	> 450	> 500	> 550
$m_{\tilde{t}} - m_{\tilde{\chi}_1^0} = 10$	87.75	37.53	23.83	15.44	8.843	6.52	4.931
$m_{\tilde{t}} - m_{\tilde{\chi}_1^0} = 20$	138.2	58.6	33.27	20.89	14.49	10.57	6.13
$m_{\tilde{t}} - m_{\tilde{\chi}_1^0} = 30$	225.2	92.03	54.86	30.05	18.99	14.66	10.59
$m_{\tilde{t}} - m_{\tilde{\chi}_1^0} = 40$	275.7	125.5	71.48	40.1	26.78	19.19	10.72
$m_{\tilde{t}} - m_{\tilde{\chi}_1^0} = 60$	337	166.6	105.2	56.01	36.69	28.1	20.22
$m_{\tilde{t}} - m_{\tilde{\chi}_1^0} = 80$	372.8	187.3	106.6	64.14	47.22	33.48	26.63

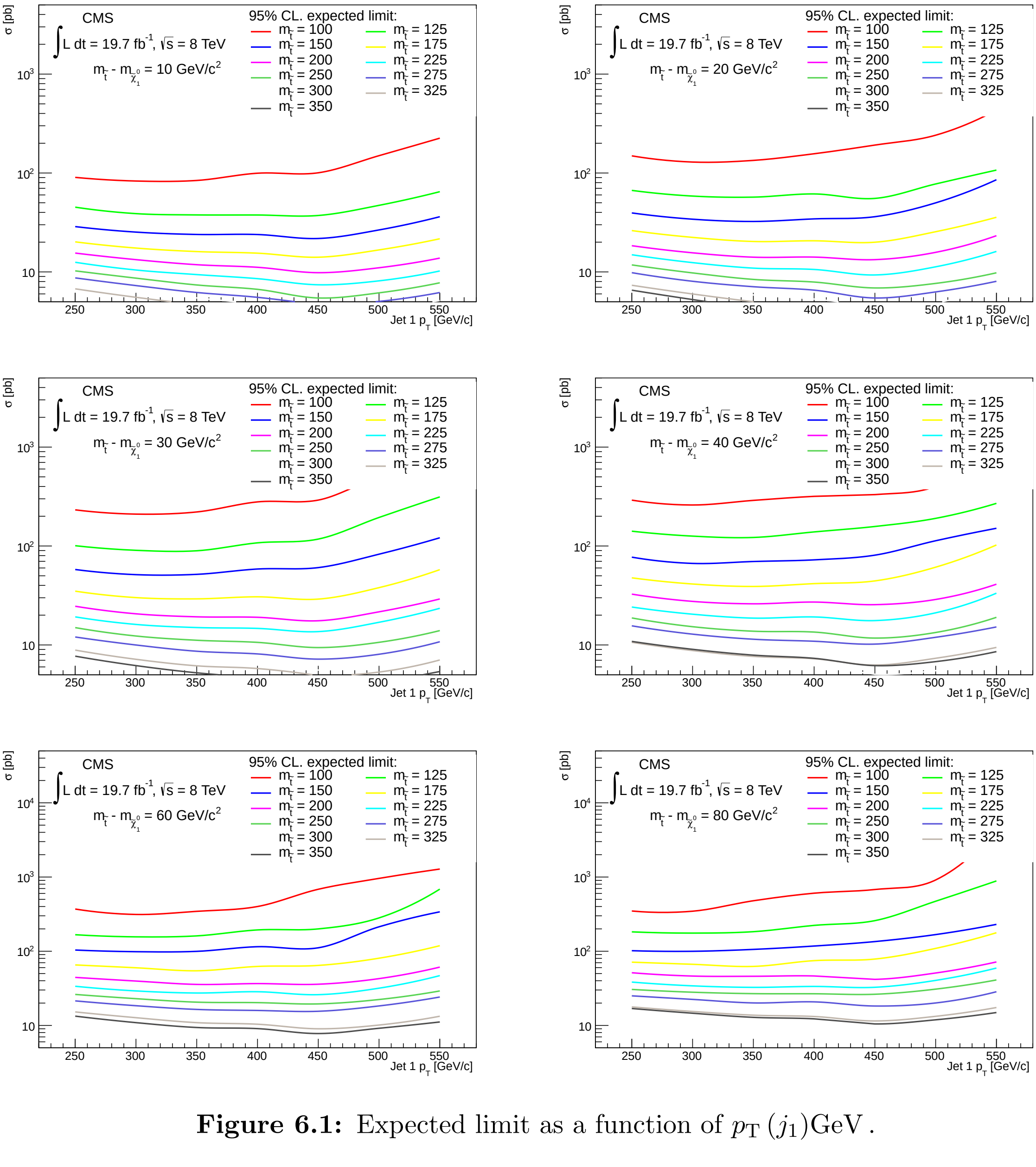

Figure 6.1: Expected limit as a function of $p_T\,(j_1)$GeV .

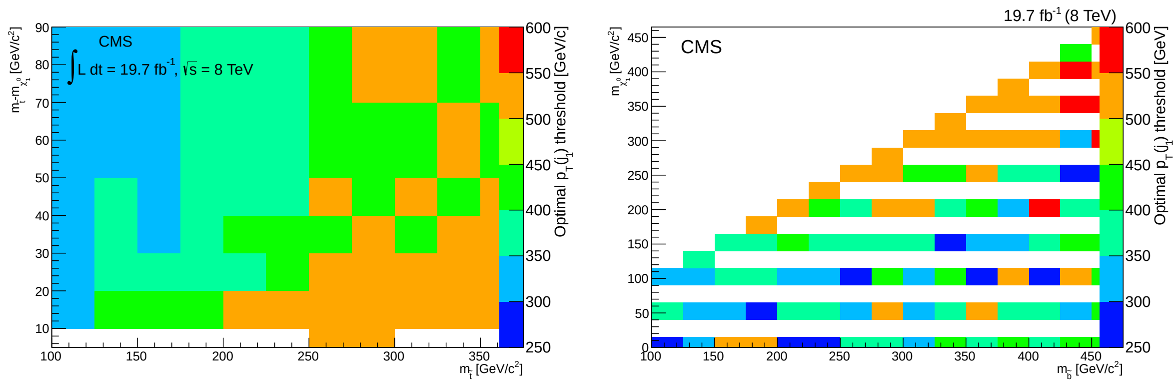

Figure 6.2: The temperature plot shows the $p_{\mathrm{T}}\left(\mathrm{j}_1\right)$ threshold at which the best expected limit is found, as a function of $m_{\tilde{\mathrm{t}}}$, and $m_{\tilde{\mathrm{t}}} - m_{\tilde{\chi}^0_1}$ (left) and $m_{\tilde{\mathrm{b}}}$ and $m_{\tilde{\chi}^0_1}$ (right).

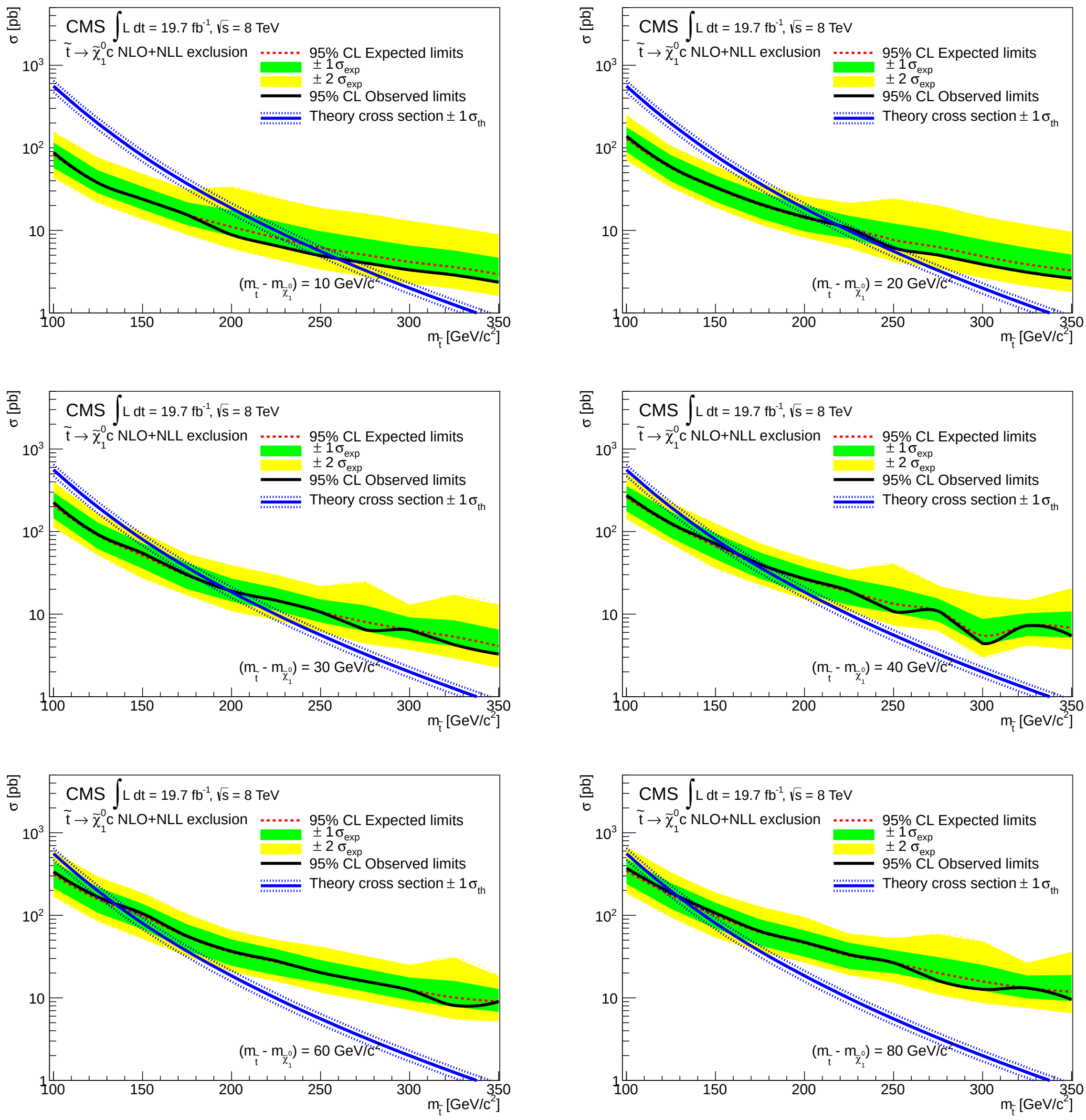

Figure 6.3: Optimised observed and expected limits on stop production cross section as a function of the stop mass for $m_{\tilde{t}} - m_{\tilde{\chi}^0_1} = 10, 20, 30, 40, 60$ and 80 GeV .

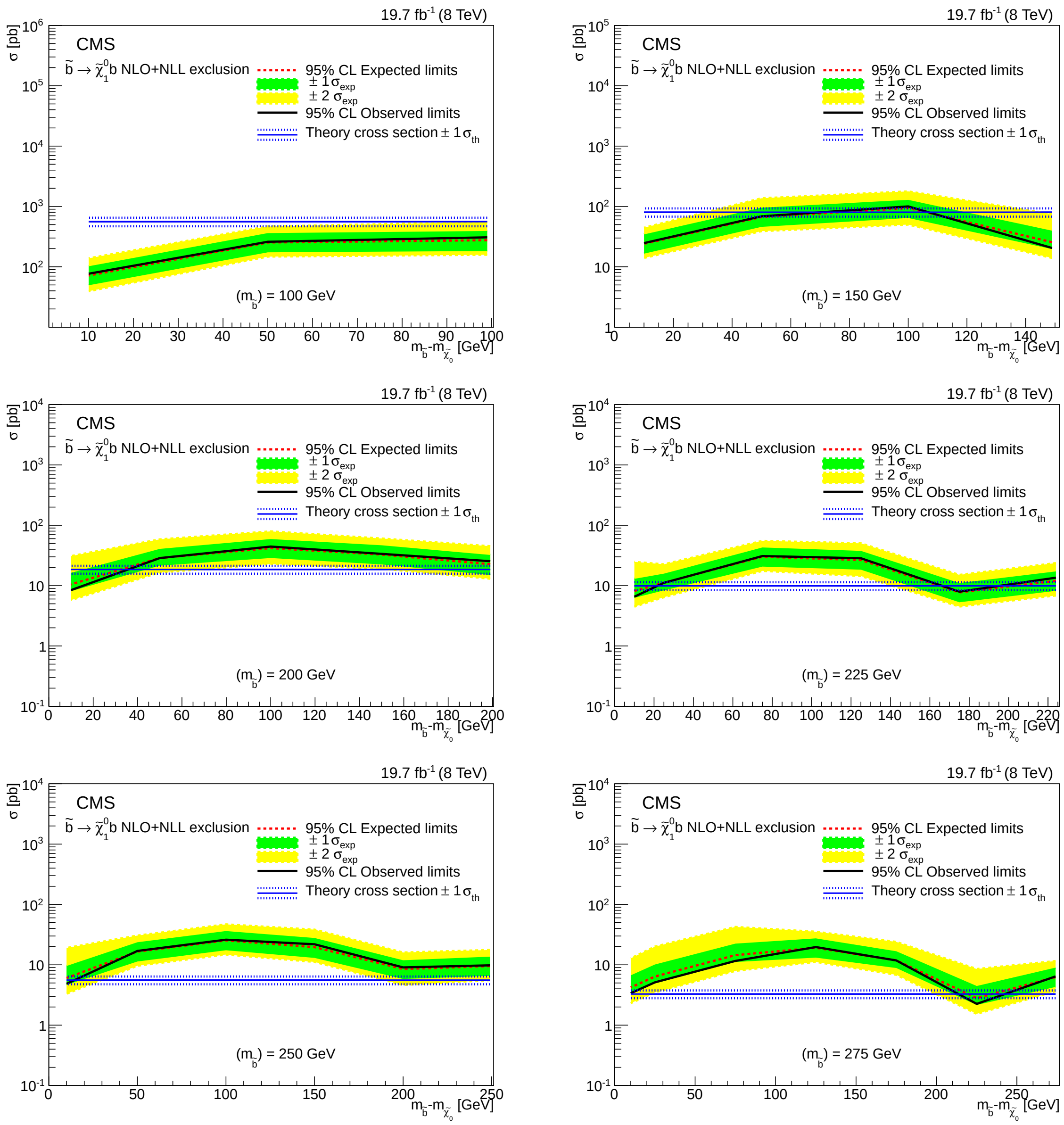

Figure 6.4: Optimised observed and expected limits on sbottom production cross section as a function of the mass difference $m_{\tilde{b}} - m_{\tilde{\chi}^0_1}$, shown for $m_{\tilde{b}} = 100, 150, 200, 225, 250$ and 275 GeV. The limits at low mass difference are due to monojet events, where an event with a radiated ISR jet passes the event selection. At large mass differences, we become sensitive to dijet events; events in which two b-jets from both bottom squark decays pass the event selection.

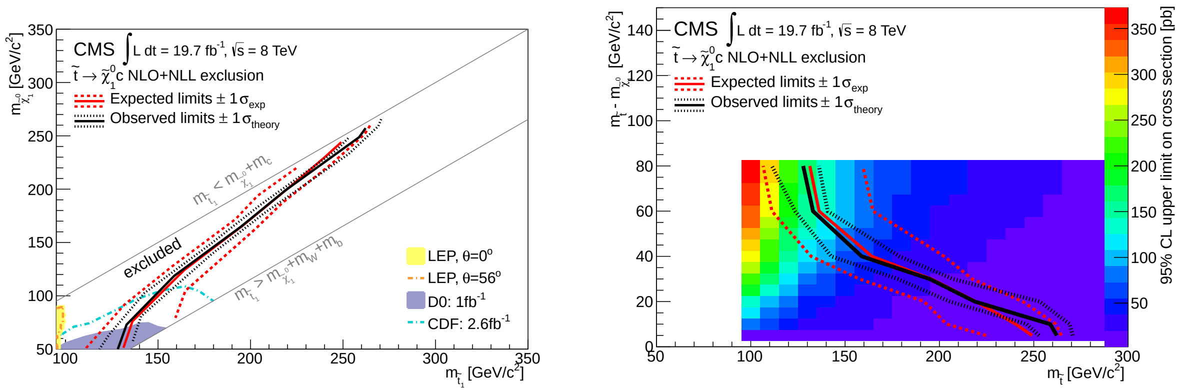

Figure 6.5: Observed and expected limits on stop production cross section as a function of the stop mass and LSP mass (left) and as a function of the stop mass and $m_{\widetilde{t}} - m_{\widetilde{\chi}_1^0}$ (right).

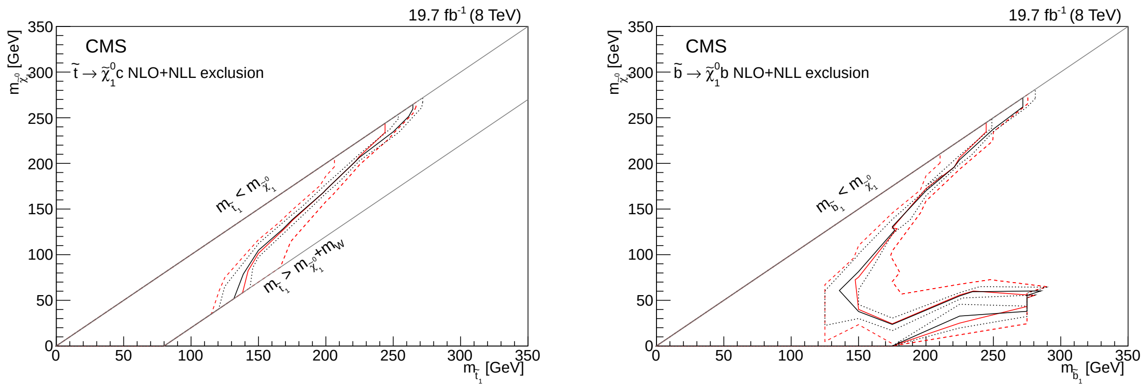

Figure 6.6: Observed and expected limits on top (left) and bottom (right) squark pair production cross section as a function of the top and bottom squark mass and LSP mass. The top squark limit is the same as the above, only formatted to allow easy comparison between the two limits, which are very similar in the compressed region, as is expected.

Chapter 7

Searching for Compressed SUSY with monojet events in parked data

Preselection	
Signal region	Single muon control region
$E_{\mathrm{T}}^{\mathrm{miss}} > 190$ GeV	$E_{\mathrm{T}}^{\mathrm{miss}} > 190$ GeV
$p_{\mathrm{T}}(\mathrm{j}_1) > 100$ GeV	$p_{\mathrm{T}}(\mathrm{j}_1) > 100$ GeV
$N_{\mathrm{jets}} \leq 2$	$N_{\mathrm{jets}} \leq 2$
$\Delta\phi(\mathrm{j}_1, \mathrm{j}_2) < 2.5$	$\Delta\phi(\mathrm{j}_1, \mathrm{j}_2) < 2.5$
Veto muon > 10 GeV	$1\ \mu$, $50 < m_T < 100$
Veto electron > 10 GeV	Veto electron > 10 GeV
Veto had tau (HPS) > 20 GeV	Veto had tau (HPS) > 20 GeV
$E_{\mathrm{T}}^{\mathrm{miss}} > 200$ GeV	$E_{\mathrm{T}}^{\mathrm{miss}} > 200$ GeV
$E_{\mathrm{T}}^{\mathrm{miss}} > 250$ GeV	$E_{\mathrm{T}}^{\mathrm{miss}} > 250$ GeV
$E_{\mathrm{T}}^{\mathrm{miss}} > 300$ GeV	$E_{\mathrm{T}}^{\mathrm{miss}} > 300$ GeV
$E_{\mathrm{T}}^{\mathrm{miss}} > 350$ GeV	$E_{\mathrm{T}}^{\mathrm{miss}} > 350$ GeV
$E_{\mathrm{T}}^{\mathrm{miss}} > 400$ GeV	$E_{\mathrm{T}}^{\mathrm{miss}} > 400$ GeV
$E_{\mathrm{T}}^{\mathrm{miss}} > 450$ GeV	$E_{\mathrm{T}}^{\mathrm{miss}} > 450$ GeV
$E_{\mathrm{T}}^{\mathrm{miss}} > 500$ GeV	$E_{\mathrm{T}}^{\mathrm{miss}} > 500$ GeV
$E_{\mathrm{T}}^{\mathrm{miss}} > 550$ GeV	$E_{\mathrm{T}}^{\mathrm{miss}} > 550$ GeV

Table 7.1: Initial cuts of the signal regions (left) and the single muon control region (right) for the parked data T2cc analysis.

Bibliography

[1] CMS, LHCb Collaboration, "Observation of the rare $B^0_s \to \mu^+\mu^-$ decay from the combined analysis of CMS and LHCb data", arXiv:1411.4413.

[2] CMS Collaboration, "Summaries of CMS cross section measurements". https://twiki.cern.ch/twiki/bin/view/CMSPublic/PhysicsResultsCombined. Accessed: 2014-12-20.

[3] S. Weinberg, "A Model of Leptons", *Phys. Rev. Lett.* **19** (Nov, 1967) 1264–1266, doi:10.1103/PhysRevLett.19.1264.

[4] S. Glashow, "Partial Symmetries of Weak Interactions", *Nucl.Phys.* **22** (1961) doi:10.1016/0029-5582(61)90469-2.

[5] A. Salam, "Weak and Electromagnetic Interactions", *Conf.Proc.* **C680519** (1968).

[6] G. Hooft, "Renormalizable Lagrangians for massive Yang-Mills fields", *Nuclear Physics B* **35** (1971) doi:http://dx.doi.org/10.1016/0550-3213(71)90139-8.

[7] P. Higgs, "Broken Symmetries and the Masses of Gauge Bosons", *Phys. Rev. Lett.* **13** (Oct, 1964) 508–509, doi:10.1103/PhysRevLett.13.508.

[8] ATLAS Collaboration, "Observation of a new particle in the search for the Standard Model Higgs boson with the ATLAS detector at the LHC", *Phys. Lett. B* **716** (2012) 1, doi:10.1016/j.physletb.2012.08.020, arXiv:1207.7214.

[9] CMS Collaboration, "Observation of a new boson at a mass of 125 GeV with the CMS experiment at the LHC", *Phys. Lett. B* **716** (2012) 30, doi:10.1016/j.physletb.2012.08.021, arXiv:1207.7235.

[10] A. D. M. F. Halzen, "Quarks and Leptons: An Introductory Course in Modern Particle Physics". John Wiley and Sons, Philadelphia, 1984.

[11] Particle Data Group Collaboration, "Review of Particle Physics", *Chin. Phys. C* **38** (2014) 090001, doi:10.1088/1674-1137/38/9/090001.

[12] Y. Fukuda, T. Hayakawa, et al., "Measurements of the Solar Neutrino Flux from Super-Kamiokande's First 300 Days", *Phys. Rev. Lett.* **81** (Aug, 1998) 1158–1162, doi:10.1103/PhysRevLett.81.1158.

[13] J. J. Thomson, "XL. Cathode Rays", *Philosophical Magazine Series 5* **44** (1897), no. 269, 293–316, doi:10.1080/14786449708621070, arXiv:http://dx.doi.org/10.1080/14786449708621070.

[14] W. Pauli, "Letter to a physics meeting in Tbingen". http://microboone-docdb.fnal.gov/cgi-bin/RetrieveFile?docid=953;filename=pauli%20letter1930.pdf, 1930. Accessed: 2015-01-30, German original and English translation.

[15] F. Reines and C. L. Cowan, "The Neutrino", *Nature* **178** (09, 1956) 446–449.

[16] C. D. Anderson and S. H. Neddermeyer, "Cloud Chamber Observations of Cosmic Rays at 4300 Meters Elevation and Near Sea-Level", *Phys. Rev.* **50** (Aug, 1936) 263–271, doi:10.1103/PhysRev.50.263.

[17] J. C. Street and E. C. Stevenson, "New Evidence for the Existence of a Particle of Mass Intermediate Between the Proton and Electron", *Phys. Rev.* **52** (Nov, 1937) 1003–1004, doi:10.1103/PhysRev.52.1003.

[18] G. Danby, J.-M. Gaillard, K. Goulianos et al., "Observation of High-Energy Neutrino Reactions and the Existence of Two Kinds of Neutrinos", *Phys. Rev. Lett.* **9** (Jul, 1962) 36–44, doi:10.1103/PhysRevLett.9.36.

[19] M. Gell-Mann, "A Schematic Model of Baryons and Mesons", *Phys. Lett.* **8** (1964) 214–215, doi:10.1016/S0031-9163(64)92001-3.

[20] G. Zweig, "An SU(3) model for strong interaction symmetry and its breaking. Version 2",.

[21] E. D. Bloom, D. H. Coward, H. DeStaebler et al., "High-Energy Inelastic $e-p$ Scattering at 6° and 10°", *Phys. Rev. Lett.* **23** (Oct, 1969) 930, doi:10.1103/PhysRevLett.23.930.

[22] M. Breidenbach, J. I. Friedman, H. W. Kendall et al., "Observed Behavior of Highly Inelastic Electron-Proton Scattering", *Phys. Rev. Lett.* **23** (Oct, 1969)

935, doi:10.1103/PhysRevLett.23.935.

[23] S. Glashow, J. Iliopoulos, and L. Maiani, "Weak Interactions with Lepton-Hadron Symmetry", *Phys. Rev. D* **2** (Oct, 1970) 1285–1292, doi:10.1103/PhysRevD.2.1285.

[24] J. J. Aubert, U. Becker, P. J. Biggs et al., "Experimental Observation of a Heavy Particle J", *Phys. Rev. Lett.* **33** (Dec, 1974) 1404–1406, doi:10.1103/PhysRevLett.33.1404.

[25] J. E. Augustin, A. M. Boyarski, M. Breidenbach et al., "Discovery of a Narrow Resonance in e^+e^- Annihilation", *Phys. Rev. Lett.* **33** (Dec, 1974) 1406, doi:10.1103/PhysRevLett.33.1406.

[26] M. L. Perl, G. S. Abrams, A. M. Boyarski et al., "Evidence for Anomalous Lepton Production in $e^+ - e^-$ Annihilation", *Phys. Rev. Lett.* **35** (Dec, 1975) 1489–1492, doi:10.1103/PhysRevLett.35.1489.

[27] DONUT Collaboration, "Observation of tau neutrino interactions", *Phys. Lett. B* **504** (2001) 218, doi:10.1016/S0370-2693(01)00307-0, arXiv:hep-ex/0012035.

[28] M. Kobayashi and T. Maskawa, "CP-Violation in the Renormalizable Theory of Weak Interaction", *Progress of Theoretical Physics* **49** (1973), no. 2, 652–657, doi:10.1143/PTP.49.652, arXiv:http://ptp.oxfordjournals.org/content/49/2/652.full.pdf+html.

[29] S. W. Herb, D. C. Hom, L. M. Lederman et al., "Observation of a Dimuon Resonance at 9.5 GeV in 400-GeV Proton-Nucleus Collisions", *Phys. Rev. Lett.* **39** (Aug, 1977) 252–255, doi:10.1103/PhysRevLett.39.252.

[30] CDF Collaboration, "Observation of Top Quark Production in $\overline{p}p$ Collisions with the Collider Detector at Fermilab", *Phys. Rev. Lett.* **74** (Apr, 1995) 2626–2631, doi:10.1103/PhysRevLett.74.2626.

[31] D0 Collaboration, "Search for High Mass Top Quark Production in $p\overline{p}$ Collisions at $\sqrt{s} =$ 1.8 TeV", *Phys. Rev. Lett.* **74** (Mar, 1995) 2422, doi:10.1103/PhysRevLett.74.2422.

[32] UA1 Collaboration, "Experimental observation of isolated large transverse energy electrons with associated missing energy at s=540 GeV", *Phys. Lett. B* **122**

(1983), no. 1, 103, doi:http://dx.doi.org/10.1016/0370-2693(83)91177-2.

[33] UA2 Collaboration, "Observation of single isolated electrons of high transverse momentum in events with missing transverse energy at the CERN pp collider", *Phys. Lett. B* **122** (1983), no. 56, 476, doi:http://dx.doi.org/10.1016/0370-2693(83)91605-2.

[34] UA1 Collaboration, "Experimental observation of lepton pairs of invariant mass around 95 GeV at the CERN SPS collider", *Phys. Lett. B* **126** (1983), no. 5, 398, doi:http://dx.doi.org/10.1016/0370-2693(83)90188-0.

[35] UA2 Collaboration, "Evidence for $Z^0 \to e^+e$ at the CERN pp collider", *Phys. Lett. B* **129** (1983), no. 12, 130, doi:http://dx.doi.org/10.1016/0370-2693(83)90744-X.

[36] TASSO Collaboration, "Evidence for planar events in e+e annihilation at high energies", *Phys. Lett. B* **86** (1979), no. 2, 243, doi:http://dx.doi.org/10.1016/0370-2693(79)90830-X.

[37] MARK–J Collaboration, "Discovery of Three-Jet Events and a Test of Quantum Chromodynamics at PETRA", *Phys. Rev. Lett.* **43** (Sep, 1979) 830, doi:10.1103/PhysRevLett.43.830.

[38] E. Noether, "Invariante Variationsprobleme", *Nachrichten von der Gesellschaft der Wissenschaften zu Gttingen, Mathematisch-Physikalische Klasse* **1918** (1918) 235–257.

[39] N. Cabibbo, "Unitary Symmetry and Leptonic Decays", *Phys. Rev. Lett.* **10** (Jun, 1963) 531, doi:10.1103/PhysRevLett.10.531.

[40] SNO Collaboration, "Measurement of the Rate of $\nu_e + d \to p + p + e^-$ Interactions Produced by ^8B Solar Neutrinos at the Sudbury Neutrino Observatory", *Phys. Rev. Lett.* **87** (Jul, 2001) 071301, doi:10.1103/PhysRevLett.87.071301.

[41] E. Corbelli and P. Salucci, "The extended rotation curve and the dark matter halo of M33", *MNRAS* **311** (2000), no. 2, 441, doi:10.1046/j.1365-8711.2000.03075.x.

[42] F. W. Dyson, A. S. Eddington, and C. Davidson, "A Determination of the Deflection of Light by the Sun's Gravitational Field, from Observations Made at the Total Eclipse of May 29, 1919", *Phil. Trans. A* **220** (1920), no. 571-581, 291,

doi:10.1098/rsta.1920.0009.

[43] R. Massey, T. Kitching, and J. Richard, “The dark matter of gravitational lensing”, *Reports on Progress in Physics* **73** (August, 2010) 086901, doi:10.1088/0034-4885/73/8/086901, arXiv:1001.1739.

[44] Planck Collaboration Collaboration, “Planck 2013 results. XVI. Cosmological parameters”, *Astron. Astrophys.* **571** (2014) A16, doi:10.1051/0004-6361/201321591, arXiv:1303.5076.

[45] D. Clowe, M. Bradac, A. H. Gonzalez et al., “A direct empirical proof of the existence of dark matter”, *Astrophys. J.* **648** (2006) L109, doi:10.1086/508162, arXiv:astro-ph/0608407.

[46] M. Davis, G. Efstathiou, C. S. Frenk et al., “The evolution of large-scale structure in a universe dominated by cold dark matter”, *Astrophys. J* **292** (1985) 371, doi:10.1086/163168.

[47] L. Goodenough and D. Hooper, “Possible Evidence For Dark Matter Annihilation In The Inner Milky Way From The Fermi Gamma Ray Space Telescope”, arXiv:0910.2998.

[48] ALEPH Collaboration, CDF Collaboration, D0 Collaboration, DELPHI Collaboration, L3 Collaboration, OPAL Collaboration, SLD Collaboration, LEP Electroweak Working Group, Tevatron Electroweak Working Group, SLD Electroweak and Heavy Flavour Groups Collaboration, “Precision Electroweak Measurements and Constraints on the Standard Model”, arXiv:1012.2367.

[49] M. Baak, M. Goebel, J. Haller et al., “The Electroweak Fit of the Standard Model after the Discovery of a New Boson at the LHC”, *Eur. Phys. J. C* **72** (2012) 2205, doi:10.1140/epjc/s10052-012-2205-9, arXiv:1209.2716.

[50] CMS Collaboration, “Precise determination of the mass of the Higgs boson and tests of compatibility of its couplings with the standard model predictions using proton collisions at 7 and 8 TeV”, arXiv:1412.8662.

[51] ATLAS Collaboration, “Measurement of the Higgs boson mass from the $H \to \gamma\gamma$ and $H \to ZZ^* \to 4\ell$ channels with the ATLAS detector using 25 fb^{-1} of pp collision data”, *Phys. Rev. D* **90** (2014) 052004, doi:10.1103/PhysRevD.90.052004, arXiv:1406.3827.

[52] Y. Golfand and E. Likhtman, "Extension of the Algebra of Poincare Group Generators and Violation of p Invariance", *JETP Lett.* **13** (1971) 323–326.

[53] S. P. Martin, "A Supersymmetry primer", *Adv. Ser. Direct. High Energy Phys.* **21** (2010) 1–153, doi:10.1142/9789814307505_0001, arXiv:hep-ph/9709356.

[54] N. Arkani-Hamed, S. Dimopoulos, and G. Dvali, "The hierarchy problem and new dimensions at a millimeter", *Phys. Lett. B* **429** (1998), no. 34, 263 – 272, doi:http://dx.doi.org/10.1016/S0370-2693(98)00466-3.

[55] R. N. Mohapatra and G. Senjanović, "Neutrino Mass and Spontaneous Parity Nonconservation", *Phys. Rev. Lett.* **44** (Apr, 1980) 912–915, doi:10.1103/PhysRevLett.44.912.

[56] J. Schechter and J. W. F. Valle, "Neutrino masses in SU(2) $\otimes$ U(1) theories", *Phys. Rev. D* **22** (November, 1980) 2227–2235, doi:10.1103/PhysRevD.22.2227.

[57] M. Schmaltz and D. Tucker-Smith, "Little Higgs review", *Ann. Rev. Nucl. Part. Sci.* **55** (2005) 229–270, doi:10.1146/annurev.nucl.55.090704.151502, arXiv:hep-ph/0502182.

[58] S. Coleman and J. Mandula, "All Possible Symmetries of the S Matrix", *Phys. Rev.* **159** (Jul, 1967) 1251, doi:10.1103/PhysRev.159.1251.

[59] Y. Golfand and E. Likhtman, "Extension of the Algebra of Poincare Group Generators and Violation of p Invariance", *JETP Lett.* **13** (1971) 323.

[60] S. Dawson, "SUSY and such", *NATO Sci.Ser.B* **365** (1997) 33–80, doi:10.1007/978-1-4615-5963-4_2, arXiv:hep-ph/9612229.

[61] S. Dimopoulos, S. Raby, and F. Wilczek, "Supersymmetry and the Scale of Unification", *Phys. Rev. D* **24** (1981) 1681–1683, doi:10.1103/PhysRevD.24.1681.

[62] D. Kazakov, "Beyond the standard model: In search of supersymmetry", (2000). arXiv:hep-ph/0012288.

[63] D. Chung, L. Everett, G. Kane et al., "The Soft supersymmetry breaking Lagrangian: Theory and applications", *Phys. Rept.* **407** (2005) 1–203, doi:10.1016/j.physrep.2004.08.032, arXiv:hep-ph/0312378.

[64] M. Papucci, J. T. Ruderman, and A. Weiler, "Natural SUSY Endures", *JHEP* **1209** (2012) 035, doi:10.1007/JHEP09(2012)035, arXiv:1110.6926.

[65] C. Brust, A. Katz, S. Lawrence et al., "SUSY, the Third Generation and the LHC", *JHEP* **1203** (2012) 103, doi:10.1007/JHEP03(2012)103, arXiv:1110.6670.

[66] CMS Collaboration, "Search for new physics in events with same-sign dileptons and b jets in pp collisions at $\sqrt{s} = 8$ TeV", *JHEP* **1303** (2013) 037, doi:10.1007/JHEP03(2013)037,10.1007/JHEP07(2013)041, arXiv:1212.6194.

[67] CMS Collaboration, "Search for gluino mediated bottom- and top-squark production in multijet final states in pp collisions at 8 TeV", *Phys. Lett. B* **725** (2013) 243–270, doi:10.1016/j.physletb.2013.06.058, arXiv:1305.2390.

[68] CMS Collaboration, "Search for new physics in the multijet and missing transverse momentum final state in proton-proton collisions at $\sqrt{s}$= 8 TeV", *JHEP* **1406** (2014) 055, doi:10.1007/JHEP06(2014)055, arXiv:1402.4770.

[69] CMS Collaboration, "Search for supersymmetry in pp collisions at $\sqrt{s}$=8 TeV in events with a single lepton, large jet multiplicity, and multiple b jets", *Phys. Lett. B* **733** (2014) 328–353, doi:10.1016/j.physletb.2014.04.023, arXiv:1311.4937.

[70] CMS Collaboration, "Search for anomalous production of events with three or more leptons in pp collisions at $\sqrt(s) = 8$ TeV", *Phys. Rev. D* **90** (2014), no. 3, 032006, doi:10.1103/PhysRevD.90.032006, arXiv:1404.5801.

[71] CMS Collaboration, "Search for top-squark pair production in the single-lepton final state in pp collisions at $\sqrt{s} = 8$ TeV", *Eur. Phys. J. C* **73** (2013), no. 12, 2677, doi:10.1140/epjc/s10052-013-2677-2, arXiv:1308.1586.

[72] CMS Collaboration, "Search for top squark and higgsino production using diphoton Higgs boson decays", *Phys. Rev. Lett.* **112** (2014) 161802, doi:10.1103/PhysRevLett.112.161802, arXiv:1312.3310.

[73] CMS Collaboration, "Search for top-squark pairs decaying into Higgs or Z bosons in pp collisions at $\sqrt{s}$=8 TeV", *Phys. Lett. B* **736** (2014) 371–397, doi:10.1016/j.physletb.2014.07.053, arXiv:1405.3886.

[74] CMS Collaboration, "Searches for electroweak production of charginos,

neutralinos, and sleptons decaying to leptons and W, Z, and Higgs bosons in pp collisions at 8 TeV", *Eur. Phys. J. C* **74** (2014), no. 9, 3036, doi:10.1140/epjc/s10052-014-3036-7, arXiv:1405.7570.

[75] CMS Collaboration, "Search for supersymmetry with razor variables in pp collisions at $\sqrt{s}$=7 TeV", *Phys. Rev. D* **90** (2014), no. 11, 112001, doi:10.1103/PhysRevD.90.112001, arXiv:1405.3961.

[76] CMS Collaboration, "Search for supersymmetry in hadronic final states with missing transverse energy using the variables α_T and b-quark multiplicity in pp collisions at $\sqrt{s} = 8$ TeV", *Eur. Phys. J. C* **73** (2013), no. 9, 2568, doi:10.1140/epjc/s10052-013-2568-6, arXiv:1303.2985.

[77] CMS Collaboration, "Search for supersymmetry in hadronic final states using MT2 in pp collisions at $\sqrt{s} = 7$ TeV", *JHEP* **1210** (2012) 018, doi:10.1007/JHEP10(2012)018, arXiv:1207.1798.

[78] D. Ghosh, M. Guchait, S. Raychaudhuri et al., "How Constrained is the cMSSM?", *Phys. Rev. D* **86** (2012) 055007, doi:10.1103/PhysRevD.86.055007, arXiv:1205.2283.

[79] A. Strumia, "The Fine-tuning price of the early LHC", *JHEP* **1104** (2011) 073, doi:10.1007/JHEP04(2011)073, arXiv:1101.2195.

[80] CMS Collaboration, "Summary Plots from 7 TeV CMS SUSY analyses". https://twiki.cern.ch/twiki/bin/view/CMSPublic/SUSYSMSSummaryPlots7TeV. Accessed: 2015-01-30.

[81] N. Arkani-Hamed, P. Schuster, N. Toro et al., "MARMOSET: The Path from LHC Data to the New Standard Model via On-Shell Effective Theories", arXiv:hep-ph/0703088.

[82] J. Alwall, P. Schuster, and N. Toro, "Simplified Models for a First Characterization of New Physics at the LHC", *Phys. Rev. D* **79** (2009) 075020, doi:10.1103/PhysRevD.79.075020, arXiv:0810.3921.

[83] LHC New Physics Working Group Collaboration, "Simplified Models for LHC New Physics Searches", *J. Phys. G* **39** (2012) 105005, doi:10.1088/0954-3899/39/10/105005, arXiv:1105.2838.

[84] CMS Collaboration, "Interpretation of Searches for Supersymmetry with

simplified Models", *Phys. Rev. D* **88** (2013), no. 5, 052017, doi:10.1103/PhysRevD.88.052017, arXiv:1301.2175.

[85] CMS Collaboration, "Summary Plots from 8 TeV CMS SUSY analyses". https://twiki.cern.ch/twiki/pub/CMSPublic/SUSYSMSSummaryPlots8TeV/SUSY2013T2ttT6.pdf. Accessed: 2015-01-30.

[86] G. D. Kribs, A. Martin, and A. Menon, "Natural Supersymmetry and Implications for Higgs physics", *Phys. Rev. D* **88** (2013) 035025, doi:10.1103/PhysRevD.88.035025, arXiv:1305.1313.

[87] WMAP Collaboration Collaboration, "First year Wilkinson Microwave Anisotropy Probe (WMAP) observations: Determination of cosmological parameters", *Astrophys. J. Suppl.* **148** (2003) 175, doi:10.1086/377226, arXiv:astro-ph/0302209.

[88] S. P. Martin, "Compressed supersymmetry and natural neutralino dark matter from top squark-mediated annihilation to top quarks", *Phys. Rev. D* **75** (2007) 115005, doi:10.1103/PhysRevD.75.115005, arXiv:hep-ph/0703097.

[89] S. P. Martin, "The Top squark-mediated annihilation scenario and direct detection of dark matter in compressed supersymmetry", *Phys. Rev. D* **76** (2007) 095005, doi:10.1103/PhysRevD.76.095005, arXiv:0707.2812.

[90] C. Balazs, M. S. Carena, and C. Wagner, "Dark matter, light stops and electroweak baryogenesis", *Phys. Rev. D* **70** (2004) 015007, doi:10.1103/PhysRevD.70.015007, arXiv:hep-ph/0403224.

[91] M. Drees, M. Hanussek, and J. S. Kim, "Light Stop Searches at the LHC with Monojet Events", *Phys. Rev. D* **86** (2012) 035024, doi:10.1103/PhysRevD.86.035024, arXiv:1201.5714.

[92] C. Boehm, A. Djouadi, and M. Drees, "Light scalar top quarks and supersymmetric dark matter", *Phys.Rev.* **D62** (2000) 035012, doi:10.1103/PhysRevD.62.035012, arXiv:hep-ph/9911496.

[93] K.-i. Hikasa and M. Kobayashi, "Light scalar top quark at e^+e^- colliders", *Phys. Rev. D* **36** (Aug, 1987) 724–732, doi:10.1103/PhysRevD.36.724.

[94] C. Boehm, A. Djouadi, and Y. Mambrini, "Decays of the lightest top squark", *Phys. Rev. D* **61** (Apr, 2000) 095006, doi:10.1103/PhysRevD.61.095006.

[95] ALICE Collaboration, "The ALICE experiment at the CERN LHC", *JINST* **3** (2008) S08002, doi:10.1088/1748-0221/3/08/S08002.

[96] ATLAS Collaboration, "The ATLAS Experiment at the CERN Large Hadron Collider", *JINST* **3** (2008) S08003, doi:10.1088/1748-0221/3/08/S08003.

[97] CMS Collaboration, "The CMS experiment at the CERN LHC", *JINST* **3** (2008) S08004, doi:10.1088/1748-0221/3/08/S08004.

[98] LHCb Collaboration, "The LHCb Detector at the LHC", *JINST* **3** (2008) S08005, doi:10.1088/1748-0221/3/08/S08005.

[99] CMS Collaboration, "CMS Physics: Technical Design Report Volume 1: Detectornce and Software", technical design report cms, CERN, (2006).

[100] M. Cacciari, G. P. Salam, and G. Soyez, "The anti-$\mathrm{k_t}$ jet clustering algorithm", *JHEP* **04** (2008) 063, doi:10.1088/1126-6708/2008/04/063, arXiv:0802.1189.

[101] CMS Collaboration, "Particle Flow Event Reconstruction in CMS and Performance for Jets, Taus and MET", CMS Physics Analysis Summary CMS-PAS-PFT-09-001, (2009).

[102] Aachen-Annecy-Birmingham-CERN-Helsinki-London(QMC)-Paris(CdF)-Riverside-Rome-Rutherford-Saclay(CEN)-Vienna Collaboration, "Experimental observation of isolated large transverse energy electrons with associated missing energy at $\sqrt{s} = 540$ GeV", *Phys. Lett. B* **122** (Jan, 1983) 103–116, doi:10.1016/0370-2693(83)91177-2.

[103] Vienna-Wisconsin Collaboration, Aachen-Amsterdam(NIKHEF)-Annecy-Birmingham-CERN-Harvard-Helsinki-Kiel-London(IC)-London(QMC)-MIT-Padua-Paris(CdF)-Riverside-Rome-Rutherford-Saclay(CEN)-Victoria Collaboration, "Events with large missing transverse energy at the CERN collider: I. $\mathrm{W} \to \tau\,\nu$ decay and test of $\tau - \mu - e$ universality at $\mathrm{Q}^2 = \mathrm{m}_W^2$", *Phys. Lett. B* **185** (Nov, 1986) 233–240, doi:10.1016/0370-2693(87)91561-9.

[104] Vienna-Wisconsin Collaboration, Aachen-Amsterdam(NIKHEF)-Annecy-Birmingham-CERN-Harvard-Helsinki-Kiel-London(IC)-London(QMC)-MIT-Padua-Paris(CdF)-Riverside-Rome-Rutherford-Saclay(CEN)-Victoria Collaboration, "Events with large missing transverse energy at the CERN collider: II. Search for the decays of W+- into heavy leptons and of Z0 into non-interacting

particles", *Phys. Lett. B* **185** (Nov, 1986) 241–248, doi:10.1016/0370-2693(87)91562-0.

[105] CMS Collaboration, "CMS The TriDAS Project: Technical Design Report, Volume 2: Data Acquisition and High-Level Trigger. CMS trigger and data-acquisition project", technical report, Geneva, (2002).

[106] CMS Collaboration, "Evidence for the direct decay of the 125 GeV Higgs boson to fermions", *Nature Phys.* **10** (2014) 557–560, doi:10.1038/nphys3005, arXiv:1401.6527.

[107] CMS Collaboration, "CMS Technical Design Report for the Level-1 Trigger Upgrade", Technical Report CERN-LHCC-2013-011. CMS-TDR-12, CERN, Geneva, (Jun, 2013). Additional contacts: Jeffrey Spalding, Fermilab, Jeffrey.Spalding@cern.ch Didier Contardo, Universite Claude Bernard-Lyon I, didier.claude.contardo@cern.ch.

[108] R. Frazier, S. Fayer, G. Hall et al., "A demonstration of a Time Multiplexed Trigger for the CMS experiment", *JINST* **7** (2012), no. 01, C01060.

[109] M. Baber, M. Blake, J. Brooke et al., "Development and testing of an upgrade to the CMS level-1 calorimeter trigger", *JINST* **9** (2014), no. 01, C01006.

[110] M. Cacciari and G. P. Salam, "Pileup subtraction using jet areas", *Phys. Lett. B* **659** (2008) 119, doi:10.1016/j.physletb.2007.09.077, arXiv:0707.1378.

[111] CM Collaboration, "Search for supersymmetry in hadronic final states with missing transverse energy using the variables α_T and b-quark multiplicity in pp collisions at $\sqrt{s} = 8$ TeV", *Eur. Phys. J. C* **73** (2013) 2568, doi:10.1140/epjc/s10052-013-2568-6, arXiv:1303.2985.

[112] technical report.

[113] A. Delgado and M. Strassler, "A Simple-Minded Unitarity Constraint and an Application to Unparticles", *Phys. Rev. D* **81** (2010) 056003, doi:10.1103/PhysRevD.81.056003.

[114] D0 Collaboration, "Search for large extra dimensions via single photon plus missing energy final states at $\sqrt{s} = 1.96$-TeV", *Phys. Rev. Lett.* **101** (2008) 011601, doi:10.1103/PhysRevLett.101.011601, arXiv:0803.2137.

[115] CDF Collaboration, "Search for large extra dimensions in final states containing

one photon or jet and large missing transverse energy produced in $p\bar{p}$ collisions at $\sqrt{s} = 1.96$-TeV", *Phys. Rev. Lett.* **101** (2008) 181602, doi:10.1103/PhysRevLett.101.181602, arXiv:0807.3132.

[116] CDF Collaboration, "A Search for dark matter in events with one jet and missing transverse energy in $p\bar{p}$ collisions at $\sqrt{s} = 1.96$ TeV", *Phys. Rev. Lett.* **108** (2012) 211804, doi:10.1103/PhysRevLett.108.211804, arXiv:1203.0742.

[117] ATLAS Collaboration, "Search for new phenomena with the monojet and missing transverse momentum signature using the ATLAS detector in $\sqrt{s} = 7$ TeV proton-proton collisions", *Phys. Lett. B* **705** (2011) 294, doi:10.1016/j.physletb.2011.10.006, arXiv:1106.5327.

[118] ATLAS Collaboration, "Search for dark matter candidates and large extra dimensions in events with a jet and missing transverse momentum with the ATLAS detector", *JHEP* **1304** (2013) 075, doi:10.1007/JHEP04(2013)075, arXiv:1210.4491.

[119] CMS Collaboration, "Search for New Physics with a Mono-Jet and Missing Transverse Energy in pp Collisions at $\sqrt{s} = 7$ TeV", *Phys. Rev. Lett.* **107** (2011) 201804, doi:10.1103/PhysRevLett.107.201804, arXiv:1106.4775.

[120] CMS Collaboration, "Search for dark matter and large extra dimensions in monojet events in pp collisions at $\sqrt{s} = 7$ TeV", *JHEP* **09** (2012) 094, doi:10.1007/JHEP09(2012)094, arXiv:1206.5663.

[121] CMS Collaboration, "Search for dark matter, extra dimensions, and unparticles in monojet events in proton-proton collisions at $\sqrt{s} = 8$ TeV", arXiv:1408.3583.

[122] OPAL Collaboration, "Photonic events with missing energy in e+ e- collisions at S**(1/2) = 189-GeV", *Eur. Phys. J. C* **18** (2000) 253, doi:10.1007/s100520000522, arXiv:hep-ex/0005002.

[123] A. Heister et al., "Single- and multi-photon production in ee collisions at $\sqrt{s}$s up to 209 GeV", *Eur. Phys. J. C* **28** (2003), no. 1, 1, doi:10.1140/epjc/s2002-01129-7.

[124] L3 Collaboration Collaboration, "Single photon and multiphoton events with missing energy in e^+e^- collisions at LEP", *Phys. Lett. B* **587** (2004) 16, doi:10.1016/j.physletb.2004.01.010, arXiv:hep-ex/0402002.

[125] DELPHI Collaboration, "Photon events with missing energy in e+ e- collisions at s**(1/2) = 130-GeV to 209-GeV", *Eur. Phys. J. C* **38** (2005) 395, doi:10.1140/epjc/s2004-02051-8, arXiv:hep-ex/0406019.

[126] D0 Collaboration, "Search for large extra dimensions via single photon plus missing energy final states at $\sqrt{s} = 1.96$-TeV", *Phys. Rev. Lett.* **101** (2008) 011601, doi:10.1103/PhysRevLett.101.011601, arXiv:0803.2137.

[127] CMS Collaboration, "Search for Dark Matter and Large Extra Dimensions in pp Collisions Yielding a Photon and Missing Transverse Energy", *Phys. Rev. Lett.* **108** (2012) 261803, doi:10.1103/PhysRevLett.108.261803, arXiv:1204.0821.

[128] ATLAS Collaboration, "Search for dark matter candidates and large extra dimensions in events with a photon and missing transverse momentum in pp collision data at $\sqrt{s} = 7$ TeV with the ATLAS detector", *Phys. Rev. Lett.* **110** (2013), no. 1, 011802, doi:10.1103/PhysRevLett.110.011802, arXiv:1209.4625.

[129] J. Alwall et al., "MadGraph/MadEvent v4: the new web generation", *JHEP* **09** (2007) 028, doi:10.1088/1126-6708/2007/09/028, arXiv:0706.2334.

[130] J. Alwall, R. Frederix, S. Frixione et al., "The automated computation of tree-level and next-to-leading order differential cross sections, and their matching to parton shower simulations", *JHEP* **07** (2014) 079, doi:10.1007/JHEP07(2014)079, arXiv:1405.0301.

[131] T. Sjöstrand, S. Mrenna, and P. Z. Skands, "PYTHIA 6.4 physics and manual", *JHEP* **05** (2006) 026, doi:10.1088/1126-6708/2006/05/026, arXiv:hep-ph/0603175.

[132] T. Sjöstrand, S. Mrenna, and P. Z. Skands, "A Brief Introduction to PYTHIA 8.1", *Comput. Phys. Commun.* **178** (2008) 852, doi:10.1016/j.cpc.2008.01.036, arXiv:0710.3820.

[133] R. Field, "Early LHC Underlying Event Data - Findings and Surprises", arXiv:1010.3558.

[134] S. Agostinelli, J. Allison, and K. A. et al, "Geant4a simulation toolkit", *Nucl. Instrum. Meth. A* **506** (2003), no. 3, 250, doi:doi.org/10.1016/S0168-9002(03)01368-8.

[135] J. Allison et al., "Geant4 developments and applications", *IEEE 53* **1** (2006) 270, doi:10.1109/TNS.2006.869826.

[136] CMS Collaboration, "The fast simulation of the CMS detector at LHC", *J. Phys. Conf. Ser.* **331** (2011) 032049, doi:10.1088/1742-6596/331/3/032049.

[137] J. Pumplin, D. R. Stump, J. Huston et al., "New Generation of Parton Distributions with Uncertainties from Global QCD Analysis", *JHEP* **07** (2002) 012, doi:10.1088/1126-6708/2002/07/012, arXiv:hep-ph/0201195.

[138] S. Alioli, P. Nason, C. Oleari et al., "NLO single-top production matched with shower in POWHEG: s- and t-channel contributions", *JHEP* **0909** (2009) 111, doi:10.1007/JHEP02(2010)011,10.1088/1126-6708/2009/09/111, arXiv:0907.4076.

[139] E. Re, "Single-top Wt-channel production matched with parton showers using the POWHEG method", *Eur.Phys.J.* **C71** (2011) 1547, doi:10.1140/epjc/s10052-011-1547-z, arXiv:1009.2450.

[140] N. Davidson, G. Nanava, T. Przedzinski et al., "Universal Interface of TAUOLA Technical and Physics Documentation", *Comput. Phys. Commun.* **183** (2012) 821, doi:10.1016/j.cpc.2011.12.009, arXiv:1002.0543.

[141] S. Höche, F. Krauss, N. Lavesson et al., "Matching parton showers and matrix elements", (2006). arXiv:hep-ph/0602031. Appear in proceedings of 'HERA and the LHC: A Workshop on the Implications of HERA for LHC Physics: CERN - DESY Workshop 2004/2005'.

[142] CMS Collaboration, "Performance of CMS muon reconstruction in pp collision events at $\sqrt{s} = 7$ TeV", *J. Inst* **7** (October, 2012) 2P, doi:10.1088/1748-0221/7/10/P10002, arXiv:1206.4071.

[143] CMS Collaboration, "Performance of electron reconstruction and selection with the CMS detector in proton-proton collisions at $\sqrt{s} = 8$TeV", (2015). arXiv:1502.02701. Submitted to *JINST*.

[144] CMS Collaboration, "Search for neutral Higgs bosons decaying to τ pairs in pp collisions at $\sqrt{s} = 7$ TeV", *Phys. Lett. B* **713** (2012) 68, doi:10.1016/j.physletb.2012.05.028, arXiv:1202.4083.

[145] CMS Collaboration, "Performance of τ-lepton reconstruction and identification in

CMS", *JINST* **7** (2012) 1001, doi:10.1088/1748-0221/7/01/P01001, arXiv:1109.6034.

[146] CMS Collaboration, "CMS tracking performance results from early LHC operation", *Eur. Phys. J. C* **70** (2010) 1165, doi:10.1140/epjc/s10052-010-1491-3, arXiv:1007.1988.

[147] CMS Collaboration, "Transverse momentum and pseudorapidity distributions of charged hadrons in pp collisions at $\sqrt{s} = 0.9$ and 2.36 TeV", *JHEP* **02** (2010) 041, doi:10.1007/JHEP02(2010)041.

[148] CMS Collaboration, "Interpretation of Searches for Supersymmetry with simplified Models", arXiv:1301.2175.

[149] M. Krämer, A. Kulesza, R. van der Leeuw et al., "Supersymmetry production cross sections in pp collisions at $\sqrt{s} = 7$ TeV", arXiv:1206.2892.

[150] CMS Collaboration, "CMS Luminosity Based on Pixel Cluster Counting - Summer 2013 Update", CMS Physics Analysis Summary CMS-PAS-LUM-13-001, CERN, (2013).

[151] L. Moneta, K. Cranmer, G. Schott et al., "The RooStats Project", in *Proceedings of the 13th International Workshop on Advanced Computing and Analysis Techniques in Physics Research (ACAT2010)*. SISSA, 2010. arXiv:1009.1003.

List of Figures

List of Tables

1 Acronyms

ADD Arkani-Hamed, Dimopoulos, and Dvali

ALICE A Large Ion Collider Experiment

ATLAS A Toroidal LHC ApparatuS

APD Avalanche Photo-Diode

ASIC Application Specific Integrated Circuit

BAU Baryon Asymmetry of the Universe

BSM Beyond the Standard Model

CERN European Organisation for Nuclear Research

CKM Cabibbo-Kobayashi-Maskawa

C.L. Confidence Level

CMS Compact Muon Solenoid

CMSSM Compressed Minimal Supersymmetric Standard Model

CP Charge Parity

CSCs Cathode Stripe Chambers

CSV Combined Secondary Vertex

CSVM Combined Secondary Vertex Medium Working Point

CPU Computer Processing Unit

DAQ Data Acquisition System

DIS Deep Inelastic Scattering

DESY Deutsches Elektronen-Synchrotron

DM Dark Matter

DT Drift Tube

ECAL Electromagnetic Calorimeter

EB	Electromagnetic Calorimeter Barrel
EE	Electromagnetic Calorimeter Endcap
ES	Electromagnetic Calorimeter pre-Shower
EMG	Exponentially Modified Gaussian
EPJC	European Physical Journal C
EWK	Electroweak
FCNC	Flavour Changing Neutral Currents
FPGA	Field Programmable Gate Array
FSR	Final State Radiation
GCT	Global Calorimeter Trigger
GMT	Global Muon Trigger
GT	Global Trigger
GUT	Grand Unified Theory
HB	Hadron Barrel
HCAL	Hadronic Calorimeter
HE	Hadron Endcaps
HF	Hadron Forward
HLT	Higher Level Trigger
HO	Hadron Outer
HPD	Hybrid Photodetectors
HPS	Hadron–Plus–Strips
ISR	Initial State Radiation
JES	Jet Energy Scale
LUT	Look Up Table
L1	Level 1 Trigger

LEP	Large Electron-Positron Collider
LHC	Large Hadron Collider
LHCb	Large Hadron Collider Beauty
LO	Leading Order
LSP	Lightest Supersymmetric Particle
MC	Monte Carlo
MSSM	Minimal Supersymmetric Standard Model
NLL	Next to Leading Logorithmic Order
NLO	Next to Leading Order
NLSP	Next-to-Lightest Supersymmetric Particle
NNLO	Next to Next Leading Order
PF	Particle Flow
POGs	Physics Object Groups
PS	Proton Synchrotron
PU	pile-up
QED	Quantum Electro-Dynamics
QCD	Quantum Chromo-Dynamics
QFT	Quantum Field Theory
PDFs	Parton Density Functions
RBXs	Readout Boxes
RPCs	Resistive Plate Chambers
RCT	Regional Calorimeter Trigger
RMT	Regional Muon Trigger
SLAC	Stanford Linear Accelerator Center
SUSY	SUperSYmmetry

SM	Standard Model
SMS	Simplified Model Spectra
SPS	Super Proton Synchrotron
TIB	Tracker Inner Barrel
TEC	Tracker Endcaps
TID	Tracker Inner Disks
TMT	Time-Multiplexed Trigger
TOB	Tracker Outer Barrel
TF	Transfer Factor
TP	Trigger Primitive
VeV	Vacuum Expectation Value
VPT	Vacuum Photo-Triode
WIMP	Weakly Interacting Massive Particle
WMAP	Wilkinson Microwave Anisotrophy Probe